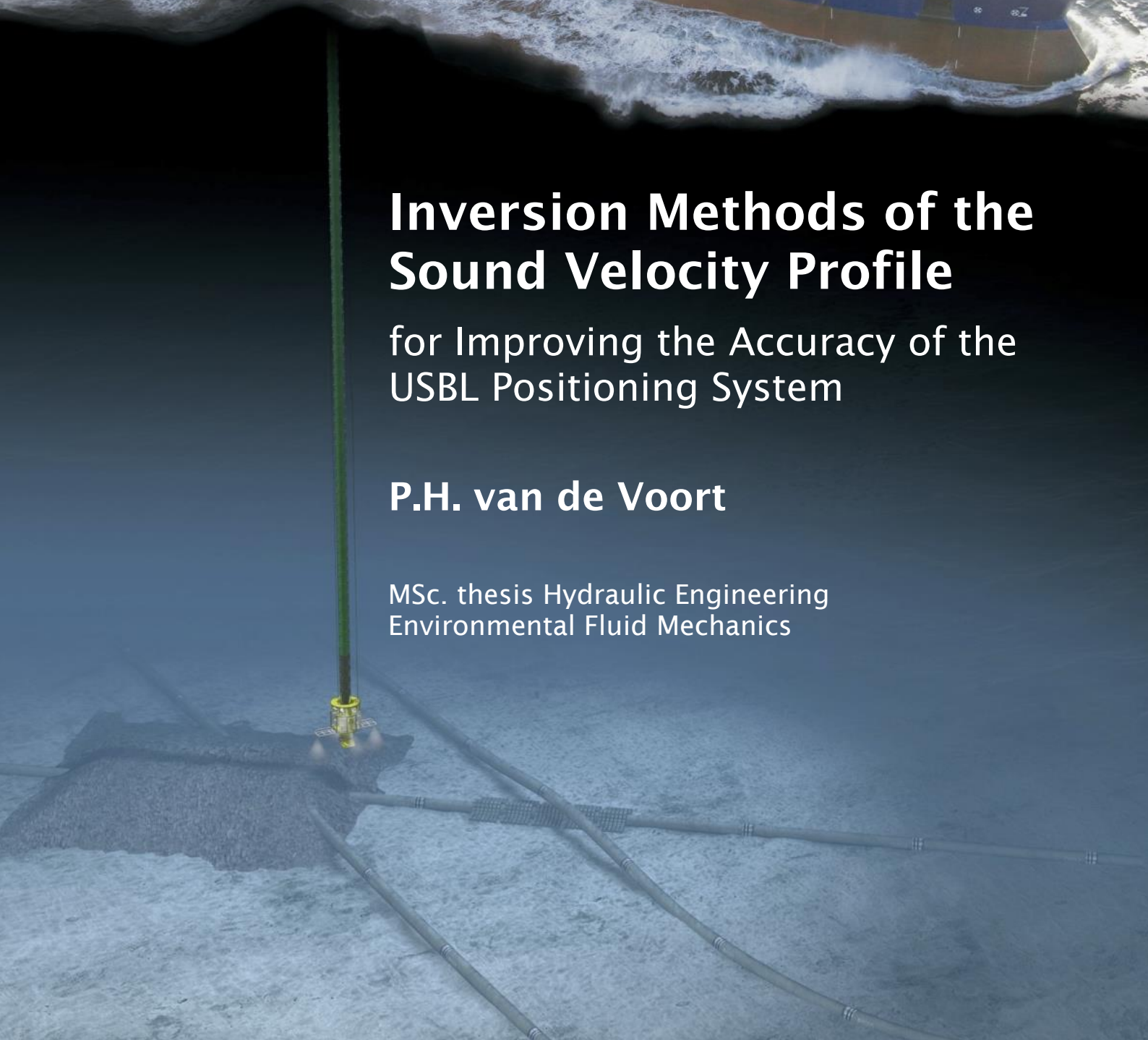# Inversion Methods of the Sound Velocity Profile

for Improving the Accuracy of the USBL Positioning System

P.H. van de Voort

MSc. thesis Hydraulic Engineering
Environmental Fluid Mechanics

Inversion Methods of the Sound Velocity Profile

for Improving the Accuracy of the USBL Positioning System

by

P.H. (Nick) van de Voort

In partial fulfilment of the requirements for the degree of

Master of Science
in Civil Engineering

at the Delft University of Technology
to be publicly defended on Monday June 13, 2022 at 3:00 PM.

ABSTRACT

Remotely Operated Vehicles (ROVs) are positioned relative to an underwater acoustic positioning system: Ultra-Short BaseLine (USBL). The accuracy is affected by refraction artifacts, caused by the variations of the sound velocity in the water column. Accurate positioning would require continuous measuring of the sound velocity profile (SVP) which is unpractical and preferably to be minimized. It requires alternative or inversion methods to obtain SVP information. In this thesis, two inversion methods are introduced: HISOM (Hull In Situ Ocean Model) and OMBES (Overlapping MultiBeam EchoSounder).

HISOM analysis whether the SVP can be approximated via other sources: 1) a constant profile based on the in situ surface (ISS) sound velocity, or 2) a profile derived from ocean model data in combination with the ISS sound velocity. These simplifications inevitably introduce a refraction error but for fallpipe ROVs operating at small incident angles (e.g. $\theta < 6°$) this error may be within acceptable margins (e.g. threshold of $0.2\,m$). The applicability is assessed by estimating the horizontal refraction error with a ray-tracing technique using daily-mean SVPs, derived from freely-available ocean model data. A spatiotemporal quantification for the North Sea yielded maps of sea areas where SVP measurements are necessary, and areas where constant surface SVPs suffice. The latter are the shallow parts of the North Sea ($< 80\,m$), where the error is always smaller than $0.2\,m$. For deeper locations, the gradients of the SVP cannot be neglected. Then, the model-based SVPs can be used with or without the use of ISS sound velocity data. Comparing a collection of observed SVPs in the North Sea revealed that these daily-mean model-based SVPs are accurate enough for the positioning of fallpipe ROVs at least up to $370\,m$ depth.

OMBES uses the synchronous overlap in depth measurements between two dual-head multibeam echosounders (MBES). In previous studies, the overlap is obtained by sailing two adjacent tracks with one MBES on a ship. Here, we propose to use two MBESs deployed on the same ship, thereby reducing the uncertainty of the ship's motions that affect the quality of the depth measurements. The mean sound velocity can be inverted by mathematically minimizing the depth differences in the overlap. This technique completely minimizes the refraction error with frequent updates of the inverted mean sound velocity on the flight. Subsequently, the mean sound velocity can be used to locate ROVs that operate close to the seafloor in shallow water ($< 80\,m$), even for large incident angles (e.g. $\theta \sim 65°$). Simulations showed that the best performance of the inversion technique is established when maximizing the distance between the multibeam heads, and by inward-tilting one or two heads. Practically, it means the deployment of MBESs on either side of the ship, rather than one pair of MBESs at mid-ship.

With increasing access to reliable ocean data, HISOM methods can potentially be run on ocean forecast model data to assess where and when refraction artifacts become dominant for fallpipe ROV positioning. This automatic assessment tool supports the SVP measuring strategy in subsea rock installation projects. OMBES can potentially be used as monitoring tool by comparing near real-time updates of the inverted mean sound velocity with the measured SVP. This data-driven decision tool can assist when to take an additional SVP. OMBES also improves the accuracy of multibeam bathymetric surveys by automatic collection of SVPs.

PREFACE

The Master thesis forms the final product in completing the Master Hydraulic Engineering at Delft University of Technology. During this thesis, I have learned that I am particularily passionate about the powerful role metocean data can play in industry-specific solutions. The collection of more and better ocean data will ultimately contribute to better decision making, improved business outcomes, and a greater understanding of our environment. A year ago, Gerben the Boer brought me into contact with Eric Peeters, Operations Manager Survey at Van Oord. Eric shared the difficulties he faced due to the sound velocity bias in underwater acoustic positioning of their fallpipe ROV. In this light, I decided to conduct my graduation research in collaboration with Van Oord to explore alternative methods for obtaining sound veloicty profile information.

I would like to thank Eric Peeters for providing me insight in the practicalities of subsea rock installation works, in particular for taking me to Van Oord's flexible fallpipe vessel Stornes, where I could discuss the topic with the crew and actually see the ingenuity of a fallpipe ROV. Gerben de Boer, I would like to thank you for your support as daily supervisor and the countless tips you gave me that helped me significantly in the organization and writing of the thesis. Your creative ideas and new perspectives provided guidance and boosted my motivation. You have sparked my enthusiasm about the future of data-driven decisionmaking tools for offshore engineering projects. I am looking forward working together with you on these interesting projects. As part of the survey team, I would like to thank Jan van den Berg for the enormous support to provide me with all information I needed. Your valuable knowledge helped me bringing theory to practice. You connected me with many colleagues that were willing to share their experiences and thoughts. In particular, thanks to Paul Hunt, Jeroen van de Grift and John van der Marel.

I also want to thank my committee members from the TU Delft during my research. Julie Pietrzak, I want to thank you for guiding this research and your knowledge on stratified flows. Mirjam Snellen, your critical and well-thought questions helped me to improve my work, in particular your attention to detail on the mathematics. Lennart Keyzer, I want to thank you for your valuable feedback and dicussions on the working mechanisms of the inverison methods. In addition, Tannaz Haji Mohammadloo, I want to thank you for your view on the adjusted method I proposed for the sound velocity inversion technique you and Mirjam worked on.

Finally, my gratitude goes out to my family and friends. Your support and friendship allowed me in discussing the topic but also in getting my mind off the thesis enjoying my time as student.

Rotterdam, June 2022

Nick van de Voort

CONTENTS

SUMMARY

Remotely Operated Vehicles (ROVs) are commonly used in underwater applications such as geophysical field surveys and offshore industry applications. ROVs are positioned relative to an underwater acoustic positioning system: Ultra-Short BaseLine (USBL). It is based on the installation of a transceiver on a pole under the vessel and a transponder mounted on the ROV. The two-way message exchange of the acoustic signal sent between the transceiver and transponder is used to estimate the range between the vessel and the vehicle, based on the time-tracking and the underwater sound velocity profile (SVP). Together with the angle of arrival, the ROV can be positioned.

The accuracy of underwater acoustic positioning depends on the accuracy of the sound velocity profile (SVP). The sound velocity varies in time and space as the salinity, temperature and pressure (depth) vary in time and space. According to Snell's law of refraction, sound velocity variations bend the ray path. Therefore, incorrect or insufficient knowledge about the SVP introduces so-called refraction errors. Consequently, the ROV will be positioned at the wrong location. Accurate positioning would require continuous measuring of the SVP which is unpractical and preferably to be minimized. Hence, the sampling rate of SVPs is a trade-off between the certainty of the positioning accuracy and economic costs. Van Oord is interested in minimizing the need for these laborious SVP measurements while keeping the accuracy of USBL positioning at desired levels. It requires alternative or inversions methods to obtain SVP information. In this thesis, two inversion methods are introduced: HISOM (Hull In Situ Ocean Model) and OMBES (Overlapping MultiBeam EchoSounder).

HISOM analysis whether the SVP can be approximated via other sources: 1) a constant profile based on the in situ surface (ISS) sound velocity, or 2) a profile derived from ocean model data in combination with the ISS sound velocity. HISOM methods primarily try to get away with a constant surface SVP or a model-based SVP that yield a refraction error that is still acceptable in terms of positioning accuracy. HISOM applies to ROVs operating at small incident angles (e.g. $\theta < 6°$, fallpipe ROVs), for which the use of constant and model-based SVPs is less penalized. The applicability is assessed by estimating the horizontal refraction error with a ray-tracing technique using daily-mean SVPs, derived from freely-available ocean model data. The spatiotemporal quantification of the horizontal refraction error for the North Sea yielded maps of sea areas where – depending on the seasonal stratification of the sound velocity – SVP measurements are necessary, and areas where constant surface SVPs suffice. The latter are the shallow parts of the North Sea ($< 80\ m$), where the error is always smaller than $0.2\ m$. For locations where the variations in the SVP cannot be neglected, the model-based SVPs can be used with or without the use of ISS sound velocity data. Comparing a collection of observed SVPs in the North Sea revealed that these daily-mean model-based SVPs are accurate enough for the positioning of fallpipe ROVs at least up to $370m$ depth (e.g. 90% of the North Sea).

OMBES uses the synchronous overlap in depth measurements between two dual-head multibeam echosounders. In previous studies, the overlap is obtained by sailing two adjacent tracks with one MBES on a ship. Here, we propose to use two MBESs deployed on the same ship, thereby reducing the uncertainty of the ship's motions that affect the quality of the depth measurements. The mean sound velocity can be inverted by mathematically minimizing the depth differences in the overlap. This technique completely minimizes the refraction error with near real-time updates of the inverted mean sound velocity on the flight. Subsequently, the mean sound velocity can be used to locate ROVs that operate close to the seafloor in shallow water ($< 80\ m$), even for large incident angles (e.g. $\theta \sim 65°$). Simulations showed that the best performance of the inversion technique is established when maximizing the distance between the multibeam heads (i.e. on port and starboard side of the surface vessel), and by inward-tilting one or two heads (e.g. 20°).

With increasing access to reliable ocean data, HISOM methods can potentially be run on ocean forecast model data to assess where and when refraction artifacts become dominant for fallpipe ROV positioning. This automatic assessment tool can support the SVP measuring strategy in subsea rock installation projects. OMBES can potentially be used as monitoring tool by comparing near real-time updates of the inverted mean sound velocity with the measured SVP. This data-driven decision tool can assist when to take an additional SVP, for instance when positioning ROVs for cable-laying activity. OMBES can also potentially improve the accuracy of multibeam bathymetric surveys by automatic collection of SVPs.

EXECUTIVE SUMMARY

Remotely Operated Vehicles (ROVs) are commonly used in underwater applications such as geophysical field surveys (e.g. seabed mapping) and offshore industry applications (e.g. subsea infrastructure inspection and subsea rock installation). ROVs are self-propelled submersibles tethered with a surface vessel for communication and power purposes. ROVs are positioned relative to an underwater acoustic positioning system. Ultra-Short BaseLine (USBL) is one of those acoustic positioning systems. It is based on the installation of a transceiver on a pole under the vessel and a transponder mounted on the ROV. The transceiver emits an acoustic signal and the transponder receives the signal, and replies with its own acoustic signal. This two-way message exchange is used to estimate the range between the vessel and the vehicle, based on the time-tracking and the underwater sound velocity profile (SVP). Together with the angle of arrival, the ROV can be positioned.

The accuracy of underwater acoustic positioning is affected by refraction artifacts, caused by the vertical variations of the sound velocity along the water depth. The sound velocity varies in time and space as the salinity, temperature and pressure (depth) vary in time and space. This causes changes in the acoustic properties of the seawater. According to Snell's law of refraction, sound velocity variations bend the ray path, causing a change of direction. When measured incorrectly, not frequently enough or in the wrong location, you get what are so-called refraction errors. Consequently, the ROV will be positioned at the wrong location. This phenomenon is illustrated in Figure S.1.

Since the USBL utilizes the transmission and reception of acoustic pulses, knowledge of the exact ray path would require continuous measuring of the SVP. This is unpractical: the vessel has to stop in the middle of its offshore operation and stay in a drift when lowering the sound velocity sensor. Hence, it is a trade-off between the certainty of the positioning accuracy and economic costs. The research question is therefore:

Figure S.1 Ray bending as result of variations in the SVP. The grey-dashed SVP spatiotemporally changes to the black-solid SVP. This causes the ray path to change, therewith introducing refraction errors ($\Delta x, \Delta z$) if one does not use the true SVP.

How to minimize the need for underwater sound velocity profile measurements, while improving the accuracy of ultra-short baseline positioning in a dynamically changing marine environment?

The sparse sampling of SVPs means that alternative or inversion methods are needed to obtain information about the vertical variation of the sound velocity. To this end, the thesis introduces <u>two methods for the inversion of the SVP</u>:

1. **HISOM** (Hull In Situ Ocean Model) methods use the instantaneous sound velocity measurement under the hull of the vessel. Two variants of HISOM are introduced:
    i. **CSSV method** (Constant Surface Sound Velocity)
       It neglects the vertical variation of the SVP. Instead, a constant (zero-gradient) SVP is constructed with its value based on the in situ surface (ISS) sound velocity.
    ii. **MSVP method** (Model-based Sound Velocity Profile)
       It estimates the SVP from freely-available ocean model data in combination with the ISS sound velocity.
2. **OMBES** (Overlapping MultiBeam EchoSounder) method uses the depth differences between soundings in the overlap of dual-head multibeam swaths to invert the mean sound velocity.
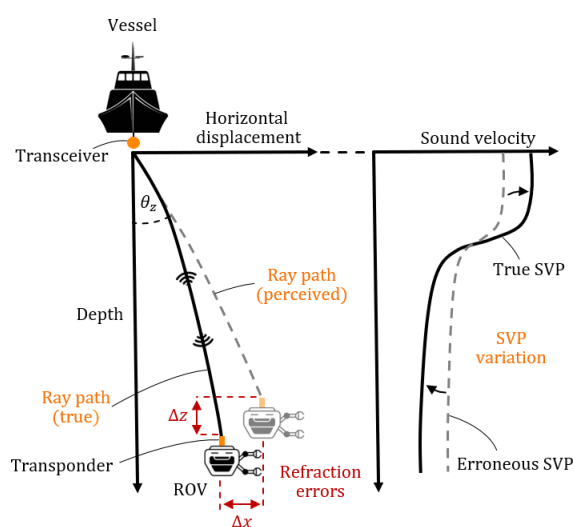
HISOM

HISOM analyses whether the contractor needs to take an SVP measurement or can rely on the ISS sound velocity measured under the hull of the vessel with a sound velocity sensor. HISOM methods primarily try to get away with a constant or model-based SVP that yield a refraction error that is still acceptable in terms of positioning accuracy. Both variants of HISOM apply to ROVs that are operating at small incident angles (almost directly under the vessel's transceiver), for which the use of constant and model-based SVPs is less penalized. Figure S.2 shows a schematization of the methods. In particular, attention is paid to the application of fallpipe ROVs (FPROVs), used for subsea rock installation projects. FPROVs have limited flexibility because of the attached fallpipe, and are therefore located close to the transceiver's nadir.
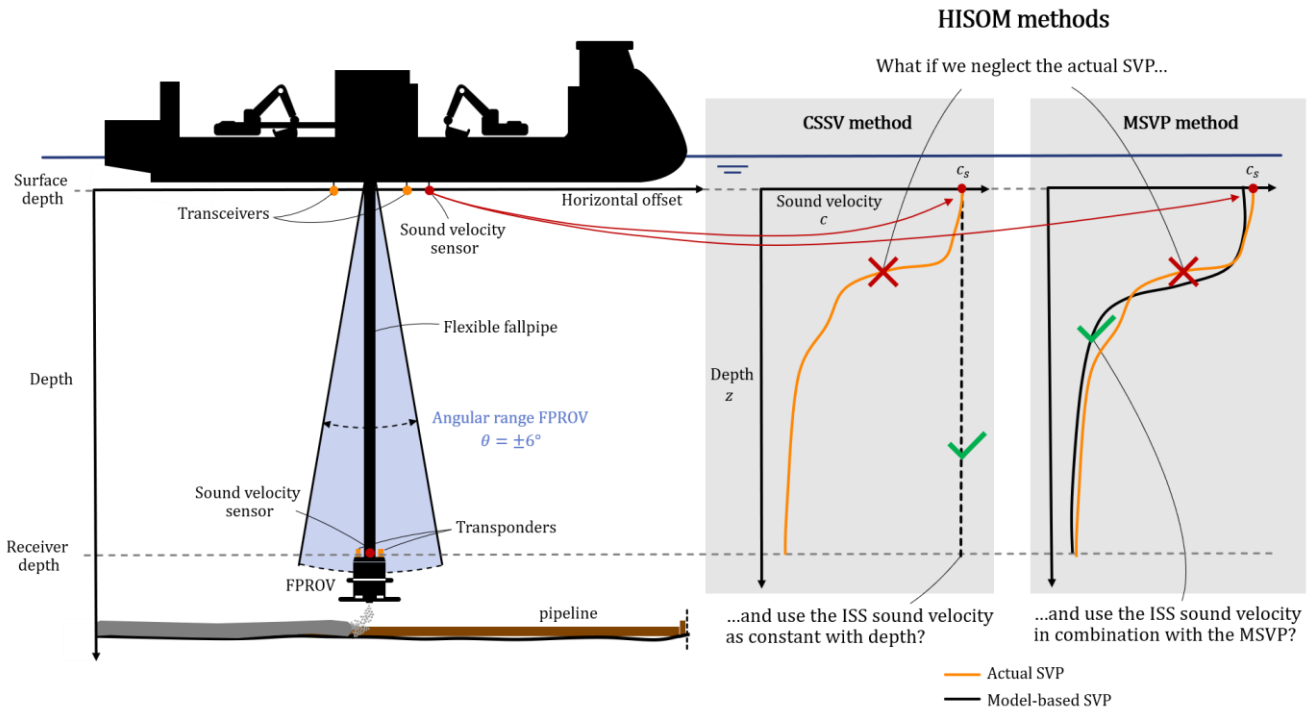
Figure S.2 Left: schematization of Van Oord's subsea rock installation vessel Bravenes and the FPROV. Right: schematization of two variants of HISOM method. The CSSV method uses the ISS sound velocity and considers it to be constant with depth. The MSVP method uses the ISS sound velocity in combination with the model-based SVP.

To answer where and when an SVP measurement can be neglected, HISOM makes use of free-of-charge-and-state-of-the-art ocean data from GLORYS 12V1. The most recent 10-year record (2010-2020) of daily-mean three-dimensional temperature and salinity matrices are requested, and translated into model-based SVPs. The model-based SVPs are compared to SVP observations collected by Van Oord on subsea rock installation trips in the North Sea. One example is shown in Figure S.3a where the surface sound velocity is plotted together with the average sound velocity over depth. The latter is essentially the harmonic mean sound velocity [1].

When the difference is small between the surface sound velocity and the harmonic mean sound velocity, the SVP usually shows less vertical variation. In terms of accuracy of underwater acoustic positioning, it means that refraction errors are negligible. In such case, it suffices to use the CSSV method i.e. construct a constant SVP with its value based on the ISS sound velocity.

---

[1] The harmonic mean sound velocity differs from a depth-weighted mean sound velocity as it is calculated by dividing the total depth by the sum of times it takes for the sound pulse to pass through each layer of constant sound speed.
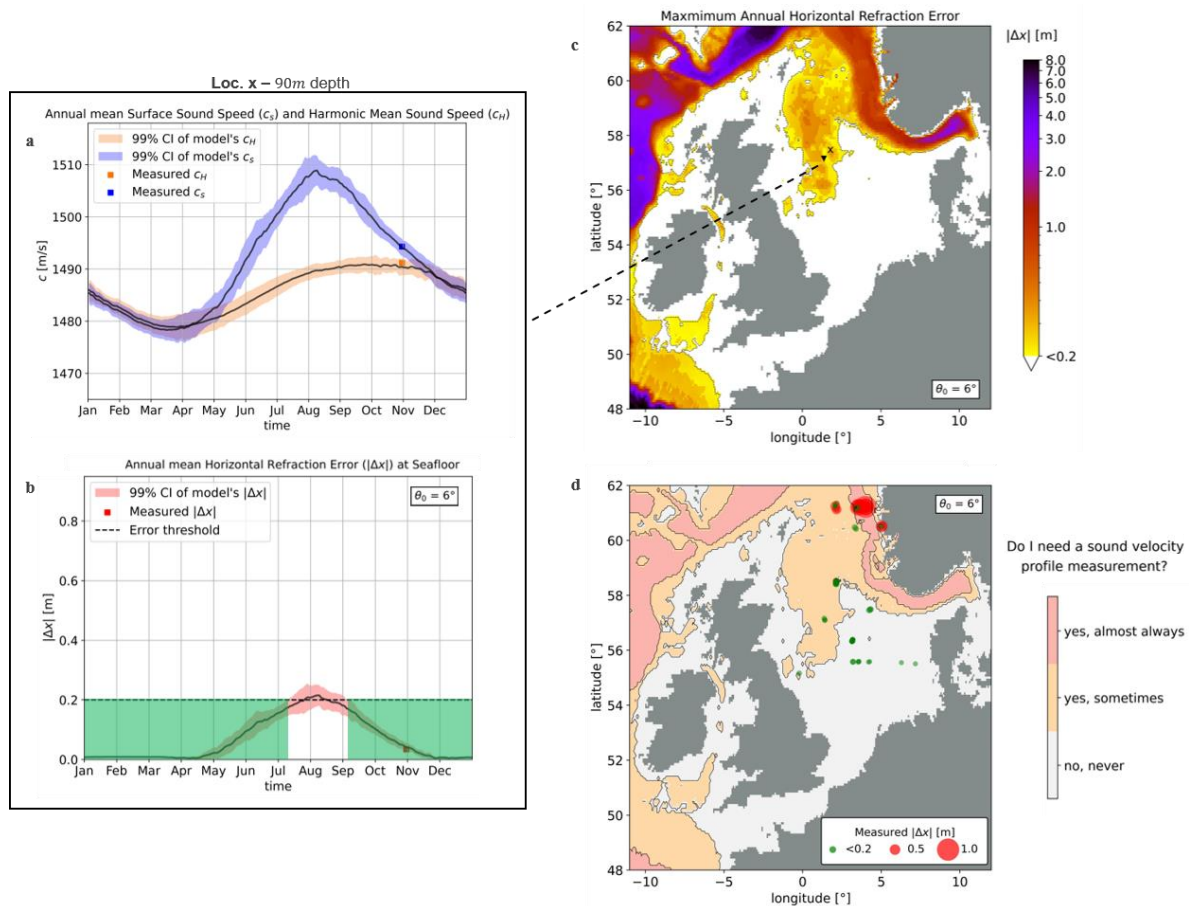
Figure S.3 a) Modelled timeseries of annual mean (black solid line) surface sound speed c_s and harmonic mean sound speed c_H. **b)** Modelled timeseries of annual mean horizontal refraction-induced positioning error $|\Delta x|$ at the seafloor for an incident angle $\theta_s = 6°$ (i.e. maximum angular range of FPROVs) when using the CSSV method. Green areas highlight the time window when the upper bound of the confidence interval (CI) for the horizontal refraction error is below the threshold of $0.2\ m$. Location x : 57.16°N; 1.37°E. **c)** Maximum annual horizontal refraction-induced positioning error at the seafloor for an incident angle $\theta_s = 6°$ when using the CSSV method. **d)** Sea areas where SVP measurements are necessary i.e. where the complexity of the SVP cannot be neglected. Areas are defined as time of the year that the horizontal refraction error is greater than the threshold of $0.2\ m$: *almost always* $> 85\%$, *sometimes* $\leq$ 85%, *never* 0%. Dots are the calculated horizontal refraction errors based on 72 observed SVPs.

Whether the difference is small enough depends on the horizontal refraction-induced positioning error [2]. The refraction error is a measure of the consequence of considering the ISS sound velocity as constant and may be (un)acceptable in offshore industry application (e.g. threshold of $0.2\ m$). Its value depends on the incident angle of the acoustic signal, and the spatiotemporal stratification of the SVP in combination with the depth propagation of the induced error. Figure S.3b shows timeseries of the horizontal refraction-induced positioning error. The green squares are the time windows when the horizontal refraction error is less than the user-defined threshold. In those periods, one does not need information of the vertical variation of the sound velocity. Instead, the ISS sound velocity can be used for USBL positioning of FPROVs. Since this surface value is measured continuously at the hull, there is no need to stop the vessel in the middle of an offshore operation.

The application of the CSSV method can be scaled up by performing the analysis for each ocean model grid cell in a sea area of interest e.g. the North Sea. The North Sea is characterized by strong seasonal stratification and freshwater run-off from rivers and the Baltic Sea. Consequently, the surface sound velocity shows seasonal deviations from the harmonic mean sound velocity. When neglecting the SVP and use the ISS sound velocity

---

[2] The vertical refraction-induced errors originating from the use of erroneous SVPs by the USBL positioning system are inferior because the ROV's depth estimate is primarily based on the difference in hydrostatic pressure, measured by pressure sensors mounted on the surface vessel and the ROV.

instead, horizontal refraction errors are introduced. However, these errors can only grow when the depth is sufficient. Therefore, much of the variability observed in the refraction errors (Figure S.3c) can be explained by the bathymetry of the North Sea. From Figure S.3c we infer that the shallow part (e.g. approximately less than $80m$) of the North Sea never experiences refraction errors larger than $0.2\ m$ when operating under small angles (e.g. FPROVs). For those subsea rock installation projects, no SVP measurement is necessary at time of operation if using the ISS sound velocity (Figure S.3d). It means that no additional stops are required to update the USBL system, therewith saving costly operation time. For locations where the complexity of the SVP cannot be neglected (e.g. red dots in Figure S.3d), one could apply the MSVP method for USBL positioning. Comparing with observed SVPs, these daily-mean model-based SVPs are found to be accurate enough for the positioning of FPROV at least up to $370m$ depth.

With increasing access to reliable ocean nowcast and forecast model predictions, HISOM methods have potential application for monitoring and planning purposes by means of an automatic assessment tool. The result would be an interactive ocean map with the horizontal refraction error the offshore contractor can expect in the upcoming days when positioning the FPROV with USBL (quite similar to Figure S.3c).

OMBES

A multibeam echosounder (MBES) is used in bathymetric surveys to obtain accurate underwater topography. It is a type of sonar that emits acoustic pulses in a fan-shape beneath the transceiver, perpendicular to the sailing direction. It uses the SVP and the time it takes for the sound pulses to reflect off the seafloor and return to the receiver to calculate the water depth. Directional information is extracted from the returning sound pulses using beamforming. The result is a swath of depth readings from a single ping. The accuracy of MBES bathymetric measurements depends on the accuracy of sound velocity information. An incorrect SVP induces refraction errors, which tend to worsen with offset from the sonar's nadir.

OMBES uses the overlap in depth measurements between two MBESs to invert the harmonic mean sound velocity. Whereas previous studies particularly focused on correcting MBES bathymetric measurements to obtain accurate underwater topography and yield the inverted harmonic mean sound velocity as by-product, this thesis proposes to use the inverted harmonic mean for USBL positioning. And instead of obtaining the semi-synchronized overlap in MBES swaths by sailing adjacent track lines (e.g. single-head MBES configuration), we propose to obtain the synchronous overlap in one single sailing track using a dual-head MBES configuration. This set-up is schematized in Figure S.4.
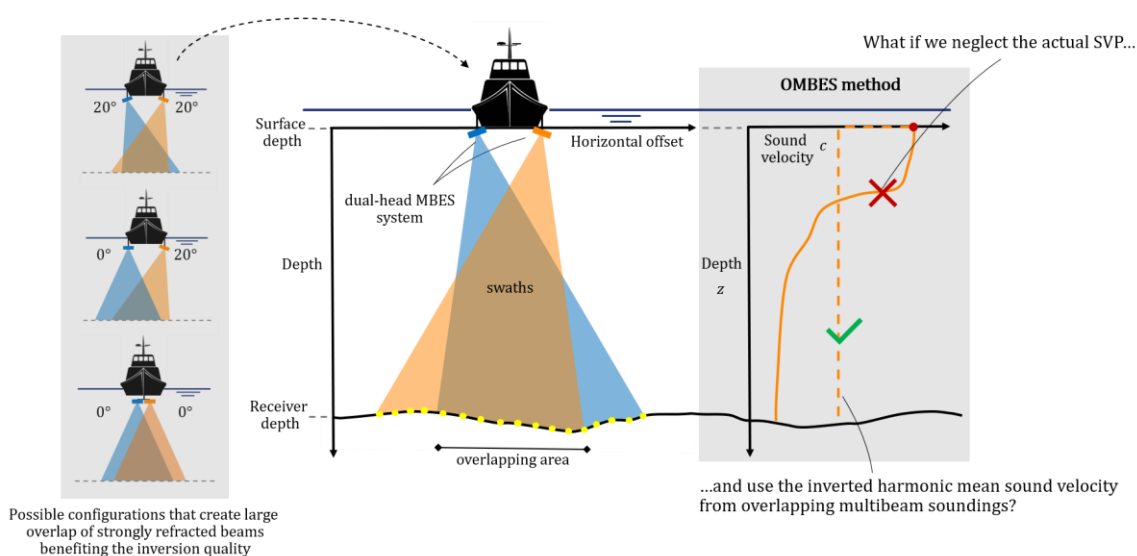

Figure S.4 Schematization of a dual-head multibeam echosounder system mounted on a survey vessel. OMBES uses the depth differences between soundings in the overlap of two swaths to invert the harmonic mean sound velocity the inverted harmonic mean sound velocity The yellow dots indicate the soundings at the seafloor.

Since the multibeam transducer heads are subject to approximately the same pitch and yaw, the two swaths of a dual-head MBES are aligned. This set-up allows to invert the harmonic mean sound velocity near real-time along the track by computing an energy function with soundings combined from one ping per head. The energy function quantifies the mismatch in depth estimates between overlapping swaths caused by the use of an erroneous SVP. Subsequently, minimization of the energy function with COBYLA – a constrained nonlinear derivative-free optimization solver – returns the harmonic mean sound velocity. The inverted harmonic mean sound velocity can be used for acoustic positioning of ROVs that are operating close to the seafloor. Moreover, close to the transceiver's nadir the error is small because refraction is limited for small incident angles. For this application range, simulations show promising results with horizontal refraction errors smaller than $0.2\ m$, even for large incident angles ($\theta_s \sim 65°$ e.g. approximately 2 water depths horizontally away from the surface vessel). The best performance of the inversion was found when maximizing the distance between the multibeam heads - mounted on the port and starboard side of the vessel (e.g. $25\ m$ difference) – and by inward-tilting one or two heads (e.g. $20°$). For this set-up, the minimum swath width is about $50°$ in $40\ m$ water depth.

In principle, no additional SVP measurements are needed when using OMBES, provided that the ROV stays close to the transceiver's nadir or close to the seafloor. However, when the client still demands SVP measurements to ensure the quality of the offshore project, OMBES can be used as monitoring tool. By comparing real-time updates of the inverted harmonic mean sound velocity with the harmonic mean of the measured SVP (at the start of the operation), the contractor can make a data-driven decision when to take an additional SVP.

To summarize, this thesis introduces two inversions methods that provide acceptable substitute SVPs for improving the accuracy of USBL positioning. HISOM methods try to get away with a refraction error that still acceptable by providing insight into the oceanographic dynamics that govern the SVP measurement strategy and planning e.g. where and when can the contractor neglect the actual SVP and rely on simplified or model-based estimates. The method can be run on ocean forecast models, making it a potential automatic assessment tool for FPROV positioning in shallow to deep water ($\pm 1000\ m$). OMBES completely minimizes the refraction error with frequent updates of the inverted harmonic mean sound velocity on the flight. There is no need to take additional SVP measurements, as long as the ROV stays close to the transceiver's nadir or close to the seafloor. OMBES suites better to ROVs that operate in shallow water ($< 80\ m$) because multibeam data rapidly loses its accuracy and hit count with increasing depth. OMBES can also be used for shallow water survey operations that cannot stop to do SVP measurements (for example in a busy waterway) or for multibeam bathymetric surveys that aim to optimize the quality of the bathymetric data by collecting SVP inversions.

NOMENCLATURE

c	Sound velocity
Δc	Measurement error of the sound velocity sensor
c_H	Harmonic mean sound velocity
Δc_H	Harmonic mean sound velocity estimation error
$\hat{c}_H$	Optimized harmonic mean sound velocity (vector)
c_i	Sound velocity per depth layer i
c_r	Sound velocity at receiver depth
c_s	Surface sound velocity, at the transducer head of the USBL or MBES
$c_{s,n}$	Surface sound velocity at the multibeam transducer head from the nth swath
$\hat{c}_s$	Surface sound velocity (vector), at the multibeam transducer head
$\text{d}c$	Sound velocity increment
d	Distance between transducer elements (baselines)
Δd	Spacing error between the transducer elements
d	Euclidian distance between depth measurements k and cell centre m_0
E	Energy
f	Frequency of the acoustic signal
g	Sound velocity gradient
g_i	Sound velocity gradient per depth layer i
$\boldsymbol{g}$	Constant sound velocity gradient
$\boldsymbol{g}_n$	Constant sound velocity gradient from the nth swath
$\hat{\boldsymbol{g}}$	Constant sound velocity gradient (vector)
$\hat{\boldsymbol{g}}_{low}$	Lower bound of the constrained constant sound velocity gradient (vector)
$\hat{\boldsymbol{g}}_{up}$	Upper bound of the constrained constant sound velocity gradient (vector)
h	Relative depth
Δh	Depth measurement error
h_H	Relative depth of the USBL transducer head
h_{ROV}	Relative depth of the ROV
k	Depth measurement
$K_{m,n}$	Total number of depth measurements from the nth swath in the mth cell
K_n	Total number of depth measurements from the nth swath
M	Total number of grid cells covering the overlap in a subregion
m_0	Cell centre of grid
n	Number of sound velocity measurements with depth or swath number
N	Total number of swaths
p	Snell's constant
$p_{m,n,k}$	Snell's constant of the kth depth measurement from the nth swath in the mth cell
$p_{n,k}$	Snell's constant of the kth depth measurement from the nth swath
r	Slant range
R	Radius of curvature
R_i	Radius of curvature per depth layer i
S	Sea water salinity
$\text{d}S$	Arc length increment
S_a	Integral of the actual sound velocity profile
S_e	Integral of the equivalent sound velocity profile
S_H	Integral of the harmonic sound velocity profile

TUDelft

Van Oord
Marine ingenuity

t	Half of the two-way travel time of signal (from transmission until reception), total propagation time
Δt	Time delay measurement error
t_i	Time instant per depth layer i
t_r	Time instant of depth layer r, remaining time
$t_{m,n,k}$	Half of the two-way travel time of signal of the kth depth measurement from the nth swath in the mth cell
$t_{n,k}$	Half of the two-way travel time of signal of the kth depth measurement from the nth swath
T	Sea water potential temperature
T	Period of the acoustic signal
x	Horizontal distance between transducer and across-track direction of ROV or seafloor
Δx_i	Horizontal displacement of acoustic pulse per depth layer i
Δx_r	Horizontal displacement of acoustic pulse at receiver depth r (seafloor or ROV transponder)
$\overline{\Delta x}$	Root-mean-square horizontal positioning error of multiple contributing error terms
$\|\Delta x\|$	Absolute (refraction-induced) horizontal positioning error
X	x-axis of the grid and data partition for soundings
y	Horizontal distance between transducer and along-track direction of ROV or seafloor
Y	y-axis of the grid and data partition for soundings
z	Vertical distance between transducer and surface normal direction of ROV or seafloor
$\mathrm{d}z$	Depth increment
Δz_i	Vertical displacement of acoustic pulse per depth layer i
Δz_r	Vertical displacement of acoustic pulse at receiver depth r (seafloor or ROV transponder)
$\|\Delta z\|$	Refraction-induced vertical positioning error
$\bar{z}$	The mean depth from depth estimates of the aligned swaths
$\bar{z}_m$	The mean depth from depth estimates in the mth cell
$z_{m,n,k}$	The kth depth measurement from the nth swath in the mth cell
z_r	True receiver depth level r, relative depth level of seafloor or ROV transponder
z_r'	Approximated receiver depth level r, relative depth level of seafloor or ROV transponder
z_s	Surface depth level, relative depth level of transducer head of the USBL or MBES
$\hat{z}_s$	Surface depth level (vector), relative depth level of multibeam transducer head
$z_{s_{m.n}}$	Depth of the multibeam transducer head at surface level from the nth swath in the mth cell
z_{s_n}	Depth of the multibeam transducer head at surface level from the nth swath
$\delta_{\|\Delta x\|}$	Threshold for the maximum allowable horizontal refraction error
ϵ_z	Vertical positioning error due to the approximation of the ESVP ray-tracing algorithm of Lu *et al.* (2012)
θ	Incident angle (angle between incident ray and surface normal)
$\Delta \theta$	Angle measurement error
$\mathrm{d}\theta$	Angle increment
θ_x	Incident angle with respect to x
θ_y	Incident angle with respect to y
θ_z	Incident angle with respect to z
θ_i	Incident angle per depth layer i
θ_r	Incident angle at receiver depth r beam angle for flat seabed, remaining angle
θ_s, θ_0	Incident angle at surface level, at the transducer head of the USBL or MBES
$\theta_{s_{m,n,k}}$	Incident angle at surface level at the multibeam transducer head of the kth depth measurement from the nth swath in the mth cell

TUDelft

Van Oord
Marine ingenuity

$\theta_{s_{n,k}}$	Incident angle at surface level at the multibeam transducer head of the kth depth measurement from the nth swath
λ	Wavelength of the acoustic signal
σ	Standard deviation from the mean
τ	Time-difference, relative delay between two transducer elements of the acoustic wave passing
φ_x	Phase-difference between two transducer elements of the acoustic wave passing with respect to x
φ_y	Phase-difference between two transducer elements of the acoustic wave passing with respect to y
φ_z	Phase-difference between two transducer elements of the acoustic wave passing with respect to z
$\Delta\varphi$	Phase-difference error

TUDelft

Van Oord
Marine ingenuity

ACRONYMS

AMUST	A Priori Multibeam Uncertainty Simulation Tool
API	Application Programming Interface
CAS	Central Authentication Service
CI	Confidence Interval
CMEMS	Copernicus Marine Environment Monitoring Service
COBYLA	COnstrained BY Linear Approximation
CSSV	Constant Surface Sound Velocity
CTD	Conductivity/Temperature/Depth sensor
DVL	Doppler Velocity Log
EC	European Commission
ESVP	Equivalent Sound Velocity Profile
FPROV	FallPipe Remotely Operated Vehicle
GNSS	Global Navigation Satellite System
HiPAP	High-Precision Acoustic Positioning
HISOM	Hull In Situ Ocean Model
IDE	Integrated Development Environment
IMCA	International Marine Contractors Association
INS	Inertial Navigation System
ISS	In Situ Surface
MBES	MultiBeam EchoSounder
MOTU	API from Copernicus Marine Service
MRU	Motion Reference Unit
MSVP	Model-based Sound Velocity Profile
MVP	Moving Vessel Profiler
NOAA	National Oceanic and Atmospheric Administration
NetCDF	Network Common Data Form
OMBES	Overlapping MultiBeam EchoSounder
PS	Pressure Sensor
QPS	Quality Positioning Services company
ROFI	Region Of Freshwater Influence
ROV	Remotely Operated Vehicle
SD	Standard Deviation
SMARTMAP	Sea Mappers' Acoustic Ray-Tracing Monitor And Planning
SNR	Signal-to-Noise Ratio
SRI	Subsea Rock Installation
SVP	Sound Velocity Profile
TP	TransPonder
TPU	Total Propagated Uncertainty
TVU	Total Vertical Uncertainty
UAPS	Underwater Acoustic Positioning System
USBL	Ultra-Short BaseLine
WD	Water Depth

1. INTRODUCTION

This chapter provides an introduction to remotely operated vehicles and the challenges faced by the offshore industry for underwater acoustic positioning, in particular due to spatiotemporal variation of the underwater sound velocity. Next, the research aim and research questions are formulated, followed by the thesis outline.

1.1 Background Information

1.1.1 Remotely Operated Vehicles (ROVs)

Remotely Operated Vehicles (ROVs) are commonly used in underwater applications such as geophysical field surveys (e.g. seabed mapping) and offshore industry applications (e.g. subsea infrastructure inspection and subsea rock installation). ROVs are self-propelled submersibles whose operation is under minimal supervisory control (Christ and Wernli, 2013). They are hard-wired (tethered) with a surface vessel for communication and/or power purposes. The ROV is part of the underwater survey system and

Figure 1.1 Pipeline inspection with an ROV (Seatools, 2022).

assists the contractor to meet the quality specifications set by the client. They have evolved into very powerful, well-instrumented work systems able to accommodate in the "dull, dirty and dangerous" work environment of the world's waters (Christ and Wernli, 2013).

Marine contractor Van Oord makes use of work-class ROVs that support cable-laying activity and pipeline inspection (Figure 1.1). For subsea rock installation (SRI) projects, the ROV is attached to a flexible fallpipe (Figure 1.2) – the so-called fallpipe ROVs (FPROVs) – allowing to install rock with high accuracy in water depths from 15 up to 1500 meters.
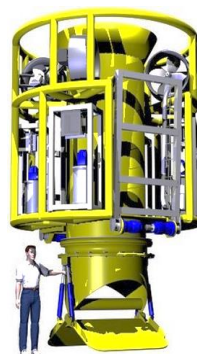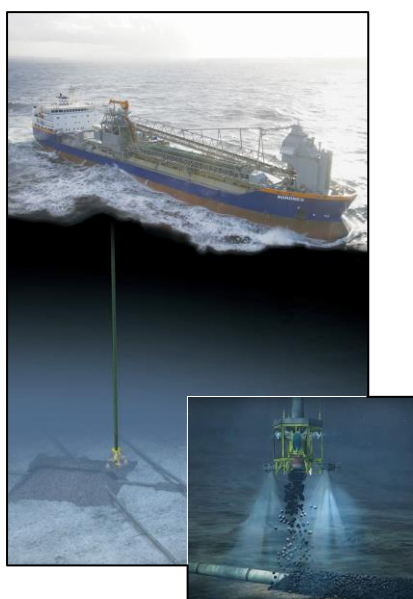

Figure 1.2 Subsea rock installation vessel Nordnes equipped with an FPROV (Van Oord, 2021).

1.1.2 Underwater acoustic positioning with USBL

Ultra-Short BaseLine

ROVs are positioned relative to an Underwater Acoustic Positioning System (UAPS). Ultra-Short BaseLine (USBL) is one of those UAPSs (Sun *et al.*, 2019), and is also known as the "range and bearing system". Figure 1.3 shows a typical USBL positioning system.

It is based on the installation of a transceiver on a pole under the vessel and a transponder mounted on the ROV. The transceiver emits an acoustic signal (pulse) and the transponder receives the signal, and replies with its own acoustic pulse (i.e. the transponder mode). This two-way message exchange is used to estimate the distance between the vessel and the vehicle, based on the time tracking and the SVP. Alternatively, the transponder is triggered via the umbilical cable, allowing for higher update rates as the acoustic pulse only travels one-way (i.e. the responder mode). In principle, one transponder suffices for acoustic communication purposes, but often multiple are installed to assure navigability in case one shuts down. For the FPROVs, six or more transponders are mounted to circumvent blockage and reflection with the fallpipe itself. Angles are measured by the transceiver,

Figure 1.3 Typical USBL positioning system.

which contains an array of transducer elements. The transceiver head ($\pm 40\ cm$) contains at least three (but often more) transducer elements. They are separated by fixed distances referred to as short baselines, from where the system gets its name. The time-phase differences between each transducer element are used to calculate the direction of the transponder (Li *et al.*, 2018). An interesting reader is referred to appendix C.1 for the derivation of the USBL principle equations for the range and bearing calculation. Figure 1.4 shows the components of the USBL positioning system, where the transceiver is interfaced to vessel heading, attitude and surface positioning systems.

Figure 1.4 Components of a typical USBL positioning system (Kongsberg Maritime, 2016; IMCA, 2017): operator station with a navigation computer, the control unit, the transceiver unit, the pole unit mounted under the vessel's hull. The spherical transceiver head (in red) consists of piezoelectric elements that can both transmit and receive acoustic signals.

Navigation aiding sensors

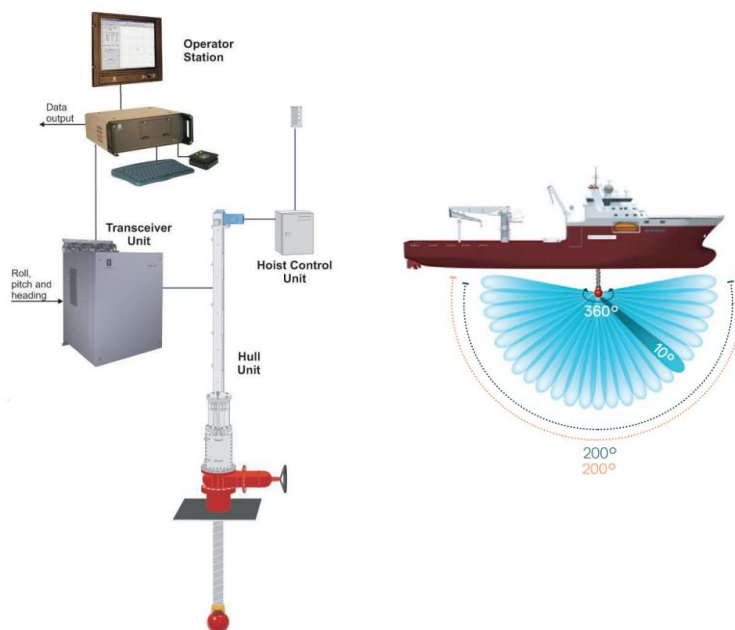ROVs are generally composed with several oceanographic sensors. The navigation system is based on INS (Inertial Navigation System) which uses a computer, accelerometers (motion sensors) and gyroscopes (rotation sensors) to continuously determine the position, velocity and orientation (e.g. pitch, roll and yaw) of the ROV by using the determined position at the previous epoch. This process is called *dead reckoning*. Often the INS is supplemented by navigation aiding sensors such as Doppler Velocity Log (DVL), Pressure Sensor (PS), Conductivity/Temperature/Depth sensor (CTD), and sound velocity probe. This is because a pure inertial solution will drift off over time (Naankeu Wati, Geldof and Seube, 2016) i.e. as each estimate of position is relative to the previous one, errors accumulate rapidly. This sensor framework is used to estimate the ROV trajectory, relative to the surface vessel, by using a Kalman Filter technique.

The translation to absolute coordinates is established with assistance of the surface survey system, among which the Global Navigation Satellite System (GNSS), and the INS of the vessel. With GNSS the vessel position can be calculated, and the INS is used to track the vessel's motions. Alternative to the INS is the Motion Reference Unit (MRU) in combination with a gyrocompass to determine the roll, pitch, heave, sway, accelerations, velocities, and geographical direction (heading).

1.1.3 Total Propagated Uncertainty (TPU)

Even with the sensor framework described above, the true position of the ROV cannot be determined due to uncertainties associated with each sensor measurement. It is impossible to find the exact position and its error. However, it is possible to estimate the uncertainty from sensor measurements with help of propagation equations. The combination of all contributing sensor uncertainties configure a predictive error budget (Naankeu Wati, Geldof and Seube, 2016). This error budget is the so-called Total Propagated Uncertainty (TPU). A good estimate of the error budget is of interest in order to meet the very demanding technical and contractual requirements in modern offshore operations. In addition, the uncertainty analysis helps to identify and correct errors during data processing.
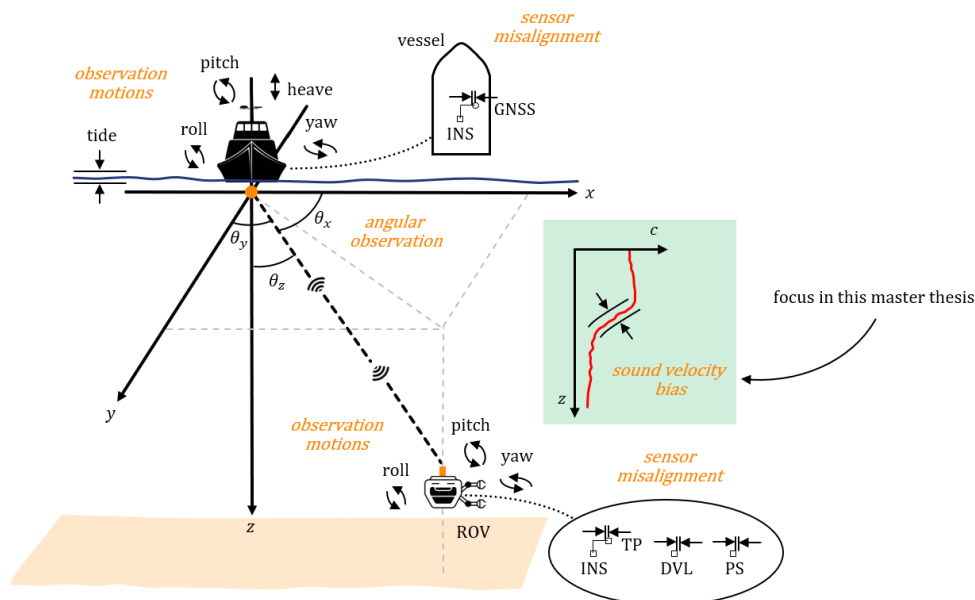
Figure 1.5 Example of an error model for an underwater survey system. Schematized are several error sources, among which the uncertainties from sensor measurements for motions and angles (e.g. random errors); the uncertainty in the sensor (mis)alignments (e.g. systematic errors). An example is the uncertainty in the distance between the center of the INS and location of the transponder (TP) mounted on the ROV's framework. In addition, the uncertainty associated with the varying underwater sound velocity is highlighted, which is the focus in this master thesis. Redrawn from Naankeu Wati, Geldof and Seube (2016).

In order to estimate the error budget, one should quantify a sequence of systematic and random errors. An overview of possible error sources is sketched in Figure 1.5. In general, the errors increase with increasing depth and increasing incident angle between the ROV's transponder and vessel's transceiver. Though, depending on the sensor and the error type, certain uncertainty propagation laws govern the magnitude of the error.

This thesis focusses on the sound velocity bias (highlighted in Figure 1.5 with green color) which is – according to Sun *et al.* (2019) – one of the main factors that restricts the accuracy of underwater acoustic positioning [3]. Compared to uncertainties from motion and attitude sensors, the uncertainty associated with the underwater sound velocity is difficult to quantify in the error budget as it depends on the marine environment. Without knowledge of the spatiotemporal variation of the SVP, the bias cannot be quantified during the operation.

1.2 Problem Description

Sound velocity bias

The sound velocity bias introduces refraction artifacts caused by the vertical variations of the sound velocity in the water column. The sound velocity varies in time and space as the salinity, temperature and pressure (depth) vary in time and space. This causes changes in the acoustic properties of the seawater (Li *et al.*, 2018). According to ray theory in acoustics (Urick, 1983), an acoustic pulse will propagate along a curved trajectory caused by gradients in the SVP (Snell's law of refraction). The acoustic ray bends, implying that the propagation distance between the transceiver and transponder is larger than the linear distance. When measured incorrectly, not frequently enough or in the wrong location, you get what are so-called refraction errors. Consequently, the ROV will be positioned at the wrong location. This phenomenon is illustrated in Figure 1.6. Thus, the spatiotemporal changes of physical properties of the seawater pose a positioning challenge which is widely known in the hydrographic survey community.
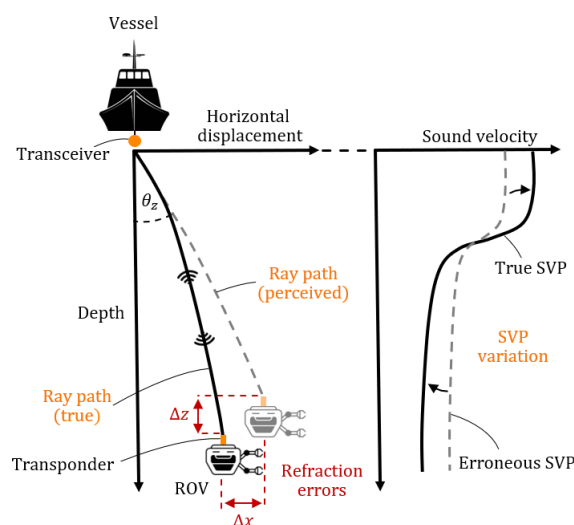

Figure 1.6 Ray bending as result of variations in the SVP. The grey-dashed SVP changes to the black-solid SVP. This causes the ray path to change, therewith introducing refraction errors ($\Delta x, \Delta z$) if one does not use the true SVP.

Laborious SVP measurements

Since the USBL utilizes the transmission and reception of acoustic pulses, knowledge of the exact path each sound pulse takes on its round trip journey to the ROV's transponder and back is crucial. However, this would require continuous measuring of the SVP, which is unpractical with its current laborious procedure: the vessel has to stop in the middle of its offshore operation and stay in a drift when lowering the sound velocity sensor. There is an option to use a Moving Vessel Profiler (MVP), which does not require the vessel to stop. However, releasing and recovering of the MVP requires high-cost equipment (Zwolak *et al.*, 2021).

Alternately, the SVP is measured with the sound velocity sensor mounted on the ROV when launching the ROV to depth (which can take up to several hours, especially in deep water). The ROV measures the instantaneous

---

[3] Another major contribution to the uncertainty associated with USBL positioning comes from the angle measurement error in determining the bearing ($\theta_x, \theta_y, \theta_z$). Its accuracy strongly depends on the water depth and the quality of the received acoustic signal. Appendix C.2 provides an in-depth error analysis for USBL positioning and quantifies the horizontal error the angular uncertainty introduces when locating the ROV.

sound velocity at its depth location and communicates this data to the vessel via the umbilical. During the rest of the operation no updates of the SVP are given, unless the operation is stopped for a manual sound velocity cast.

In practice, the USBL positioning system is initialized with the SVP measurement from the ROV's launch at the start of the operation. If the surveyor onboard suspects significant changes in the SVP, the vessel is stopped and an additional SVP cast is taken manually. This new profile is used to update the USBL positioning system, therewith reducing the risk of facing refraction errors. Hence, it is a trade-off between the certainty of the positioning accuracy and economic costs. Often the question is raised: *"How 'little' sampling can we get away while maintaining the accuracy of USBL positioning at desired level?"*

Course of action

In order to know where and when the offshore contractor can get away measuring the SVP, the sound velocity bias should be quantified in terms of the refraction-induced positioning error and be included in the error budget model. Currently, the refraction-induced positioning error is not accounted for in the error budget model of Van Oord. Consequently, the TPU is consistently underestimated.

In order to quantify the uncertainty of the sound velocity bias, two important steps must be taken:

1. *Provide suitable methods for the inversion of the SVP*
   Knowing that the physical properties of the seawater are changing during the time on site, repeated measurements of the SVP are necessary. However, SVP casts at regular intervals are laborious and costly. Therefore, we seek for solutions that minimize (or prevent) the need for SVP measurements. These solution methods use a combination of instantaneous sensor data, model data and oceanographic pre-knowledge, to invert the SVP i.e. to provide a substitute or equivalent SVP. Subsequently, the USBL positioning system is updated with the inverted SVP.
2. *Quantify the bias of the SVP*
   With an underwater acoustic ranging algorithm, one can estimate the refraction-induced positioning errors any arbitrary change in the SVP would introduce. The uncertainty quantification of the SVP potentially leads to an increase in the capability, performance and accuracy of modern USBL positioning systems. Fundamental is ray-tracing, which is a method for calculating the trajectory of the acoustic pulse through the seawater with varying velocity characteristics. Examples of fast and accurate ray-tracing algorithms are proposed in literature (Lu *et al.*, 2012; Li *et al.*, 2018).

1.3 Aim of Study

The thesis aims to provide suitable methods for the inversion of the SVP for improvement of the accuracy of the USBL positioning system in a dynamically changing marine environment, ultimately to know where and when the offshore contractor can minimize – or even prevent altogether – the need for laborious SVP measurements. The next step is to extent Van Oord's error budget model for the USBL positioning system, and in particular the inclusion of the refraction-induced positioning error that any arbitrary change in the SVP would introduce.

As client expectations, technical and contractual requirements in modern offshore operations, are moving forward (IMCA, 2017), increased capability, performance and accuracy of USBL positioning systems is necessary. Clever usage of oceanographic pre-knowledge combined with estimated SVPs and the variations therein may contribute to the fulfillment of these expectations, thereby strengthening Van Oord's leading position in the offshore market.

1.4 Research Questions

This study defines several questions to achieve the predefined objective:

Main question

How to minimize the need for underwater sound velocity profile measurements, while improving the accuracy of ultra-short baseline positioning in a dynamically changing marine environment?

Sub-questions

1. What are suitable methods to invert the underwater sound velocity profile and the spatiotemporal variability therein, and how can the estimate be used for ultra-short baseline positioning?
2. What is the contribution of the refraction-induced positioning error in the error budget model of underwater acoustic positioning systems?

1.5 Thesis Outline

This thesis presents two inversion methods:

1. **HISOM method** (chapter 3)
   HISOM (Hull In Situ Ocean Model) uses the instantaneous sound velocity measurement under the hull of the vessel. Two variants of HISOM are introduced:

   i. **CSSV method** (Constant Surface Sound Velocity)
      It neglects the vertical variation of the SVP. Instead, a constant (zero-gradient) SVP is constructed with its value based on the in situ surface (ISS) sound velocity measured under the hull.

   ii. **MSVP method** (Model-based Sound Velocity Profile)
      It estimates the SVP from freely-available ocean model data in combination with the ISS sound velocity.

HISOM methods primarily try to get away with a constant or model-based SVPs with a sound velocity bias that is still acceptable in terms of positioning accuracy. Both variants of HISOM apply to ROVs that are operating at small incident angles (almost directly under the vessel's transceiver), for which the use of simplified and model-based substitute SVPs is less penalized. In particular, attention is paid to the application of FPROV acoustic positioning with USBL in deep water. FPROVs have limited flexibility because of the attached fallpipe, and are therefore located close to the transceiver's nadir. Figure 1.7 shows a schematization of this application.
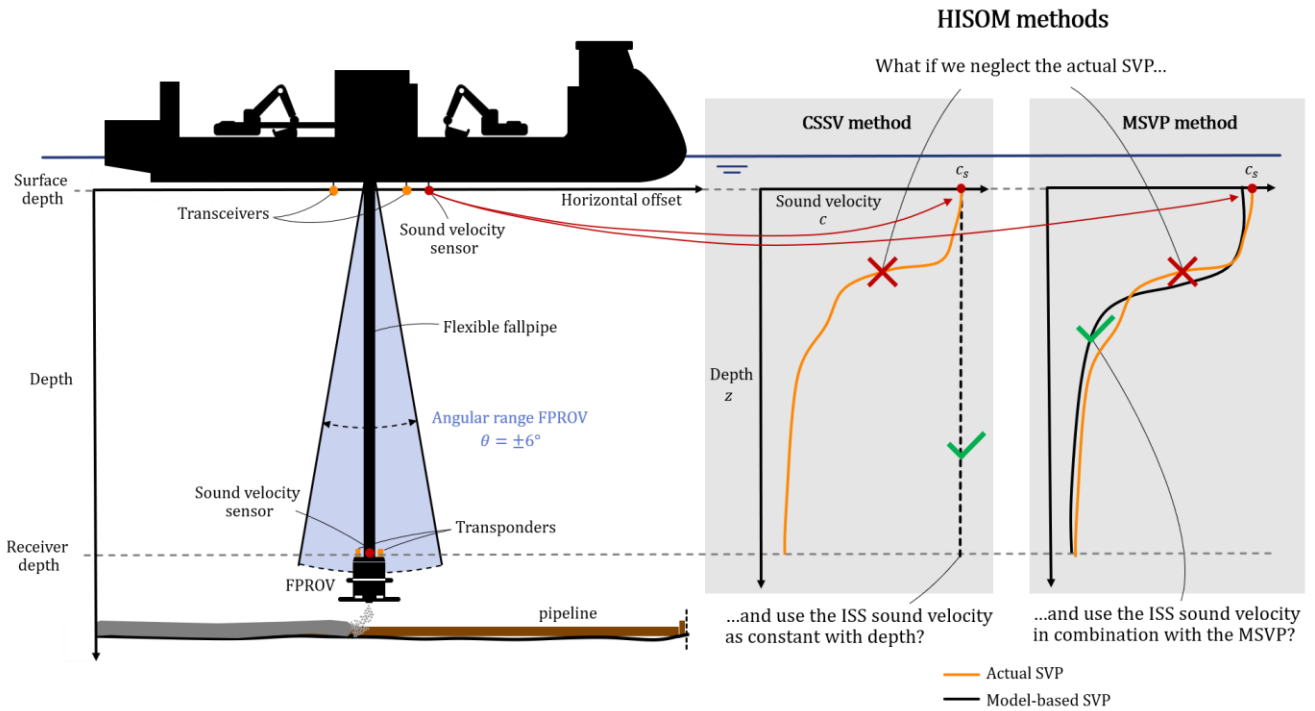
Figure 1.7 Left: schematization of Van Oord's SRI vessel Bravenes and the FPROV. Right: schematization of two variants of HISOM method. The CSSV method uses the ISS sound velocity and considers it to be constant with depth. The MSVP method uses the ISS sound velocity in combination with the model-based SVP.

2. **OMBES method** (chapter 4)

OMBES uses the depth differences between soundings in the overlap of dual-head multibeam swaths to invert the harmonic mean sound velocity. This mean value is valid for positioning of ROVs operating at small incident angles (almost directly under the vessel's transceiver), and close to the seafloor (even for large incident angles i.e. great offsets from the vessel). Whereas HISOM tries to get away with a sound velocity bias that still acceptable, OMBES completely minimizes the sound velocity bias with frequent inversions of the mean sound velocity on the flight. Figure 1.8 shows a schematization of a possible set-up for obtaining the overlap.
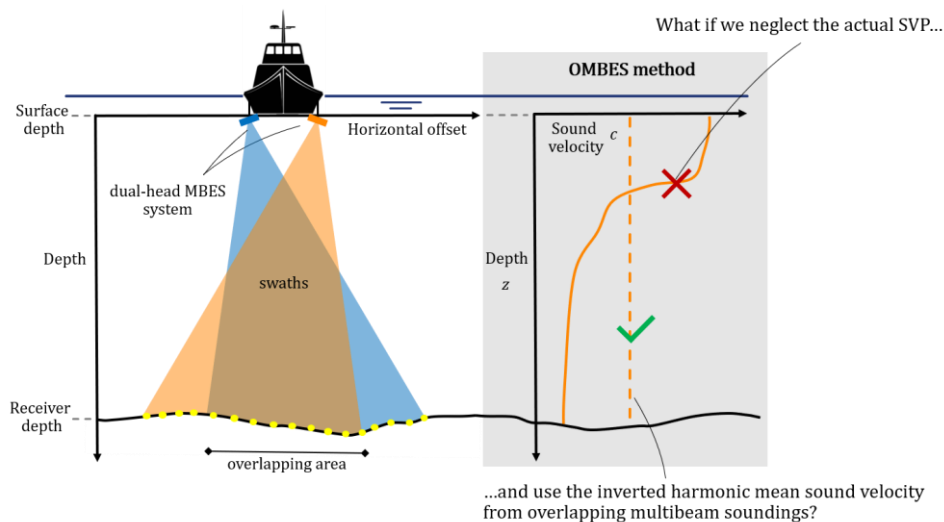

Figure 1.8 Schematization of a dual-head multibeam echosounder system mounted on a survey vessel. OMBES uses the depth differences between soundings in the overlap of two swaths to invert the harmonic mean sound velocity the inverted harmonic mean sound velocity The yellow dots indicate the soundings at the seafloor.

Furthermore, the thesis is structured as follows:

Chapter 1 is about the ROV, the underwater acoustic positioning method USBL, and the restriction in positioning accuracy caused by variations in the SVP. **Chapter 2** introduces the USBL principle, the concept of the harmonic mean sound velocity, and describes the derivation of the acoustic ray-tracing algorithm used for calculating the refraction-induced positioning errors that appraise the performance and potential applicability of the two inversion methods. **Chapter 3** introduces HISOM methods. Using both model-based SVPs from freely-available ocean model data, together with SVP observations, it is assessed where and when in the North Sea the offshore contractor can neglect the actual SVP and instead consider the ISS sound velocity as being constant with depth. The chapter ends with an error analysis of the model's ability to estimate SVPs, accurate enough for the application of FPROV acoustic positioning. **Chapter 4** introduces the OMBES method that uses the depth differences in the overlap of dual-head multibeam swaths to invert the harmonic mean sound velocity. The chapter presents the minimization algorithm used for the inversion. A proof-of-concept is presented to show the method's potential application and several model experiments are conducted to investigate the optimal configuration of the dual-head MBESs. **Chapter 5** presents the discussion, and **chapter 6** the summary, conclusion and recommendations.

2. ESVP RAY-TRACING ALGORITHM

In this chapter, we introduce the USBL principle and motivate the need for a ray-tracing algorithm that enables us to estimate the ray's position in a layered media with varying sound velocity characteristics. Subsequently, we provide the derivation of the Equivalent Sound Velocity Profile (ESVP) ray-tracing algorithm. The ESVP is a simplified substitute for the actual, complex SVP, as will become clear in paragraph 2.3. This algorithm forms the basis for calculating the refraction-induced positioning errors and appraise the performance and potential applicability of the sound velocity inversion methods presented in this thesis.

2.1 USBL Principle

The ROV's position is computed based on USBL positioning equations. These equations use the relationship between the acoustic transmitter, transducer elements, and the transponder installed on the ROV. A simplified schematic of the USBL structure is shown in Figure 2.1, where transducer elements $1, 2, 3,$ and 4 are arranged on the x, y-axis, respectively. The transmitter is located in the origin. From Figure 2.1 follow the basic equations of the USBL positioning algorithm based on the <u>slant range</u> and <u>azimuth</u> (Wang *et al.*, 2018; Tong *et al.*, 2019). They are presented in appendix C.1. Here, the slant range r is the (shortest, linear) distance between the center of the acoustic transceiver and the target. It is the product of the <u>harmonic mean sound velocity</u> and the one-way propagation time of the acoustic signal.
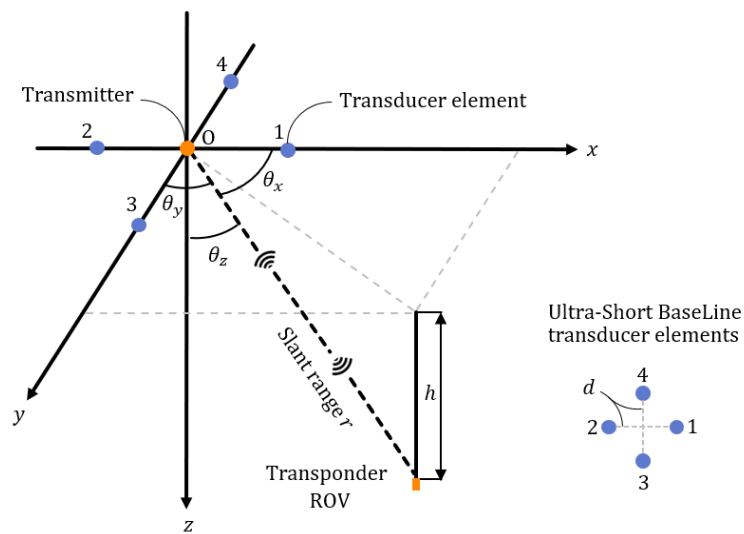
Figure 2.1 Schematization of the Ultra-Short BaseLine structure based on four transducer elements.
Redrawn from Tong *et al.* (2019).

Since the harmonic mean is a crucial concept in understanding the techniques applied in the inversion methods presented in this thesis, we introduce the concept with a straightforward calculation and make the translation to the harmonic mean sound velocity as applied in ocean acoustics.

2.1.1 The harmonic mean sound velocity

In ocean acoustics one often wants to calculate the distance a sound pulse will travel in a given amount of time. This requires knowledge of the mean sound velocity. However, for a given SVP one cannot simply average the

sound speeds over each depth layer to obtain the proper mean sound velocity. This depth-weighted mean sound velocity does not produce the correct average. Instead, one must divide the total depth by the sum of the time it takes for the sound to pass through each depth layer of constant sound speed (Schmidt, 2012). This is called the <u>harmonic mean</u> (Ferger, 1931).

More formally, the harmonic mean sound velocity is defined as the reciprocal of the arithmetic mean of the reciprocals of each sound speed per depth layer. In mathematical terms, the (unweighted) mean harmonic sound velocity c_H is defined as (Ferger, 1931):

$$c_H = \frac{n}{\frac{1}{c_0} + \frac{1}{c_1} + \cdots + \frac{1}{c_n}} = \frac{n}{\sum_{i=1}^{n} \frac{1}{c_i}} = \left(\frac{\sum_{i=1}^{n} c_i^{-1}}{n} \right)^{-1} \qquad 2.1$$

Here, n is the number of sound velocity measurements with depth. If these measurements are equidistantly distributed over the vertical (with depth increments of $1\ m$), then n also represents the total distance. In such case, all sound velocity measurements have equal weights (i.e. unweighted). If the measurements are unequally distributed, weights must be applied to scale the sound velocity measurement with its travelled distance. The weighted harmonic mean sound velocity is defined as (Ferger, 1931):

$$c_H = \frac{\sum_{i=1}^{n} |\Delta z_i|}{\frac{|\Delta z_0|}{c_0} + \frac{|\Delta z_1|}{c_1} + \cdots + \frac{|\Delta z_n|}{c_n}} = \frac{\sum_{i=1}^{n} |\Delta z_i|}{\sum_{i=1}^{n} \frac{|\Delta z_i|}{c_i}} \qquad 2.2$$

Intermezzo 2.1 provides a simple demonstration for the calculation of the harmonic mean sound velocity in a two-layered media, followed up by a practical example of the harmonic mean as required for the calculation of the slant range.

Intermezzo 2.1 Calculation of the harmonic mean sound velocity

_____

The calculation of the harmonic mean is best demonstrated with a simple example as shown in Figure 2.2. Consider a two-layered water column of $2\ km$ depth with a different sound velocity per layer:

- From 0-1000 m the sound velocity is $c = 2000\ m/s$;
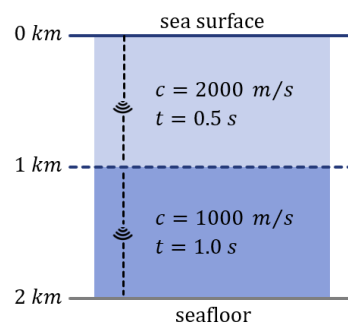- From 1000-2000 m the sound velocity is $c = 1000\ m/s$.

Figure 2.2 Example of nonconstant sound velocity in (strange) water column. Redrawn from Van den Berg (2021).

What is the average sound velocity of a sound pulse traveling from the sea surface to the seafloor? The correct average is the harmonic mean: 1333.33 m/s (and not the arithmetic mean 1500 m/s!).

It can be proven as follows:

$$\text{Average velocity} = \frac{\text{Total distance traveled}}{\text{sum of time for each segment}} = \frac{2D}{\frac{D}{c_1} + \frac{D}{c_2}} = \frac{2 \cdot 1000}{\frac{1000}{2000} + \frac{1000}{1000}} = \frac{2000}{0.5 + 1.0} = 1333.33 \; m/s$$

As a more practical example, the harmonic mean sound velocity is calculated for an SVP from $z = 8 \; m$ (relative depth of the USBL transducer to the sea surface) towards $z = 61 \; m$, shown in Figure 2.3. Using Eq. [2.2], the harmonic mean sound velocity is $c_H = 1489.73 \; m/s$. Physically, it means that the time it takes to travel the 53 meters is the same for a sound pulse propagating with a velocity that varies over depth (black line) and for a sound pulse propagating with a constant harmonic mean sound velocity (orange dashed line). The harmonic mean sound velocity – as appearing in the slant range calculation – is thus a simplified representation of the actual SVP.
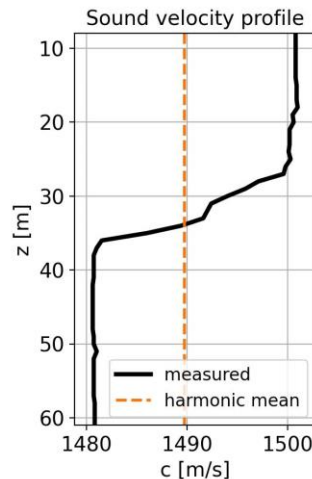

Figure 2.3 SVP (black line) measured on board of Van Oord's flexible fallpipe vessel Stornes in the North Sea; harmonic mean sound velocity (orange dashed line).

2.1.2 Ray trace modeling of sound propagation

Because refraction of the ray's path is <u>not</u> corrected for in the USBL model, we should apply an acoustic ray-tracing method. A ray-tracing algorithm enables us to estimate the trajectory of the ray's path. It accounts for bending (refracting) of the acoustic pulse due to vertical variations of the sound velocity.

In the remaining of the chapter, we consider two ray-tracing algorithms:

1. **The Equal Gradient ray-tracing algorithm (paragraph 2.2):** a conventional method that <u>subsequently</u> calculates the ray's displacements from the transceiver head by breaking down the SVP (Lu *et al.*, 2012; Hovem, 2013; Li *et al.*, 2018)**.**
2. **The Equivalent Sound Velocity Profile (ESVP) ray-tracing algorithm (paragraph 2.4):** a direct ray-tracing method that follows from the Equal Gradient ray-tracing algorithm. The ESVP ray-tracing algorithm can <u>directly</u> calculate the ray's displacements, using a simplified (though equivalent) representation of the actual SVP (Lu *et al.*, 2012; Xin *et al.*, 2018; Bu *et al.*, 2021). Paragraph 2.3 explains the relationship between the actual SVP, the ESVP and the harmonic SVP.

The ESVP ray-tracing algorithm will be used in the **HISOM methods** (chapter 3) for USBL positioning by directly calculating the (horizontal) displacements with the approximated SVP. In the **OMBES method** (chapter 4), we use the ESVP ray-tracing algorithm the other way around. The harmonic mean sound velocity is inverted by minimizing the vertical displacements from overlapping multibeam data. Subsequently, the harmonic mean is used for USBL positioning, again by using the ESVP ray-tracing algorithm.

2.2 Derivation of Equal Gradient Ray-Tracing Algorithm

This section provides expressions for an estimate of the ray's vertical and horizontal displacement for a layered media where the sound velocity varies with depth. The derivation is based on the assumption that the relationship between the sound velocity and the depth is linear in each depth layer (e.g. equal gradient), and that the trajectory of the sound wave in each depth layer is an arc segment (Li *et al.*, 2018). Figure 2.4 shows a schematization of the Equal Gradient ray-tracing principle.

Starting with the sound velocity gradient g $[s^{-1}]$:

$$g(z) = \frac{dc(z)}{dz} \tag{2.3}$$

According to Snell's law, when the sound speed varies with depth, the ray angle θ is a function of depth. It implies that the ray paths will bend and the rays propagate along curved paths (Hovem, 2013). Snell's law is expressed by:

$$p = \frac{\sin\theta(z)}{c(z)} = \frac{\sin\theta_s}{c_s} \tag{2.4}$$

where p is Snell's constant. The subscript 's' indicates the values at surface level (e.g. at the transducer head of the USBL or MBES).
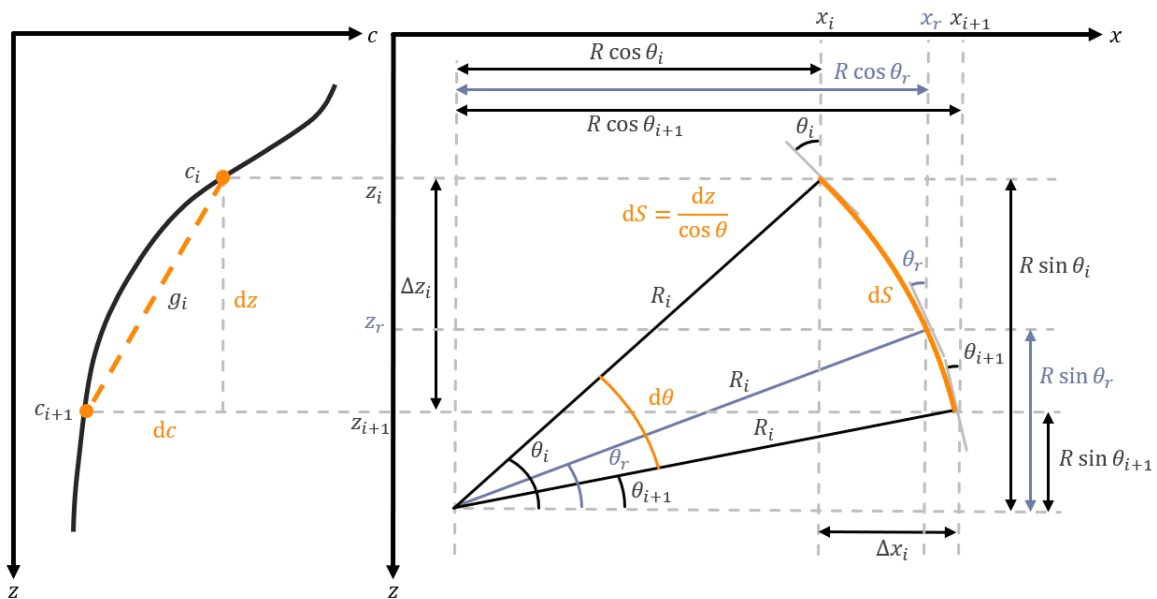

Figure 2.4 Schematization of Equal Gradient ray-tracing method

The curved paths are circular arcs. The radius of curvature R $[m]$ is defined as the ratio between an increment in the arc length dS and an increment in the angle $d\theta$ (Hovem, 2013):

$$R = \frac{dS}{d\theta} = \frac{1}{\cos\theta(z)}\frac{dz}{d\theta} \tag{2.5}$$

Differentiating Eq. [2.4] with respect to the ray angle θ gives the ray's radius of curvature at depth z. But first we rewrite Eq. [2.4]:

$$c(z) = \frac{c_s}{\sin \theta_s} \sin \theta(z)$$

2.6

Now differentiate Eq. [2.6] with respect to θ_z and rewrite:

$$\frac{\mathrm{d}c(z)}{\mathrm{d}\theta} = \frac{\mathrm{d}c}{\mathrm{d}z}\frac{\mathrm{d}z}{\mathrm{d}\theta} = \frac{c_s}{\sin \theta_s} \cos \theta(z)$$

$$\mathrm{d}\theta_z = \frac{\sin \theta_s}{c_s} \frac{1}{\cos \theta(z)} \mathrm{d}c(z)$$

2.7

Substitution of Eq. [2.7] in Eq. [2.5] to obtain the radius of curvature at depth z:

$$R(z) = \frac{1}{\cos \theta(z)}\frac{\mathrm{d}z}{\mathrm{d}\theta} = \frac{c_s}{\sin \theta_s}\frac{\mathrm{d}z}{\mathrm{d}c(z)} = \frac{1}{pg(z)}$$

2.8

From Eq. [2.8] we infer that:

- when $g > 0$ then $R > 0$ i.e. upward refraction of the ray;
- when $g < 0$ then $R < 0$ i.e. downward refraction of the ray.

In the schematization of Figure 2.4, $g = \mathrm{d}c/\mathrm{d}z < 0$, so downward refraction indeed. In fact, sound waves bend away from the layers with high sound speed and bend towards the layers with low sound speed (e.g. sound is lazy). This is illustrated in Figure 2.5.
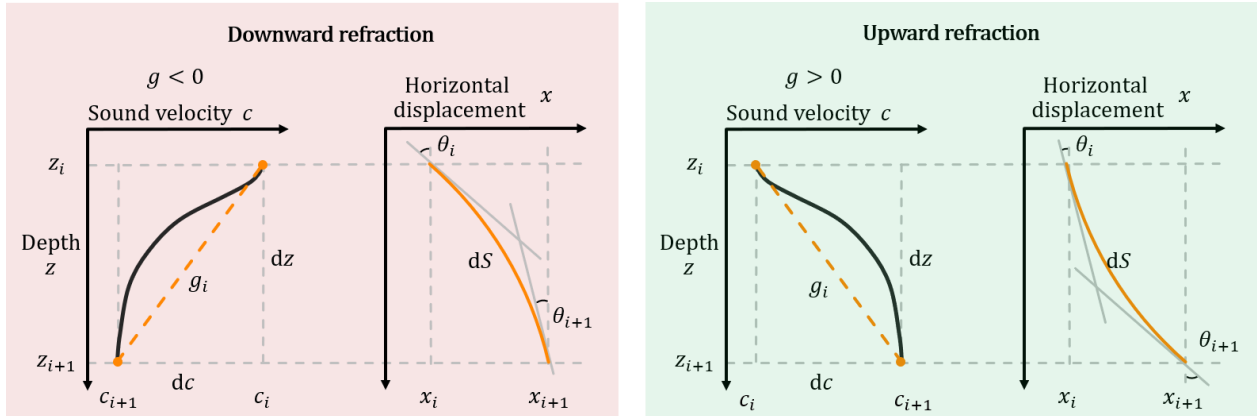
Figure 2.5 Schematization of downward and upward refraction for depth layer i with the Equal Gradient ray-tracing method

Assuming that the sound speed changes with a constant gradient g_i in each depth layer i, the sound velocity function is the next layer is expressed as:

$$c_{i+1}(z) = c_i(z) + g_i(z_{i+1} - z_i) = c_i(z) + g_i \Delta z_i$$

2.9

From the model in Figure 2.4, expressions for the vertical displacement Δz $[m]$, horizontal displacement Δx $[m]$, and the propagation time t $[s]$ per depth layer i can be derived, which form the basis for the Equal Gradient ray-tracing algorithm (Lu *et al.*, 2012; Xin *et al.*, 2018). A detailed derivation can be found in appendix A.1.

$$\begin{cases} \Delta z_i = R_i(\sin\theta_{i+1} - \sin\theta_i) & \text{2.10} \\[2mm] \Delta x_i = R_i(\cos\theta_i - \cos\theta_{i+1}) & \text{2.11} \\[2mm] t_i = \dfrac{\theta_{i+1} - \theta_i}{g_i(\sin\theta_{i+1} - \sin\theta_i)}\ln\left(\dfrac{\sin\theta_{i+1}}{\sin\theta_i}\right) & \text{2.12} \end{cases}$$

Once the pulse reaches the seafloor at depth layer r (e.g. receiver depth z_r, see Figure 2.4, highlighted in blue), the expressions are:

$$\begin{cases} \Delta z_r = R_i(\sin\theta_r - \sin\theta_i) & \text{2.13} \\[2mm] \Delta x_r = R_i(\cos\theta_i - \cos\theta_r) & \text{2.14} \\[2mm] t_r = \dfrac{\theta_r - \theta_i}{g_i(\sin\theta_r - \sin\theta_i)}\ln\left(\dfrac{\sin\theta_r}{\sin\theta_i}\right) & \text{2.15} \end{cases}$$

Since the remaining θ_r is <u>unknown</u>, in order to calculate Δz_r and Δx_r, the angle θ_r is based on the remaining time t_r, which is expressed as the total propagation time t minus the sum of times of the above layers (Lu et al., 2012):

$$t_r = t - \sum_{j=1}^{i-1} t_j = \frac{\theta_r - \theta_i}{g_i(\sin\theta_r - \sin\theta_i)}\ln\left(\frac{\sin\theta_r}{\sin\theta_i}\right)$$

$$t_r = t - \sum_{j=1}^{i-1} \frac{\theta_{j+1} - \theta_j}{g_j(\sin\theta_{j+1} - \sin\theta_j)}\ln\left(\frac{\sin\theta_{j+1}}{\sin\theta_j}\right) = \frac{\theta_r - \theta_i}{g_i(\sin\theta_r - \sin\theta_i)}\ln\left(\frac{\sin\theta_r}{\sin\theta_i}\right) \qquad \text{2.16}$$

To obtain the remaining t_r from Eq. [2.16], one has to subsequently loop over all above layers to calculate the sum of times, followed by subtraction of this sum from the total propagation time t. Next, an iterative approach is required to approximate the remaining angle θ_r because it cannot be written in a direct form i.e. it appears three times on the right-hand side of the equation in quite complicated mathematical functions. This calculation procedure can be used for USBL positioning but is rather unpractical for massive multibeam bathymetry data due to the large number of iterations (e.g. number of beams is usually 256 or 1024). In addition, it introduces a certain truncation error. Therefore, we aim for a more direct calculation procedure.

2.3 Equivalent Sound Velocity Profile and Harmonic Mean Sound Velocity Profile

In the previous section, a set of equations are derived for calculating the <u>vertical displacement</u>, <u>horizontal displacement</u> and <u>propagation time</u> per depth layer, all based on the actual SVP and Snell's law of refraction. Even though the simplified model is capable of calculating the ray's path, it is quite complex to go through all depth layers. In addition, to calculate the remaining angle θ_r an iteration is required which complicates the algorithm, and makes the calculation process time-consuming (Lu *et al.*, 2012; Li *et al.*, 2018).

Geng and Zielinski (1999) proposed the <u>equivalent sound velocity profile (ESVP) method</u> to omit the iterative calculation procedure. They showed that for the same propagation time, the horizontal displacement (i.e. the location at which the acoustic pulse impinges on the seafloor) is almost the same for a family of SVPs (Geng and Zielinski, 1999). Required is these SVPs have the same sound velocity at surface level c_s and the same area under

them (e.g. integral). Therefore, a <u>constant</u> sound velocity gradient [4] $\boldsymbol{g}$ can be used instead of the actual profile in order to simplify the calculation (Zhang *et al.*, 2022).

The <u>harmonic mean sound velocity profile</u> is an extreme member of this family. The harmonic mean sound velocity follows directly from the ESVP, and it is the exact same harmonic mean sound velocity being used in the USBL positioning equations (see appendix C.1). However, we faced that the USBL positioning model does not correct for refraction errors when using the harmonic mean sound velocity. In order to land at the same spot at the seafloor, a correction for refraction must be applied. It requires a measurement of the surface sound velocity c_s, and introduction of an infinitesimal depth layer in the harmonic sound velocity profile to correct for refraction. This new layer goes from the surface sound velocity c_s to the harmonic mean sound velocity c_H, and has a very large sound velocity gradient $g = \mathrm{d}c/\mathrm{d}z$. An illustration of these simplified profiles is given in Figure 2.6. A proof that the areas under the profiles are equal is given in appendix A.2.
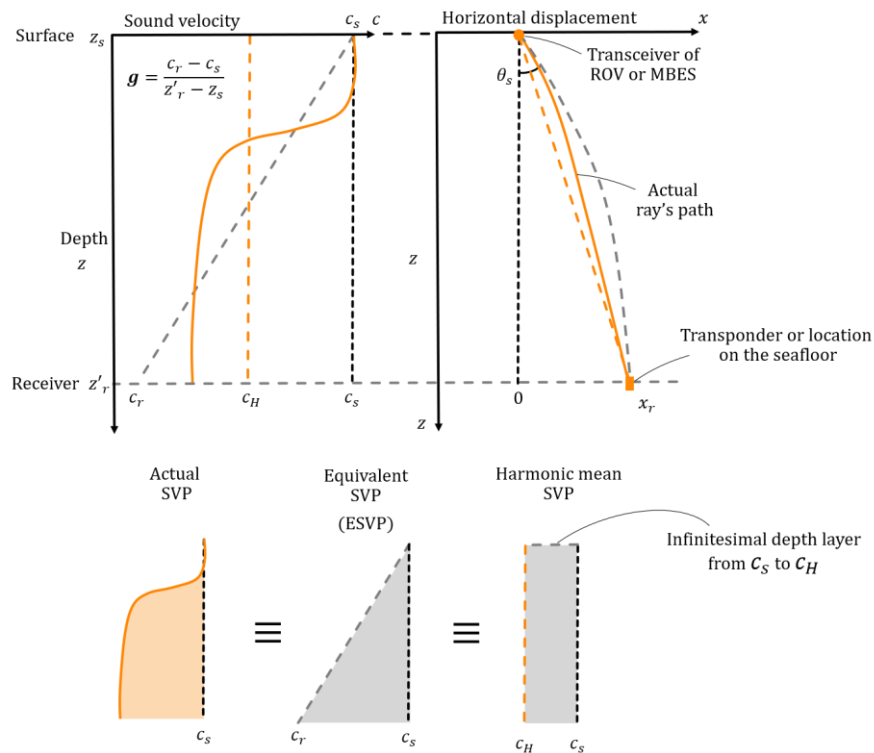
Figure 2.6 Relationship between the actual SVP, the equivalent SVP, and harmonic mean SVP and their ray's path.

The above highlights that the equivalent SVP and harmonic mean SVP can be used interchangeable to estimate the location of the ROV's transponder or the location where the acoustic pulse impinges on the seafloor.

From the geometry in Figure 2.6, and by using $c_r = 2c_H - c_s$, the constant sound velocity gradient $\boldsymbol{g}$ follows (see also appendix A.2):

$$\boldsymbol{g} = \frac{c_r - c_s}{z'_r - z_s} = \frac{2c_H - 2c_s}{z'_r - z_s} \qquad \text{2.17}$$

where c_s is the surface sound velocity i.e. the sound velocity at the transducer head of the USBL or MBES at surface depth level z_s.

---

[4] In the remaining, we will use a bold $\boldsymbol{g}$ for the constant sound velocity gradient associated with the constant gradient ESVP model, whereas $g = \mathrm{d}c/\mathrm{d}z$ refers to the sound velocity gradient for a small increment in the actual SVP.

An important note is that the receiver depth is an approximation of the true receiver depth z_r, denoted with the annotation " $'$ ". The approximated receiver depth z_r' has two different meanings depending on the application:

- *z_r' is the depth location of the ROV's transponder*:
  For ROV positioning with USBL (chapter 3), the receiver depth is unknown and what we are after. As will become clear in paragraph 2.4, the constant sound velocity gradient $\boldsymbol{g}$ can be used to directly calculate the ROV's position. However, the constant gradient itself depends on the unknown receiver depth (see Eq. [2.17]). Therefore, we must provide a first estimate of the depth location of the ROV's transponder. One way is to use the USBL principle equations, where the effect of refraction is neglected (see appendix C.1):

$$z_r' = r \cos \theta_z \qquad \text{2.18}$$
$$r = c_H t \qquad \text{2.19}$$

  where r is the slant range, the product of the harmonic mean sound velocity c_H and the one-way propagation time of the acoustic signal t. The harmonic mean sound velocity can be calculated using Eq. [2.2] based on the measured SVP. θ_z is the incident angle with respect to the vertical axis.

  Alternatively, depth information can be obtained from pressure sensors (Wang *et al.*, 2018). The depth level is obtained on the difference in hydrostatic pressure: one sensor mounted on the framework of the ROV measures the water pressure, and one sensor on the vessel measures the atmospheric pressure.

- *z_r' is the average depth location of the seafloor:*
  For inversion of the harmonic mean sound velocity from overlapping multibeam data (chapter 4), the constant gradient $\boldsymbol{g}$ that is unknown, while minimization of the mismatch in depth estimates already provides an estimate of the receiver depth z'_r. Here, the receiver depth denotes the average depth of the seafloor. Once the constant gradient $\boldsymbol{g}$ is optimized, it can be used to directly locate the ROV.

As already described, the use of the ESVP and its constant gradient $\boldsymbol{g}$ allow a direct ray-tracing method that omits the complex iteration procedure! It will be presented in the next paragraph.

2.4 Derivation of ESVP Ray-Tracing Algorithm

In case of a constant sound speed gradient $\boldsymbol{g}$, a direct expression can be derived for the time at receiver depth t_r (Lu *et al.*, 2012). A detailed derivation is given in appendix A.3.

$$t_r = \frac{1}{g_i} \ln \left(\frac{\tan(\theta_r/2)}{\tan(\theta_i/2)} \right) \qquad \text{2.20}$$

From Eq. [2.20] we can directly obtain the angle at receiver depth:

$$\theta_r = 2 \arctan(e^{t_r g_i} \tan(\theta_i/2)) \qquad \text{2.21}$$

Compare this result with Eq. [2.16]. In this way, no iteration is required!

Since we consider a constant gradient $\boldsymbol{g}$, the remaining angle θ_r can be found using the incident sending angle θ_s and the time measurement t (half of the one-way travel time):

$$\theta_r = 2 \arctan(e^{tg} \tan(\theta_s/2)) \qquad \text{2.22}$$

Now, using Eq. [2.22], the vertical displacement z_r in Eq. [2.13] and horizontal displacement x_r in Eq. [2.14] can be directly calculated:

$$z_r' - z_s = R(\sin\theta_r - \sin\theta_s) = \frac{\sin(2\arctan(e^{tg}\tan(\theta_s/2))) - \sin\theta_s}{pg} \qquad 2.23$$

$$x_r = R(\cos\theta_s - \cos\theta_r) = \frac{\cos\theta_s - \cos(2\arctan(e^{tg}\tan(\theta_s/2)))}{pg} \qquad 2.24$$

Eq. [2.23] and Eq. [2.24] are the basic formulas for calculation of the displacements based on the ESVP that uses a constant gradient g.

The only ingredients needed to calculate the displacements are (for the application of MBESs and USBL positioning systems):

- t [s], half of the two-way travel time of the acoustic signal, recorded by the multibeam/USBL transducers;
- g [s^{-1}], constant sound velocity gradient of the ESVP (Geng and Zielinski, 1999);
- θ_s [°], incident ray angle at multibeam/USBL head, measured at surface level z_s;
- $p = \sin\theta_s/c_s$, Snell's constant, where c_s [m/s] is the surface sound speed at measured at surface level z_s with a sound velocity sensor integrated or close to the multibeam/USBL head device.

This ray-tracing algorithm allows to calculate the vertical and horizontal displacement in one step.

Van Oord
Marine ingenuity

3. HISOM METHODS

The methods presented in this chapter apply to fallpipe ROVs (FPROVs). Such an ROV is attached to a string of buckets. When the ROV is steadily lowered towards the sea bottom, a constant supply of buckets is fed by a combination of winches and cables (Figure 3.1). This unique flexible fallpipe system together with the powerful ROV allow the contractor to install rock with high accuracy and efficiency i.e. subsea rock installation (SRI) projects (Figure 3.2).

The bucket system makes the fallpipe flexible. As a consequence, the FPROV will always drift off in the presence of currents. In order to correct for drifts and to arrive at the designated work area (e.g. straight above a pipeline), the pilot on board will maneuver the FPROV with its integrated thrusters.

Though, the flexibility of the fallpipe is limited. As a rule of thumb, the maximum horizontal offset of the FPROV from the transceiver is no more than 10% of the water depth. This comes down to a maximum angular range of $-6° < \theta_s < 6°$, where θ_s is the incident angle with the normal at surface depth. Van Oord's fleet of SRI vessels can place rock at a maximum depth of $1500m$,

Figure 3.1 String of buckets of flexible fallpipe on board of vessel Nordnes. Image: Van Oord (2021).

and thus a maximum offset of $150m$. Because of the small incident angles at which FPROV operate, refraction will be limited when sending an acoustic signal between the transceiver and the transponder. Hence, if an erroneous SVP is used, the refraction-induced horizontal positioning error is limited. Or stated differently, the use of erroneous SVPs will be less penalizing.

Figure 3.2 Left: schematization of Van Oord's SRI vessel Bravenes and the flexible FPROV. Right: schematization of two methods presented in this chapter. The CSSV method uses the ISS sound velocity and considers it to be constant with depth. The MSVP method uses the ISS sound velocity in combination with the model-based SVP.

Since measuring the SVP is an expensive procedure, it would be interesting to know what refraction error will be introduced when neglecting the actual (complex) SVP. Instead, an in situ sound velocity measurement c_s is used, measured under the hull of the vessel at surface depth z_s. Here, the surface depth z_s is defined as the depth at

which the transceiver is located. Next to the transceiver, other instruments are mounted on the vessel, such as an ADCP, MBES with integrated sound velocity sensor. The sound velocity sensor provides continuous updates of the sound velocity at surface depth, necessary for accurate determination of the beam angles at the transducer multibeam head. It is not common practice to use the In Situ Surface (ISS) sound velocity for USBL positioning. However, it can be measured easily and provide useful information. To this end, we analyze the potential application of using surface level sound velocity information for the acoustic positioning of FPROVs.

This chapter presents <u>two variants</u> that are based on HISOM. Both methods apply to FPROVs. The CSSV method (Constant Surface Sound Velocity) – presented in paragraph 3.3 – investigates under what conditions it is valid to neglect the actual SVP for the case of underwater acoustic positioning with small incident angles ($\theta_s < 6°$). These conditions include the spatiotemporal stratification of the SVP, and the depth of the geographical sea location. Instead of using the actual (complex) SVP (orange profile, Figure 3.2), the ISS sound velocity is considered constant between the transceiver and the transponder (zero-gradient profile, black dotted line, Figure 3.2). This will inevitably introduce refraction errors. The question is whether these errors matter given the error budget requirements. Depending on their value, they may be (un)acceptable for offshore application. The hypothesis is that sea areas exist where the depth is not sufficient for the refraction error to grow large enough with the consequence of passing a tolerance threshold. Despite the high degree of stratification, the (shallow) depths limit the error to grow problematically in terms of positioning accuracy. When operating in these sea areas with SRI vessels, it suffices to consider the ISS sound velocity as being constant with depth.

The MSVP method (Model-based Sound Velocity Profile) – presented in paragraph 3.4 – also neglects the actual SVP but instead estimates the SVP from freely-available ocean model data. The model-based estimates of the SVP – in combination with the ISS sound velocity – are used to determine the position of the FPROV (Figure 3.2). The hypothesis is that the model-based estimates are accurate enough for underwater acoustic positioning due to the fact that FPROVs operate at small incident angles.

The sea area of interest is the North Sea (Figure 3.3). It is a marginal, shallow sea on the European continental shelf. The North Sea is one of the most heavily used seas worldwide, with resulting competition between marine shipping, food supply, energy, nature and recreation. Van Oord is active in the North Sea's energy sector by constructing offshore wind farms and energy islands, cable-laying activity and subsea rock installation for the oil and gas infrastructure.

The North Sea is seen as breeding ground for innovation with further development of offshore wind energy, the electrification of oil and gas platforms, and the offshore production of green hydrogen and its transport to land (Peters, 2020). With increasing activity offshore, underwater acoustic positioning systems will be used more frequently. Along with their deployment comes the demand for reliable SVP information, that determines the accuracy of these systems. However, the hypothesis states that sea areas exist where one can get away with surface information only. Therefore the question is whether profile information is really needed. For the assessment one

Figure 3.3 Map of the North Sea (Halava, 2010)

must examine what part refraction-induced positioning errors play. The error analysis helps to assess at what time

of the year and where in the North Sea the contractor should take an SVP, and when and where the contractor can rely on the ISS sound velocity.

For the assessment of the HISOM methods, we use empirically-derived SVPs from freely-available ocean model data (3D-temperature and -salinity data). The 3D sound velocity data serves as input for the refraction-induced positioning error analysis, and enables us to assess where and when in the North Sea it is valid to neglect the actual SVP and instead consider the surface sound speed as being constant with depth. The model-based SVPs are later used for the MSVP method. In order to assess whether the model-based SVPs are reliable estimates, observed SVPs collected by Van Oord's Stornes SRI vessel were analyzed for this sea area. The set includes 72 SVPs from 13 SRI projects executed in the North Sea between June and November in the year 2020.

The chapter outline is as follows: paragraph 3.1 explains in detail the data source and how the data can be accessed. In paragraph 3.2, an empirical relation is presented that calculates the sound velocity based on temperature, salinity and depth. To understand how the sound velocity varies in time and space, the dominating physical processes at work in the North Sea are examined that are responsible for variations in temperature and salinity. Next, the translation to the spatiotemporal variability of the sound velocity is made. Paragraph 3.3 presents how to proceed from SVPs to refraction errors and assesses the performance, applicability and validity of the CSSV method for the North Sea based on model data and observations. At last, paragraph 3.4 shows the performance of the MSVP method based on observations.

3.1 Data Sources and Access

For the assessment of both methods, we use free-of-charge-and-state-of-the-art ocean data from the Copernicus Marine Environment Monitoring Service (CMEMS). The CMEMS is funded by the European Commission (EC) and operationally implemented by Mercator Ocean International. The system provides different products for observations and model outputs covering ocean physics, sea-ice state and biochemistry. The capacity encompasses the description of the current situation (analysis), the prediction of the situation 10 days ahead (forecast), and the provision of retrospective

Figure 3.4 Snapshot of the dynamic interface of CMEMS MyOcean Viewer (Copernicus Marine Service, 2022). 3D potential sea water temperature (thetao) is selected of the Operational Mercator global ocean forecast system.

data (reanalysis). A major objective of the CMEMS is to cater the needs of public and private users for global ocean knowledge, and to boost the blue economy across maritime sectors by providing ocean data and information (le Traon *et al.*, 2019). The ocean products can be viewed online interactively (see Figure 3.4).
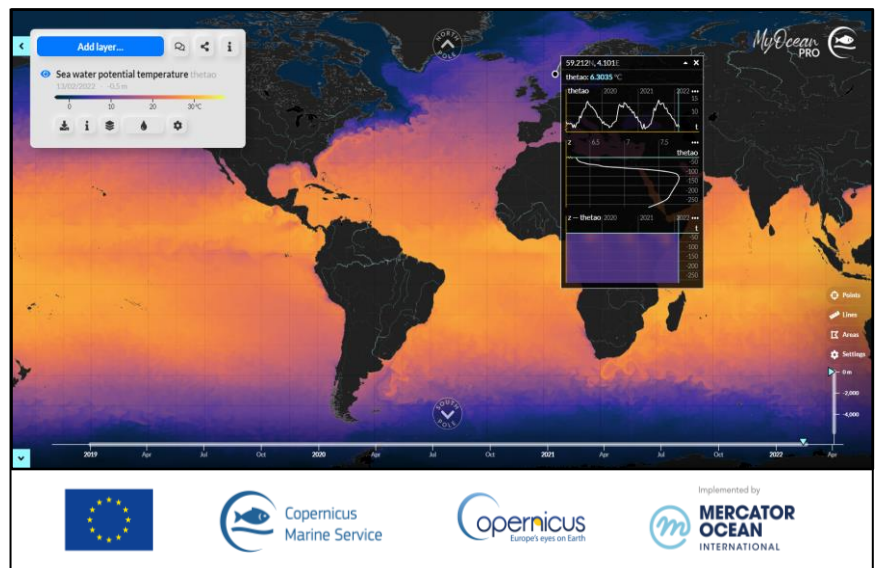
For this thesis, the CMEMS global ocean product GLORYS 12V1 is selected. It is an eddy-resolving global ocean simulation model constrained by assimilation of observations (Drévillon, Fernandez and Lellouche, 2021). GLORYS 12V1 describes the spatio-temporal evolution of 3D thermodynamic variables (temperature, salinity), 3D dynamic variables (eastward and northward velocities), altimeter data and sea-ice features (fraction, thickness and velocities). Data assimilation allows to interpolate different types of observations, and to include derived parameters that are not directly observed (le Traon *et al.*, 2019). The product uses an equirectangular grid at

$1/12°$ ($\sim 9.25 km$) horizontal resolution and 50 standard depth levels from $-5500\,m$ to $0\,m$. It is organized in three datasets: daily mean fields, monthly mean fields, and monthly climatology mean fields. The temporal coverage is from 01-01-1993 to 31-12-2019. The freely-available ocean data from GLORYS 12V1 is of interest for empirical estimation of the 3D sound velocity, as the model has global coverage of the dependent thermodynamic variables (temperature and salinity), resolved on a high-resolution grid for a long time period.

This thesis uses a subset of 3D-temperature and -salinity data including the North Sea and ranges from 48°N to 62°N degree latitude and from 12°W to 11°E degree longitude. The most recent 10-year period is chosen from 01-01-2010 to 31-12-2019, long enough for a proper estimate of the mean SVP and recent enough to include climatological changes. The fields are daily means, centered at noon. Table 3.1 summarizes the data request.

Product	Requested variables		Geographical area		Time range	
			Latitude	Longitude	Start data	End data
GLORYS 12V1	T [℃] sea water potential temperature	S [PSU] sea water salinity	48°N - 62°N	12°W - 11°E	01-01-2010 12:00:00	31-12-2019 12:00:00

Table 3.1 CMEMS global ocean product GLORYS 12V1 data request overview.

The downloaded file including the 10-year-daily mean 3D- temperature and -salinity field account for 4.67 Gb. The dataset is downloaded remotely by creating a connection via an Application Programming Interface (API) MOTU Client. More information on the data access via MOTU Client is given in appendix B.

3.2 Sound Velocity Data

Using the 3D-temperature and -salinity matrices from GLORYS 12V1, the sound velocity can be calculated with an empirical model according to temperature, salinity and depth (pressure) (Zhang, Xu and Gao, 2018). With use of the 10-year-daily-mean 3D-temperature and -salinity data, an estimate of the 3D sound velocity is provided for a representative year in the sea area of interest.

3.2.1 Empirically-derived sound velocity data

In literature, there are several empirical equations that calculate the sound velocity from temperature, salinity and depth (Talib *et al.*, 2011; Zhang, Xu and Gao, 2018). They differ in accuracy and range of applicability. This thesis uses the popular and accurate empirical equation of Medwin. Medwin's relation for the speed of sound is valid for a realistic combinations of temperature T (0 to 35℃), salinity S (0 to 40 ppt ($\cong$ PSU)), and depth z (0 to 1000 m). It reads (Medwin, 1975):

$$c = 1449.2 + 4.6\text{T} - 5.5 \cdot 10^{-2}\text{T}^2 + 2.9 \cdot 10^{-4}\text{T}^3 + (1.34 - 0.017)(\text{S} - 35) + 0.016z \qquad 3.1$$

Table 3.2 gives a general impression about the effect of variations in temperature, salinity and depth, on the sound speed. From Table 3.2 follows that the sound speed is most sensitive to variations in temperature.

Variation	Medwin's relation for sound speed $[m/s]$
*Nominal Conditions**	**1497.02**
Temperature decrease/increase of **1.0**℃	$-4.66/+4.77$
Salinity decrease/increase of **1.0 PSU**	$-1.32/+1.32$
Depth decrease/increase of **1.0** m	$-0.02/+0.02$

Table 3.2 The effect of temperature, salinity and depth variation on the sound speed according to Medwin's empirical relation.

Applying Medwin's relation to the 4D (time and 3D-space) -temperature and -salinity data, a 4D array is constructed of the sound velocity. The dimensions are c(time, depth, latitude, longitude). Figure 3.5 shows the multidimensional model.
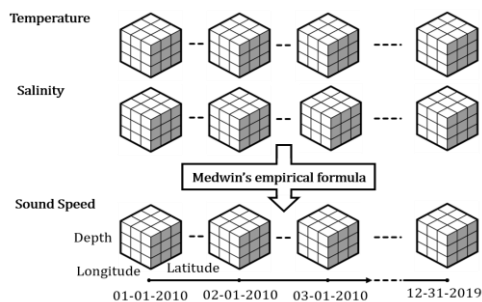

Figure 3.5 Multidimensional model of 4D-temperature and -salinity data, empirically converted into 4D sound speed data using Medwin's empirical relation.

3.2.2 Temperature, salinity and their variability in the North Sea

The previous section described that the sound velocity depends on temperature, salinity and depth. The daily-mean surface values for temperature, salinity and sound velocity are mapped in Figure 3.6 for July 1st, 2010.

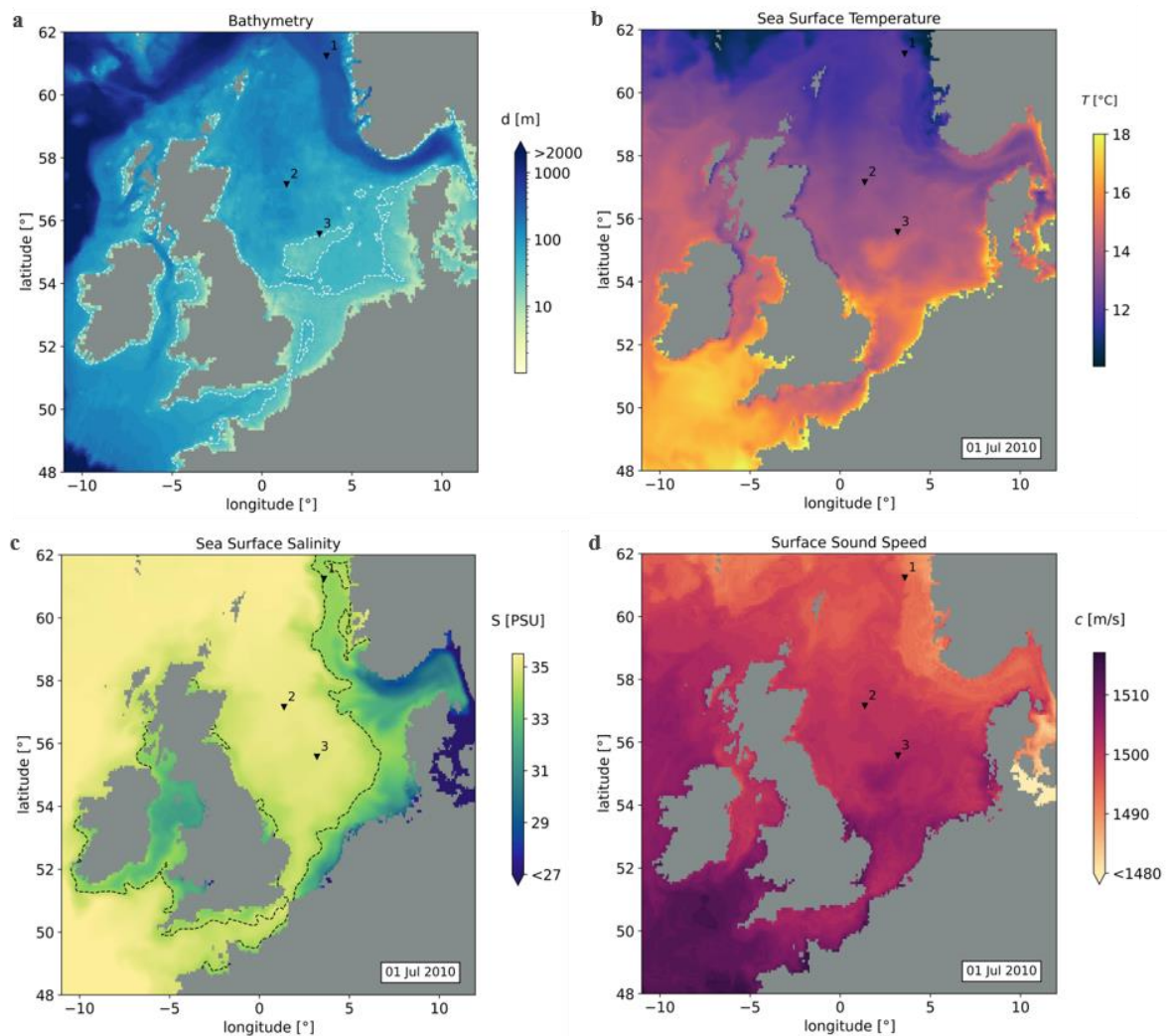**Figure 3.6** Color map of North Sea's **a)** bathymetry (white dashed line is the 40 m isobath); **b)** sea surface temperature; **c)** sea surface salinity (white dashed line is the 34 PSU isohaline); **d)** surface sound speed, daily-means of July 1st, 2010. Bathymetric data and thermodynamic variables from GLORYS 12V1, provided by Copernicus Marine Service. Sound speed empirically calculated using

In order to understand how the sound velocity varies in time and space, we must examine the dominating physical processes at work in the North Sea that are responsible for variations in temperature and salinity. Because the sound velocity is most sensitive to variations in temperature, much of the spatial features observed in surface temperature can be found in the pattern of the surface sound velocity (Figure 3.6b,d). In general it holds that the higher the temperature, the higher the sound velocity. But along some coastlines, the reduced salinity counteracts the effect of high temperatures on the sound velocity, while in the Kattegat and Skagerrak (Figure 3.3), the fresh inflow from the Baltic completely dominates the value of the sound velocity (Figure 3.6c,d). An overall schematic of the stratified conditions in the North Sea is given in Figure 3.7.
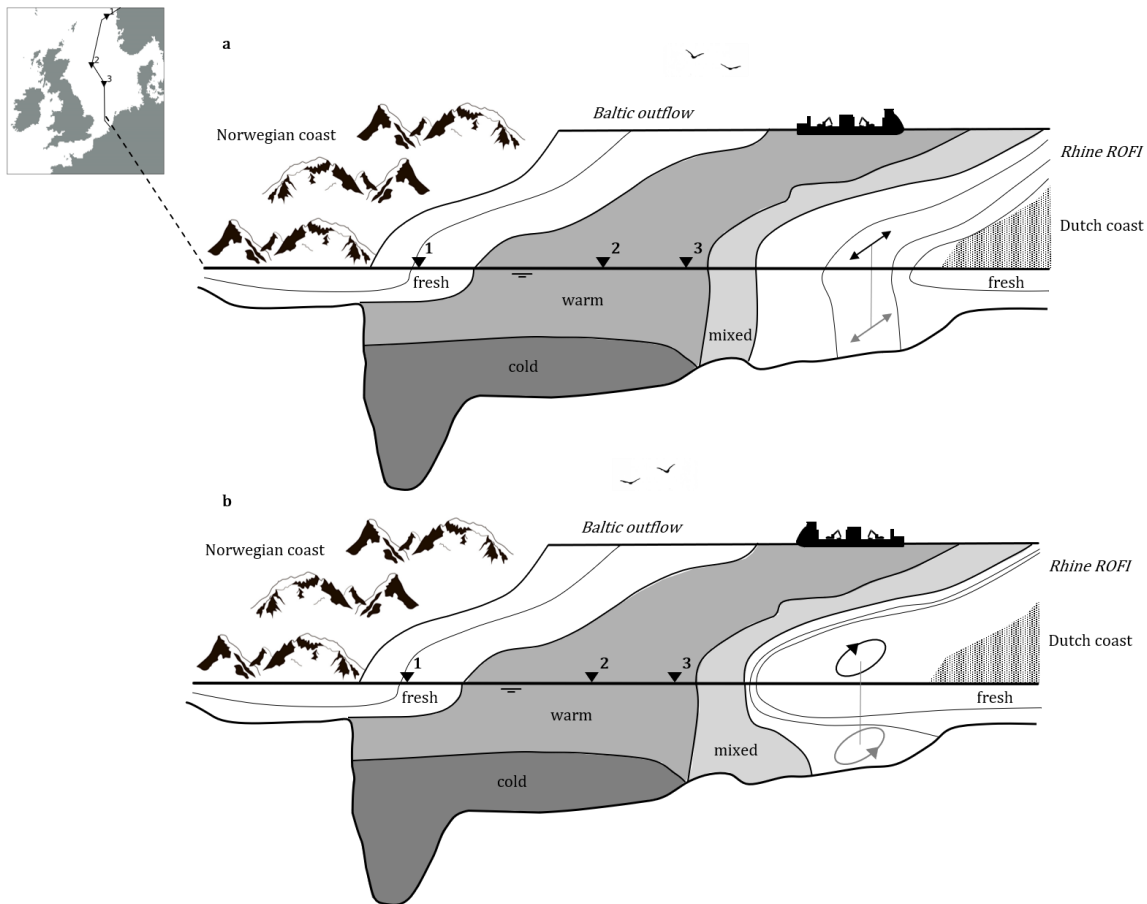

Figure 3.7 Schematization of stratified conditions in the North Sea**.** The Rhine ROFI **a)** during well-mixed conditions; **b)** during stratified conditions (after Simpson et al. 1990). The majority of the North Sea is dominated by seasonal thermal stratification cycle. The Norwegian coast is characterized by haline stratification as result of freshwater fluxes originating from the Baltic. The (Rhine) ROFI has a dominant fortnightly haline stratification cycle (de Boer, Pietrzak and Winterwerp, 2009).

The question remains what physical processes govern the variability of the sound speed's dependent variables in the North Sea? Basically, it comes down to a competition between buoyancy and stirring. Stirring occurs mainly due to tidal motions and the influence of winds. The two main sources of buoyancy are solar heating at the surface and freshwater run-off from rivers and fjords (Crawford, 2017):

- *Buoyancy input from heat*
  The majority of the North Sea is dominated by solar heating (Crawford, 2017). Because the buoyancy input from heat is relatively uniform in space, the observed differences in surface temperature can be linked to the water depth. In fact, the heat gain from the air depends on the thermal capacity, which

reduces with decreasing water depth (Clark, Webb and Ladle, 1999). Therefore, shallow areas are more sensitive to changes in air temperature. In these shallow areas, the heat is generally well-mixed throughout the water column due to the presence of tidal motions. In deeper sea areas where the tides have less of an impact, thermal stratification occurs as heat accumulates in the upper layers. According to Huthnance (1991), the $40m$ depth contour is approximately the bound where seasonal thermal stratification occurs in the North Sea (Figure 3.6a).

- *Buoyancy input from freshwater run-off*
  In contrast to the input from heat, the input of buoyancy from freshwater discharge is very localized in space and significantly contributes to salinity stratification. In particular, outflow from major rivers – such as the Rhine and Elbe – contribute to buoyancy input in coastal areas adjacent to estuaries (Crawford, 2017), known as regions of freshwater influence or ROFIs (Simpson, 1993). The extent of the ROFIs along the Dutch coast and the inner German Bight (Figure 3.3) depend on the amount of river discharge and compete with tidal and wind mixing to establish stratification (de Boer, Pietrzak and Winterwerp, 2009). Another major source of fresher inflow comes from the Baltic via the Skagerrak, which stream continuous north along the Norwegian coast.

3.2.3 Sound velocity and its variability in the North Sea

When we translate the variability of temperature and salinity to the variability of the sound velocity in the North Sea, we find that its value is largely characterized by seasonal variation due to solar heating. In coastal areas adjacent to estuaries, the sound velocity can differ locally depending on the competition between the freshwater input and stirring.

The constant sound velocity gradient

In order to assess how vertical stratification establishes and when it potentially will influence the SVP, we aim to plot the sound velocity gradient $g = \mathrm{d}c/\mathrm{d}z$, which is the change in sound velocity with depth. According to Snell's law, sound velocity gradients induce refraction of the ray path and cause the acoustic pulse to propagate along a curved trajectory. For a particular depth level – for instance the seafloor – the net effect of refraction can be summarized by a <u>constant</u> sound velocity gradient g. It the inverse of the slope in the ESVP (chapter 2). The constant sound velocity gradient can be used as measure of how stratified the water column is in terms of the sound velocity. Its relation to the actual SVP and the harmonic mean SVP was given in paragraph 2.3.

Based on the geometry in Figure 2.6, we recall that:

$$g = \frac{c_r - c_s}{z_r' - z_s} = \frac{2c_H - 2c_s}{z_r' - z_s}$$

3.2

where c_s is the surface sound velocity measured real-time under the hull of the vessel with a sound velocity sensor. c_H is the harmonic mean sound velocity at receiver depth z_r'. Here, we use the seafloor as receiver depth and assume the FPROV to be <u>close</u> to the seafloor. In practice, the FPROV maneuvers approximately 3 to 5 m above the seafloor. The harmonic mean sound speed c_H is calculated based on the model's SVP using Eq. [2.2] (paragraph 2.1).

Seasonal variation of the sound velocity

For July 1st, 2010, the harmonic mean sound velocity at the seafloor c_H is mapped in Figure 3.9b. Where the harmonic mean sound velocity (3.9b) differs from the surface sound velocity (3.9a), the SVP shows gradients $g = \mathrm{d}c/\mathrm{d}z$ that cause refraction of the ray's path. Using the constant sound velocity gradient g in a colormap

highlights to what extent the water column is stratified in terms of sound velocity. Its parameter scales the difference between the surface sound velocity c_S and the harmonic mean sound velocity c_H to depth. The constant sound speed velocity g is mapped in Figure 3.9c for July 1st, 2010, and in Figure 3.10 for January/April/July/October 1st based on the 10-year-mean, period 2010-2020. To our knowledge, it is the first time the constant sound velocity gradient is mapped in this way.
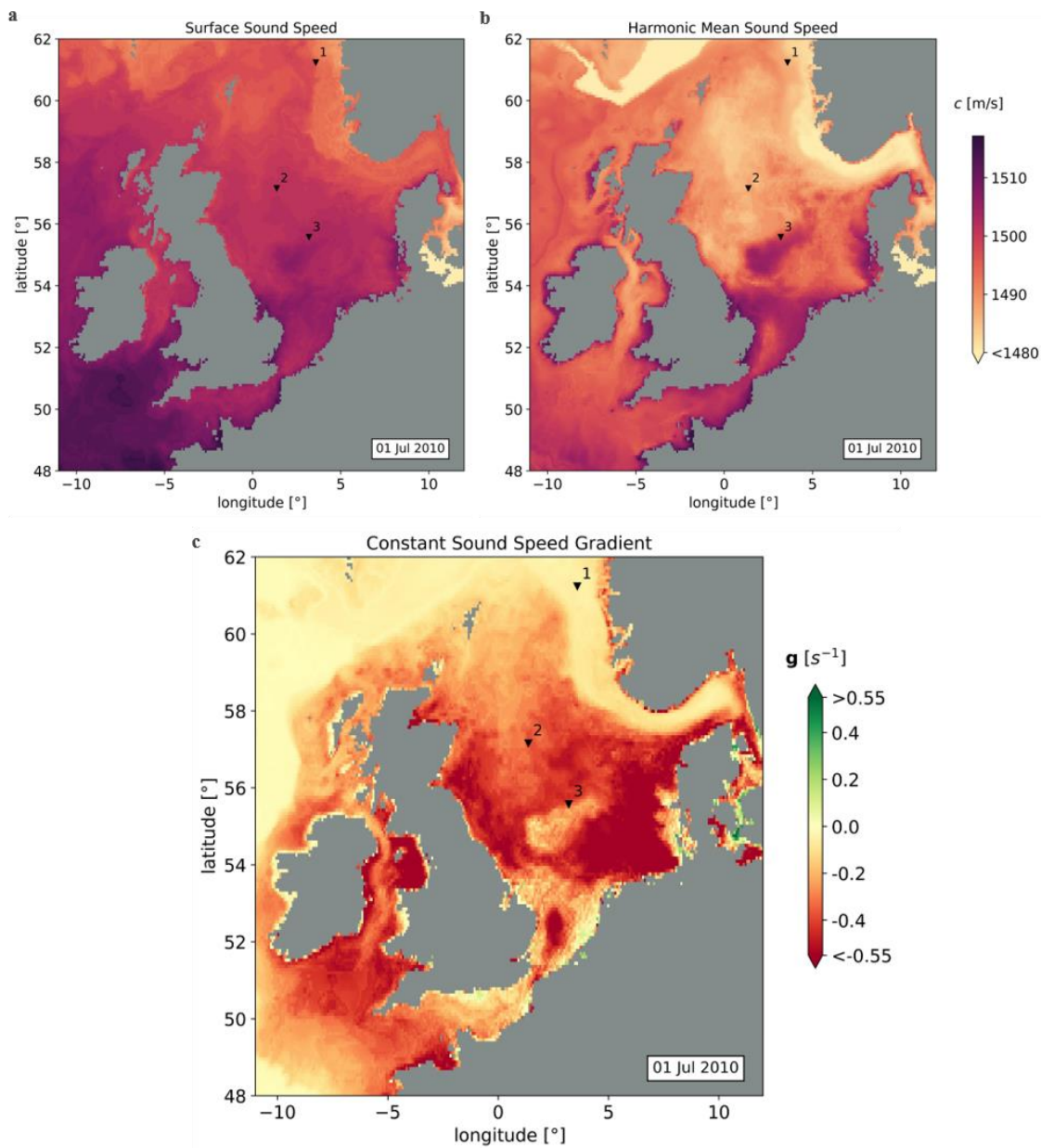

Figure 3.9 Color map of North Sea's **a)** surface sound speed; **b)** harmonic mean sound speed at the seafloor; **c)** constant sound speed gradient, daily-means of July 1st, 2010. Bathymetric data and thermodynamic variables from GLORYS 12V1, provided by Copernicus Marine Service. Sound speed empirically calculated using Medwin's relation. Black markers indicate installation location – that are used in paragraph 3.3 – where SVPs were taken by Van Oord's SRI vessel Stornes in the year 2020.

Figure 3.10 shows that the North Sea is characterized by significant variation in the constant sound speed gradient throughout the year. Its value knows three distinct cases. They are schematized in Figure 3.10 and explained in more detail:

- *When $g < 0$ then $c_S > c_H$ and we have net downward refraction of the ray (red color in Figure 3.10 & 3.11).*

This case is associated with thermal stratification, where the accumulated heat in upper water layers induce a thermocline that is responsible for a negative sound velocity gradient. In line with Huthnance (1991), thermal stratification occurs approximately for the $40m$ isobath in summer period (see Figure 3.10c). However, with increasing depth the effect of the thermocline is averaged out vertically: the constant sound velocity gradient decreases. Approximately for the $400m$ isobath – where the continental slope starts – the effect is negligible: the constant sound velocity gradient stays relatively stable throughout the year.
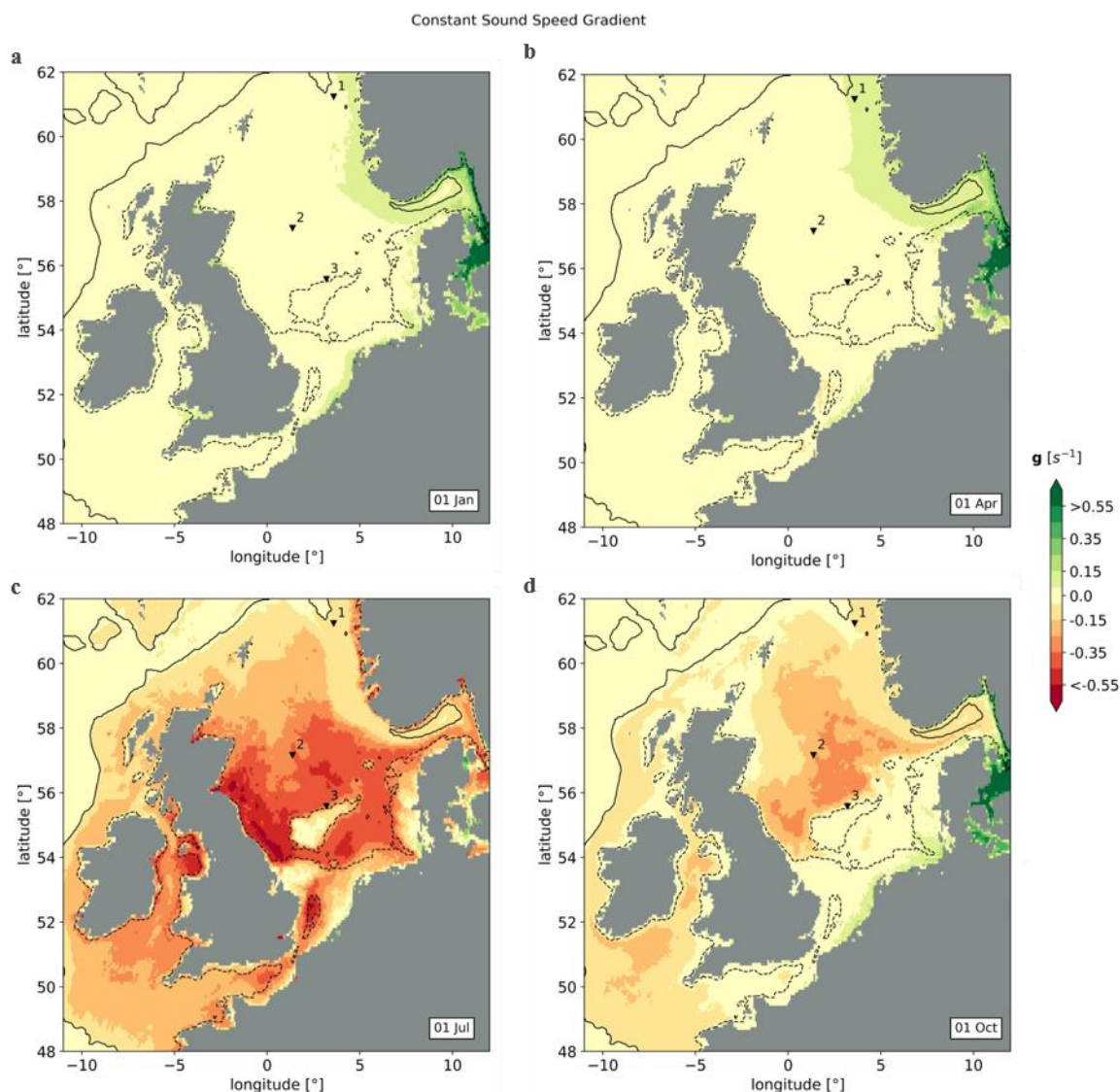

Figure 3.10 Color map of North Sea's 10-year-mean constant sound speed gradient g for **a)** January 1st; **b)** April 1st; **c)** July 1st; **d)** October 1st, period 2010-2020. Black dashed line is the $40m$ isobath; black solid line the $400m$ isobath. Bathymetric data and thermodynamic variables from GLORYS 12V1, provided by Copernicus Marine Service. Black markers indicate installation location – that are used in paragraph 3.3 – where SVPs were taken by Van Oord's SRI vessel Stornes in the year 2020.

- *When $g \cong 0$ then $c_s \cong c_H$ and we have almost no refraction of the ray (yellow color in Figure 3.10 & 3.11).*
  This is the well-mixed situation in terms of sound velocity, often occurring in shallow coastal areas away from the influence of freshwater. There, the sound velocity remains constant with depth i.e. the harmonic mean sound velocity hardly deviates from the surface sound velocity. Since the surface sound velocity is

mostly influenced by the air temperature, the sound velocity follows the seasonal cycle. However, during winter/spring (Figure 3.10a,b), almost the entire shelf sea has small sound velocity gradients due to reduced or absent heat input in combination with the effect of strong wind mixing. Offshore of the continental shelf, the constant sound velocity gradients are relatively stable throughout the year due to the very large depth. The effect of increased sound speeds in upper layers from buoyant heat input is averaged out from surface to bottom.

- When $g > 0$ then $c_s < c_H$ and we have net upward refraction of the ray (green color in Figure 3.10 & 3.11).
  This situation is related to salinity gradients due to freshwater discharge and is characteristic in the Kattegat, the Skagerrak, and along the Norwegian coast where fresh Baltic waters enter the North Sea. Only during summer, the buoyancy input from solar heating is dominant over the buoyancy input from freshwater, creating negative gradients. This mechanism also holds for ROFIs: if the input of buoyancy from freshwater is larger than the input from solar heating, positive gradients exist (autumn and winter period, Figure 3.10a,d). But in summer, the riverine discharges are small, and the effect of solar heating is strong, such that these shallow coastal areas have constant sound speeds from surface to bottom.
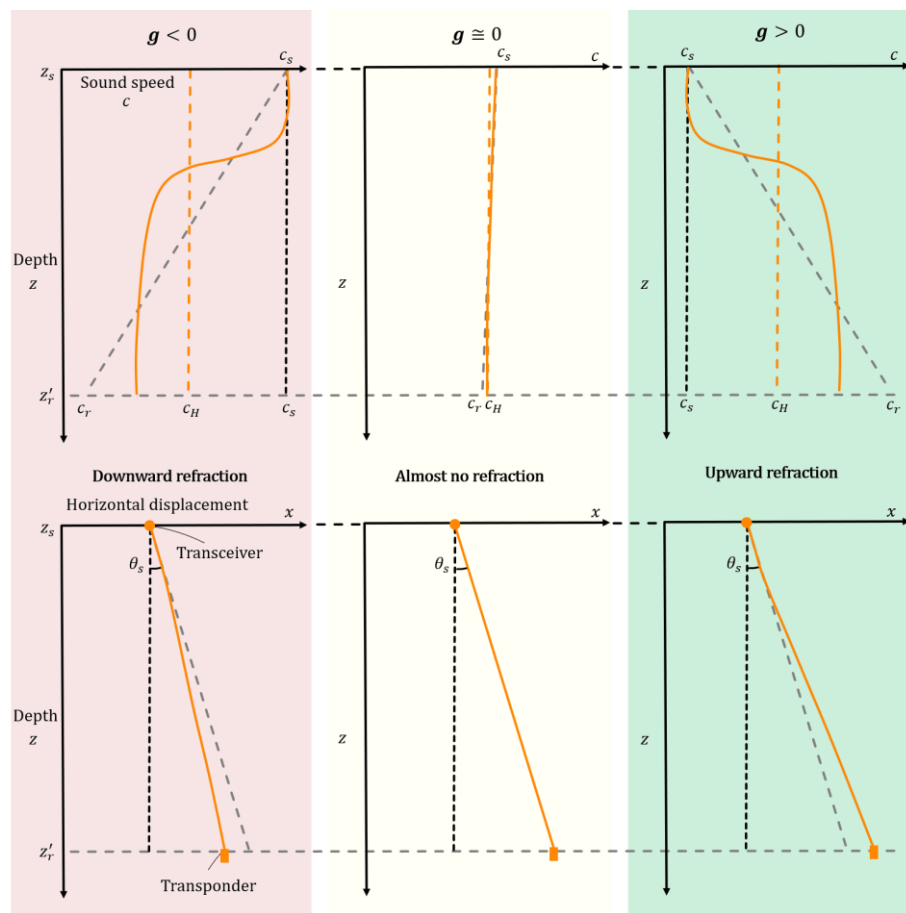
Figure 3.11 Upper: SVP (orange line) and their equivalent SVP (ESVP) (gray line) with the constant sound velocity gradient g (Eq. [3.2]). Lower: effect of constant sound velocity gradient on ray's refraction. Sound waves bend away from the layers with high sound velocity and bend towards the layers with low sound velocity i.e. sound is lazy. Transceiver is located under the hull of the vessel. Transponder is mounted on the FPROV.

In the next paragraph we will see how the value of the constant sound velocity gradients influences the value of the refraction-induced positioning error. In combination with the water depth, the constant sound velocity gradient determines where and when the contractor can apply the CSSV method and use the ISS sound velocity instead.

3.3 The CSSV Method

In the previous paragraph we assessed the stratification of the SVP by means of the constant sound velocity gradient g. During winter/spring, we saw that for most of the shelf sea the SVP shows less depth-variation. Then, the effect of refraction and its associated positioning error is small. However, during summer, strong gradients exist and one could expect the effect of refraction to be much larger.

It is interesting to examine what the refraction error is in case no SVP is taken. Instead, the value of the ISS sound velocity is assumed to be constant with depth. This simplification obviously leads to refraction errors. But in case the harmonic mean sound velocity does not deviate much from the surface sound velocity (i.e. $c_s \cong c_H$ and $g \cong 0$, Figure 3.11), it might not lead to significant refraction errors that are problematic for underwater acoustic positioning with FPROVs. Another case is that strong gradients exist, but the depth is insufficient for the refraction error to grow problematically in terms of positioning accuracy. This is because FPROVs have a limited angular range and thus operate under small incident angles. Whether it is valid to use the ISS sound velocity as constant depends on the stratification of the actual SVP and the depth at which the FPROV is located.

In order to assess the quality of the model-based SVPs, we compare the estimated refraction errors – based on 10-year-daily-mean temperature and salinity data, period 2010-2020 – with observations in the North Sea from Van Oord's SRI vessel Stornes in the year 2020. At those project locations, the SVP was measured simultaneously with the launch of the FPROV by means of a sound velocity sensor attached to the ROV's framework (Figure 3.2). In this paragraph, three project locations are dealt with in detail to give the reader feeling for the type and variability of the data. Geographical information is given in Table 3.3. At the end of the paragraph, an overview of the performance estimates for other project locations are given, constituting a total of 72 observations from 13 SRI projects.

Project	1	2	3
Geographical location	61.24°N; 3.59°E	57.16°N; 1.37°E	55.58°N; 3.20°E
Depth	$355m$	$90m$	$65m$

Table 3.3 Geographical information for three SRI project locations in the North Sea where SVPs were taken by Van Oord's SRI vessel Stornes in the year 2020.

3.3.1 Time-dependent SVPs

In paragraph 3.2 we presented colormaps of the geospatial dependency of temperature, salinity and sound velocity for one particular day. The temporal variability of these variables could not be captured in one single figure as only three dimensions can be mapped. Therefore, this section stacks the SVPs (vertical axis) in time (horizontal axis) where the color is the value of the variable. The time-dependent behavior of sound velocity is studied in more detail for project location 1. Figure 3.12 shows the timeseries of 10-year-daily-mean temperature, salinity and sound velocity.

The white lines indicate the difference in value between the surface z_s and bottom z_r'. The timeseries of temperature (3.12a) show strong seasonal dependence, where upper layers are slightly colder in winter and significantly warmer in summer compared to the bottom temperatures. The timeseries of salinity (3.12b) however show a less distinct pattern with spontaneous patches of freshwater originating from the Baltic. Their combined effect on the sound velocity (3.12c) is clearly dominated by the temperature seasonality.
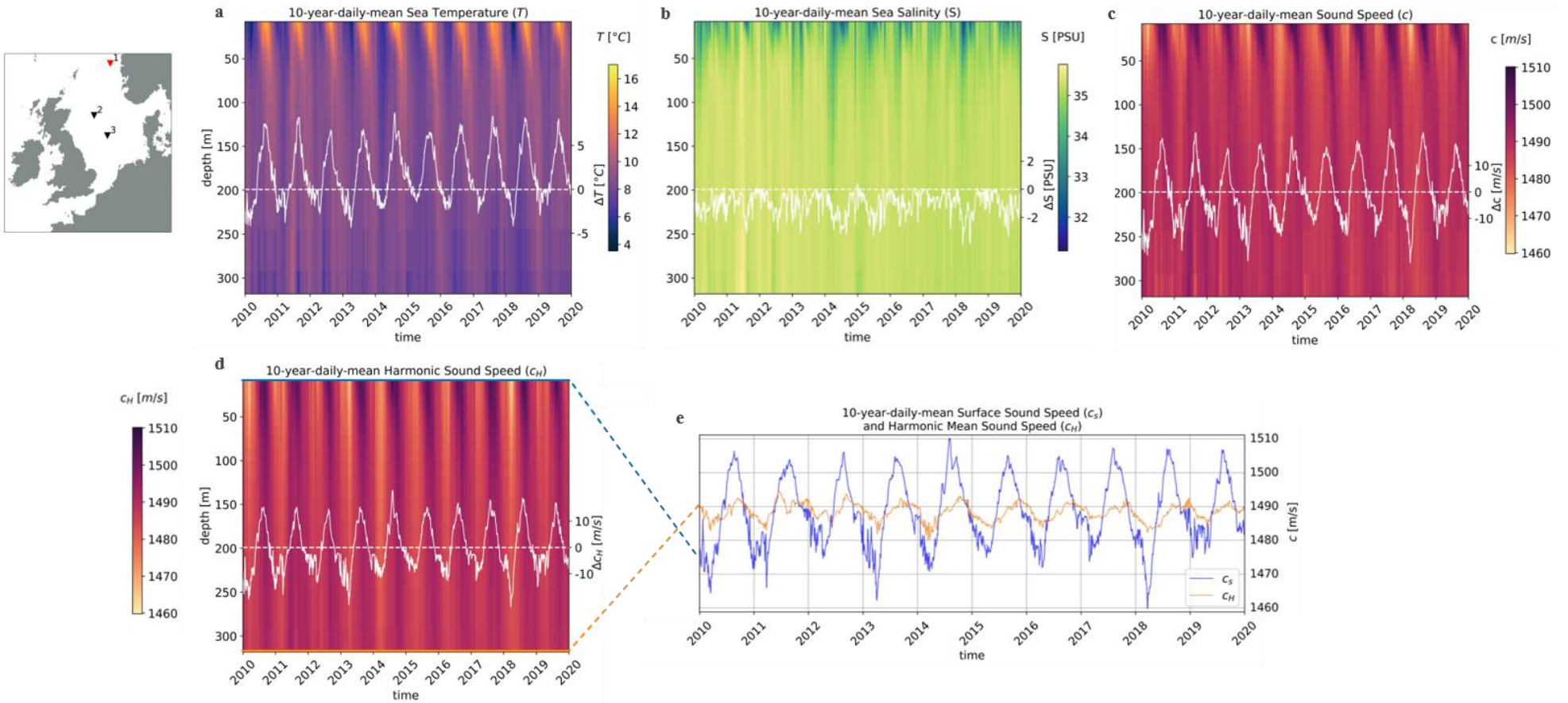
Figure 3.12 Color map timeseries of 10-year-daily-mean **a)** sea temperature; **b)** sea salinity **c)** sound speed; **d)** harmonic sound speed; **e)** surface sound speed (blue surface line in **d**) and harmonic mean sound speed at receiver depth (orange bottom line in **d**). Project location 1 (61.24°N; 3.59°E). Thermodynamic variables from GLORYS 12V1, provided by Copernicus Marine Service. Sound speed empirically calculated using Medwin's relation Eq.[3.1]. White lines indicate variable difference between surface and bottom.

However, compared to the temperature variations, the difference in sound velocity between surface and bottom is less in summer and more in winter. This is due to the effect of reduced salinity at surface level, and the influence of depth. Because of its geographical location along the Norwegian coast, project location 1 is characterized by significant sound velocity gradients in summer period that occur in the upper $70m$, while in winter period it is characterized by more mild sound velocity gradients

Using Eq. [2.2], the timeseries of the harmonic mean sound velocity are calculated and plotted in Figure 3.12d. Where the white line crosses zero, the surface sound velocity c_s equals the harmonic mean sound velocity c_H at the seafloor [5]. Figure 3.12e shows the timeseries of the surface sound velocity c_s (blue surface line in Figure 3.12d) and the harmonic mean sound velocity at receiver depth (orange bottom line in Figure 3.12d).

When the surface sound speed c_s and the harmonic mean sound speed c_H are equal, the consequence of considering the surface sound speed as being constant with depth is minimal in terms of refraction error. Where the difference is largest, the refraction error is largest if one neglects the vertical variation of the SVP.

3.3.2 From SVP to refraction-induced positioning error

Using the ESVP ray-tracing algorithm, derived in chapter 2, we can calculate what vertical and horizontal refraction-induced positioning errors are introduced when using the ISS sound velocity as constant instead of the actual SVP (Figure 3.13). Recall the basic formulas for the vertical displacement z_r' and horizontal displacement x_r at receiver depth, based on the ESVP using the constant sound velocity gradient $\boldsymbol{g}$:

$$z_r' = z_s + \frac{\sin(2\arctan(e^{tg}\tan(\theta_s/2))) - \sin\theta_s}{p\boldsymbol{g}}$$

<div align="right">3.3</div>

$$x_r = \frac{\cos\theta_s - \cos(2\arctan(e^{tg}\tan(\theta_s/2)))}{p\boldsymbol{g}}$$

<div align="right">3.4</div>

The other ingredients needed to calculate the displacements are:

- $t\ [s]$, the one-way travel time of the acoustic signal, recorded by the USBL transducer;
- $\boldsymbol{g}\ [s^{-1}]$, constant sound velocity gradient of the ESVP (Geng and Zielinski, 1999);
- $\theta_s\ [°]$, incident ray angle at USBL transducer head, surface level z_s;
- $p = \sin\theta_s/c_s$, Snell's constant, including $c_s\ [m/s]$, the surface sound velocity close to the USBL head.

Using Eq. [3.3] and Eq. [3.4], we can calculate the vertical and horizontal displacements for the case considering the actual SVP and the case considering the ISS sound velocity as being with depth i.e. the CSSV method. Both cases are schematized in Figure 3.13. Comparing the transponder coordinates (x_r, z_r'), results in a refraction-induced positioning error, respectively Δz in the vertical direction and Δx in the horizontal direction.

---

[5] The sound velocity at surface is in fact the harmonic mean sound velocity at surface level. Using Eq. [2.2] for the first layer:

$c_H = \sum_{i=1}^{1}|\Delta z_i|/\sum_{i=1}^{1}\frac{|\Delta z_i|}{c_i} = |\Delta z_s|/\frac{|\Delta z_s|}{c_s} = c_s$
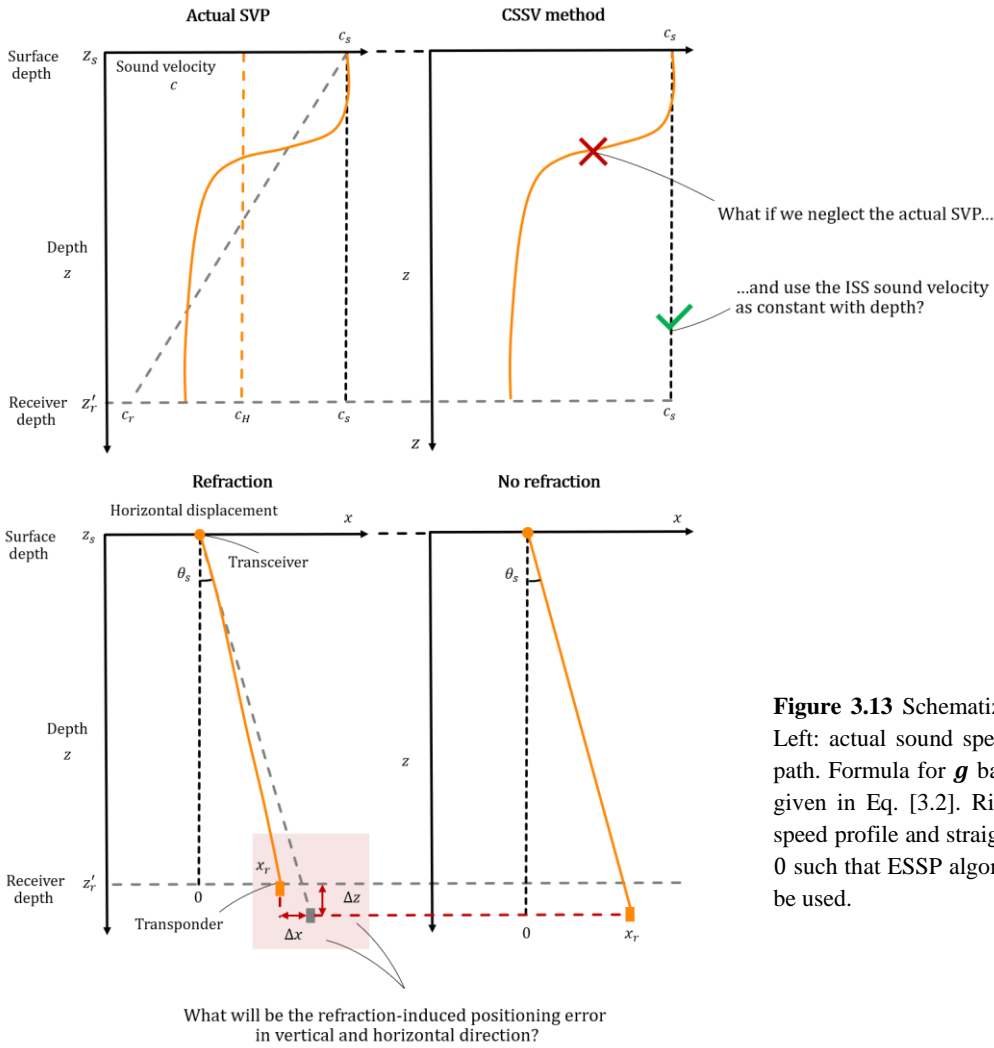
TUDelft

Van Oord
Marine ingenuity

Figure 3.13 Schematization of the CSSV method Left: actual sound speed profile and refracted ray path. Formula for $\boldsymbol{g}$ based on ESSP algorithm and given in Eq. [3.2]. Right: constant surface sound speed profile and straight ray path. $\boldsymbol{g}$ asymptotic to 0 such that ESSP algorithm (Eq. [3.3] & [3.4]) can be used.

In this thesis, the calculation of the refraction errors is based on the 10-year-daily-mean record of the empirically-derived SVPs from GLORYS 12V1. For each day of the year, the mean is calculated. The result is a representative one-year timeseries of the average surface sound velocity and the average harmonic mean sound velocity. This is in fact a timeseries of the sample mean. To give an indication of how uncertain the estimated mean is, we aim to derive the confidence intervals for the mean. Chosen is to use the Student's t-distribution for the derivation of the confidence intervals under the assumption that the sample comes from a normal distribution, which is a safe assumption according to Central Limit Theorem (Storch and Zwiers, 1984). The bounds are estimated with 99% confidence, which is more than three standard deviations (3σ) from the mean. More details on the motivation and derivation are provided in intermezzo 3.1.

Intermezzo 3.1 Confidence intervals of the mean

_____

The timeseries of the sample mean, based on $n = 10$ observations, is applied for each day of the year $\{x_1, \dots, x_n\}$ and reads:

$$\bar{x} = \frac{1}{n} \sum_{i=1}^{n} x_i \qquad \text{I.1}$$

To give an indication of how uncertain the estimated mean is, we aim to derive the confidence intervals for the mean. Without making a distributional assumption, we could proceed using bootstrap, which is a non-parametric method. Bootstrapping first randomly samples with replacement from the modelled sound speeds for the specific day of the year, and then evaluates the

statistic from the newly created sample. In this case the statistic is the sample mean. By repeating these steps a large number of times, an approximate confidence interval can be constructed (Storch and Zwiers, 1984). However, the problem with a small sample is the question whether it can correctly describe the population it comes from. When the variation in the sample is small – as is the case for the sound speed data derived from GLORYS 12V1 – the derived confidence intervals is relatively narrow banded around the sample mean. That might sound like a good thing, but there is no way to know whether the small sample is good enough except getting real observations. For this reason, we move to a parametric method and assume the sample comes from a normal distribution. This is a safe assumption according to Central Limit Theorem. Central Limit Theorem assures that the sample mean will have a distribution that converges towards a normal distribution as the sample size increases (Storch and Zwiers, 1984), provided that the random variables are independent and identically distributed. But, since the population's standard deviation is unknown and because the sample size is small, we should apply the Student's t-distribution, introduced by W.L. Gosset. The Student's t-distribution can specifically be used for estimating the mean of a normally distributed population. In fact it converges to the standard normal distribution when $n \geq 30$ (Storch and Zwiers, 1984):

The confidence interval (CI) using the t-statistic reads (Storch and Zwiers, 1984):

$$\left(\bar{x} - t\frac{S}{\sqrt{n}}, \bar{x} + t\frac{S}{\sqrt{n}}\right)$$

I.2

With the sample mean $\bar{x}$, the number of observations n, and S the square root of the sample variance for each day of the year:

$$S^2 = \frac{1}{n-1}\sum_{i=1}^{n}(x_i - \bar{x})^2$$

I.3

The t-value in Eq. [I.2] is the $0.5 + \tilde{p}/2$ quantile of the t-distribution with $n - 1$ degrees of freedom (df). We want to estimate the bounds with 99% confidence, that is $\tilde{p} = 0.99$. This yields $t = 3.250$ for df = 9, which comes down to more than three standard deviations (3σ) from the mean. The confidence interval derived with the Student's t-distribution provide a broader confidence interval because the sample is assumed to be taken from a population following the normal distribution. This provides more information compared to the one derived with bootstrapping, because it only uses the sample variables. The latter is therefore not presented in this study; only the confidence interval derived using the Student's t-distribution.

_____

The result for calculating the sample mean and its confidence interval for the 10-year-daily-mean record of the surface sound velocity c_s and the harmonic mean sound velocity c_H (Figure 3.12e) is given in Figure 3.15a. From Figure 3.15a the timeseries of the constant sound velocity gradient g easily follows using Eq. [3.2] (Figure 3.15b). Then, the horizontal displacement x from the transceiver can be calculated using Eq. [3.4] (Figure 3.15c), where the incident angle is fixed and considered to have a value of $\theta_s = 6°$ i.e. approximately the maximum angular range of the FPROV. This yields the maximum refraction-induced positioning error we can expect using the CSSV method. The same working procedure for translating thermodynamic variables into sound speed data – as was shown in Figure 3.12 – is applied to project locations 2 and 3. Their resulting annual mean timeseries are given in Figure 3.15.

Along with the modelled timeseries – representing a typical year at these project locations – the observed values are plotted. These are derived from sound velocity profile measurements on board of Stornes SRI vessel at the project locations in 2020. Figure 3.14 shows the measured and modelled SVPs at these locations.

For the specific day of the year, all three measured SVPs show a sharp sound speed gradient, where the increase in the upper 40 to $50m$ is due to solar heating during summer period. Consequently, a sharp thermocline has developed. The dip in sound velocity between 40 and $70m$ at project location 1 is because of reduced salinity in the upper layers due to a freshwater current stream originating from the Baltic Sea. However, the buoyant input from heat dominates in the upper $40m$, therewith significantly increasing the sound velocity.

As expected, the model-based SVPs are relatively smooth. Two plausible reasons for the smoothening are:

- The modelled profiles are averaged over a day, and then the mean of consecutive years is taken for the period 2010-2020, while the measured profiles are taken at a specific time of the day in a different year. Therefore, the measured profiles show day-specific details that are averaged out by the model, and thus can take a more complex shape with steep gradients;
- Despite averaging over a day, it could be that the GLORYS 12V1 system is not capable of modelling the steep gradients in terms of the underlying physics.

In addition, the modelled profile does not always cover the water column. Some reasons for the mismatch are:

- The bathymetry is not correctly represented in the Copernicus product: the depth increment increases with increasing depth, therewith the resolution decreases;
- Based on the coordinates of the measurement location, the grid cell closest to the project location is chosen, but that can be approximately 4.5 km off. Because of the spatial resolution, the model might lack providing the correct depth information.

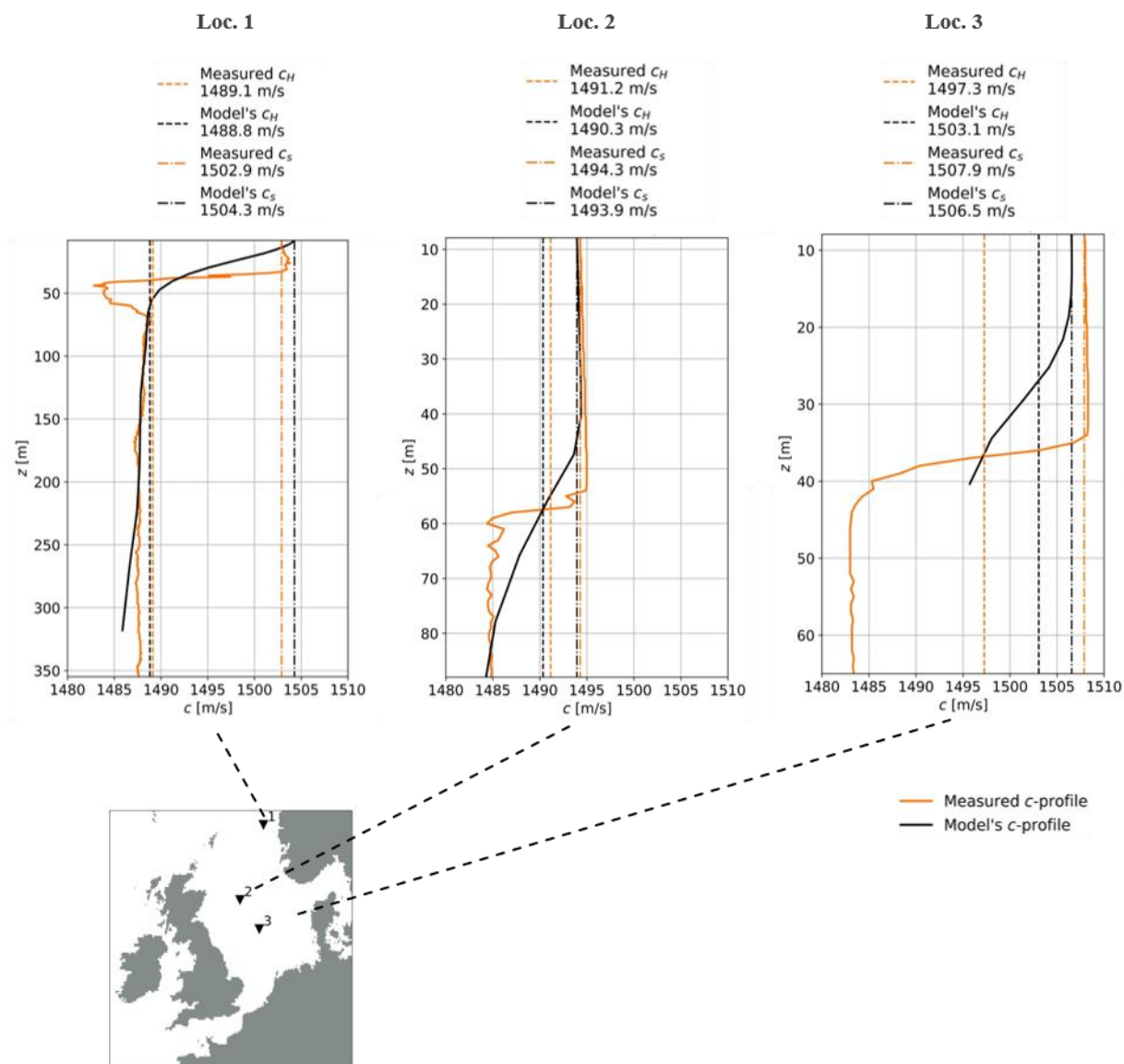**Figure 3.14** Model-based SVPs based on mean sound velocity data in the period 2010-2020 (black solid line) of GLORYS 12V1 vs. measured SVPs taken by Van Oord's Stornes SRI vessel in 2020 (orange solid line), for three project locations in the North Sea. Loc.1 (Sept 11th, 2020); loc. 2 (Oct 29th, 2020); loc.3 (Aug 8th, 2020). Harmonic mean sound speed c_H and surface sound speed c_s are presented with dashed lines.

Despite the imperfections, of interest is whether the model can provide accurate estimates of the surface sound velocity and the harmonic mean sound velocity as the acoustic pulse propagates with sound speeds that differ continuously: the pulse accelerates/decelerates, and refracts by the change in sound velocity. When the harmonic mean sound velocity is estimated correctly, we know what the average velocity is of the acoustic pulse on its way down, and thus the distance travelled. In combination with a correct estimate of the surface sound velocity, the refraction can be applied. Looking at Figure 3.14, we see that the estimates of the surface sound velocity correspond well with the observed value for that specific day of the year i.e. less than $1.5\,m/s$ difference. In addition, the modelled values of the harmonic mean sound velocity agree with the observations for project location 1 and 2, but <u>not</u> for project location 3. The mismatch of project location 3 is because the modelled harmonic mean sound velocity is based on the short profile in the upper $40m$. Consequently, the harmonic mean is much higher compared to the one derived from the observed profile, which has a significant contribution of lower sound speeds in deeper layers (last $25m$). An insufficient depth profile does not always lead to bad estimates. For example project location 1, the profile also has insufficient depth (misses $35m$). However, the harmonic mean sound velocity does not change much in these lower layers, and because of its great depth, a shortening has minor influence on the value.

The SVP measurements at the three project locations are compared with the estimated timeseries of GLORYS 12V1 for the case of applying the CSSV method. Their derived values are plotted in Figure 3.15. For each location and parameter, a brief overview is given:

- *Timeseries of annual mean surface sound velocity c_s and harmonic mean sound velocity c_H (Figure 3.15a)*
  All three locations show a strong seasonal dependence in surface sound velocity due to solar heating in upper layers. The minimum occurs in spring and the maximum in summer period. The surface sound velocity for project location 1 shows quite some peaky variation in winter/spring, most likely due to discharge volumes of Baltic freshwaters in upper layers that differ in intensity and timing each year. For those months, the confidence interval of the mean is relatively broad. With increasing depth, the timeseries of the harmonic mean sound velocity are becoming more stable throughout the year: the seasonal changes in upper layers are averaged out for greater depths. Therefore, an estimate of the harmonic mean sound velocity can be provided easily (as will be clear in paragraph 3.4). For shallower depths, the harmonic mean sound velocity is more variable and starts to follow the annual cycle of the surface sound velocity more and more, in agreement with the heat gain from air in shallower waters (see section 3.2.2). The measured values (squares) fall within the derived confidence interval of the mean over the 10-year period, except the harmonic mean for project location 3 (which is due to insufficient depth representation of the GLORYS 12V1 product).

- *Timeseries of annual mean constant sound velocity gradient g (Figure 3.15b)*
  In agreement with the findings in section 3.2.3 we observe the following: when $c_s < c_H$ then $g > 0$ (green zone); when $c_s > c_H$ then $g < 0$ (red zone); where the lines cross, $c_s = c_H$ then $g = 0$. For project locations 2 and 3, the harmonic mean sound velocity is almost equal to surface sound velocity in winter/spring. For those periods, the constant sound velocity gradient is close to zero, referring to the well-mixed situation in terms of sound velocity. Then, the effect of refraction is nihil. In contrast, in summer period the gradient is large, and thus the ray will be refracted significantly. How large the refraction error will be depends on the depth propagation of the acoustic signal. For project location 1, refraction occurs almost the entire year. Because of the large depth, the seasonal variation in upper layers does not penetrate into deeper layers. Therefore, the harmonic mean sound velocity cannot follow the changes of sound velocity in upper layers. Consequently, a gradient exist almost the entire year. Although the gradient is small, the depth at this location is large and thus the error can grow significantly when propagating towards the ROV at depth.
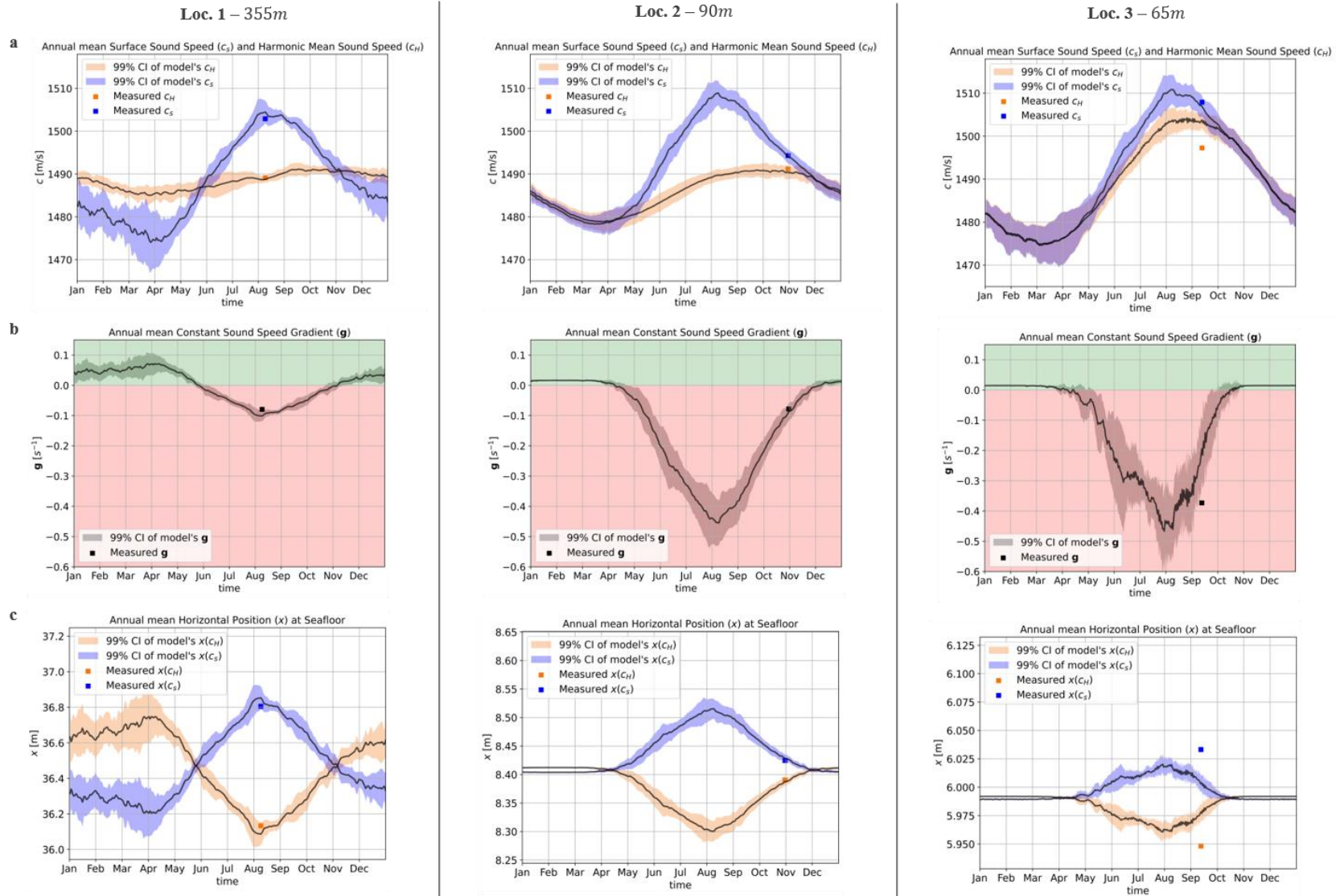
Figure 3.15 Modelled timeseries of annual mean (black solid lines) **a)** surface sound speed c_s and harmonic mean sound speed c_H; **b)** constant sound speed gradient g; **c)** horizontal position at seafloor for an incident angle of $\theta_s = 6°$ using Eq. [3.5], for three project locations in the North Sea. Confidence interval (CI) is constructed using the t-statistic Eq. [I.2]. Measured values are presented with squares for the specific day of the year. Depth at Loc. 1 $355m$, Loc 2. $90m$ and Loc. 3 $65m$

- *Timeseries of annual mean horizontal displacement x (Figure 3.15c)*
  Using Eq. [3.5], with a fixed incident angle of $\theta_s = 6°$, the horizontal position can be calculated. It is the displacement (or offset) from the transceiver head, and increases with increasing depth. Overall we see the following for the three project locations: where the harmonic mean sound speed is close to the surface sound velocity (3.15a), the gradient is close to zero (well-mixed situation)(3.15b), the displacement is approximately equal. For these cases, the use of the CSSV method is valid because the actual SVP does not result in significant refraction.

The absolute difference between the displacements is the refraction-induced horizontal positioning error $|\Delta x|$. Whether the positioning error is acceptable depends on what client requirements are set in terms of accuracy. The threshold is ambiguous as it depends on the client's requirements, the project type and the design. Also the water depth is of importance because the accuracy of underwater acoustic positioning decreases with increasing water depth. Therefore, it makes sense the client and contractor agree on a lower accuracy for a SRI project at $800m$ depth compared to one at $100m$ depth. There is no general design manual that fits the accuracy requirements for all type of offshore projects.

In order to assess where and when the CSSV method has potential, we come up with a simple and general threshold function $\delta_{|\Delta x|}$ in $[m]$ for the maximum allowable refraction error $|\Delta x|$ (Figure 3.16a):

$$\delta_{|\Delta x|} = \begin{cases} 0.2 & \text{for} & z \le 400m \\ z/2000 & \text{for} & 400m < z \le 1000m \end{cases}$$ 3.5
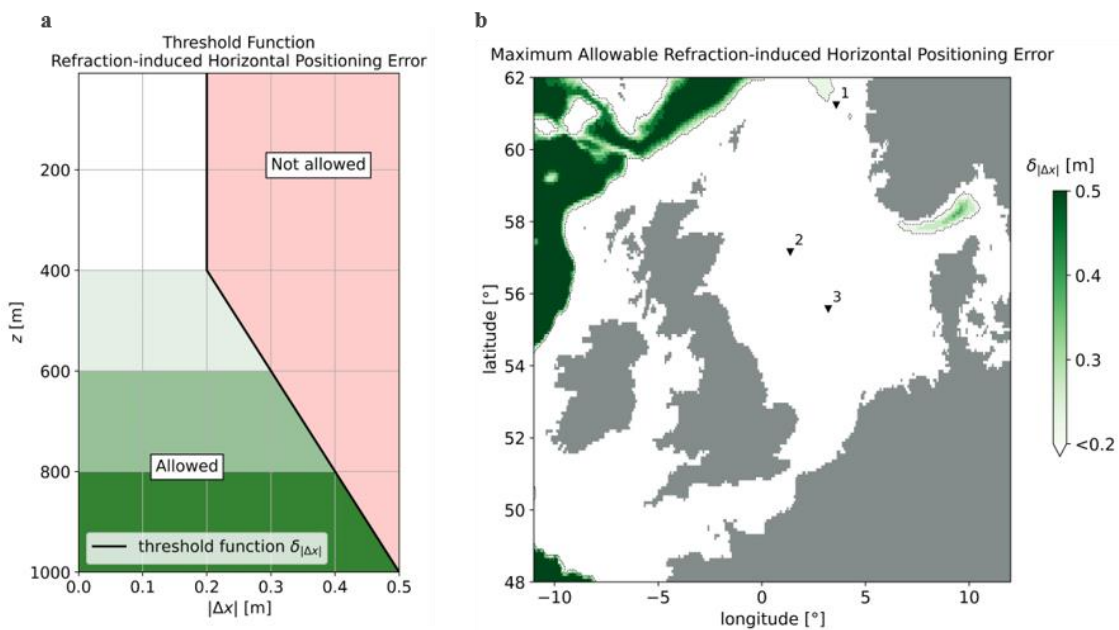

Figure 3.16 a) Threshold function Eq. [3.5] for the maximum allowable refraction-induced horizontal positioning error with depth. Minimum allowable error is $0.20m$ towards $400m$. From there it increases towards $0.5m$ at $1000m$ water depth. **b)** Maximum allowable horizontal positioning error mapped for the North Sea.

Where the maximum allowable horizontal positioning error at $1000m$ depth is $50cm$ and decreases with decreasing depth towards the minimum of $20cm$. Since the three case locations all have a depth less than $400m$ (Figure 3.14), the threshold is $\delta_{|\Delta x|} = 20cm$. The maximum allowable refraction-induced horizontal positioning error is also mapped for the entire North Sea, based on the threshold function Eq. [3.5], and is given in Figure 3.16b. Only in the Skagerrak and along the continental slope the depth is larger than $400m$ and thus $\delta_{|\Delta x|}$ is depth-dependent.

Figure 3.18a shows the refraction-induced horizontal positioning errors $|\Delta x|$ for the three project locations, obtained by taking the absolute difference between the horizontal displacements in Figure 3.15c. The measurements (red squares) are in good agreement with the estimated error, except for location 3 due to inaccurate depth information.

Most interesting are the green time windows, which highlight what time of the year the error is below the threshold $\delta_{|\Delta x|}$. These are the time periods when it is valid to neglect the actual SVP and instead use the CSSV method. For project location 1, the refraction error is significant and above the threshold most of the time. At that location, one cannot get away with considering the ISS sound velocity as constant most of the time. At project location 2, the summer stratification causes sound velocity gradients to grow and therewith the refraction error, passing the allowable threshold in that period, while the rest of the year it is valid to use the ISS sound velocity. At project location 3, one can always neglect the complexity of the SVP and rely on the ISS sound velocity. Despite the fact that the water column is characterized by strong sound velocity gradients, the depth is insufficient for the error to grow large enough to pass the threshold.

Applying the above described approach to the entire North Sea, we estimate the refraction-induced positioning error when using the CSSV method. Figure 3.18a shows the maximum and minimum horizontal positioning error, where both maximum and minimum are based on the upper bound of the 99% confidence interval of the mean. The colormap of the maximum error tells us that for a very large area of the North Sea the $0.20m$ threshold is never passed throughout the year (white colour). The colormap of the minimum error tells us that almost the entire North Sea experiences time windows where one could neglect the sound speed profile. Only at the continental slope and in the Skagerrak, the refraction-induced horizontal positioning error passes the $0.20m$ all year. Comparing with the bathymetric map in Figure 3.6a, we notice that the magnitude of the error is largely governed by the water depth. Despite the fact of the large sound velocity gradients in summer in the North Sea (Figure 3.10c), the shallow depths limit the error to grow. As the combination of sound velocity gradients and depth determines the magnitude of the refraction error, one can define sea areas where CSSV method has potential applicability by using the datasets of Copernicus Marine Service. This will be done in the next section.

Alternative to mapping absolute values, the errors can be scaled to the water depth (WD). Figure 3.17 shows the maximum annual horizontal refraction error as percentage of the water depth. It indicates that the degree of refraction is almost uniform for the North Sea, from approximately $35m$ depth contour (black line in Figure 3.17), where the purple colour starts. According to Huthnance (1991), this isobath is approximately the bound where seasonal thermal stratification occurs in the North Sea. Exceptions occur along the Norwegian coast and the Faroe-Shetland Channel, where refraction errors are amplified by sound velocity gradients as result of currents, originating from the Baltic Sea and the Atlantic, respectively.

Figure 3.17 Colourmap of maximum annual horizontal refraction-induced positioning error at the seafloor for an incident angle of $\theta_s = 6°$ when using the CSSV method. The errors are scaled by the water depth (WD) and given in percentages. Black line is the $35m$ isobath. Also the three project locations are given.

Similarly, the refraction-induced vertical positioning error $|\Delta z|$ is calculated and the maximum and minimum values are plotted in Figure 3.18b, along with the timeseries of the vertical error at the three project locations, all by using Eq. [3.3]. The vertical refraction error is a scaled version of the horizontal refraction error (factor ~4.5-5 larger). The scaling factor mostly depends on the incident angle θ_s: with increasing incident angle, the horizontal (vertical) refraction error increases (decreases), and therewith the ratio changes. For the application of FPROVs the incident angles are small and thus the acoustic pulse is sent almost perpendicular into the water
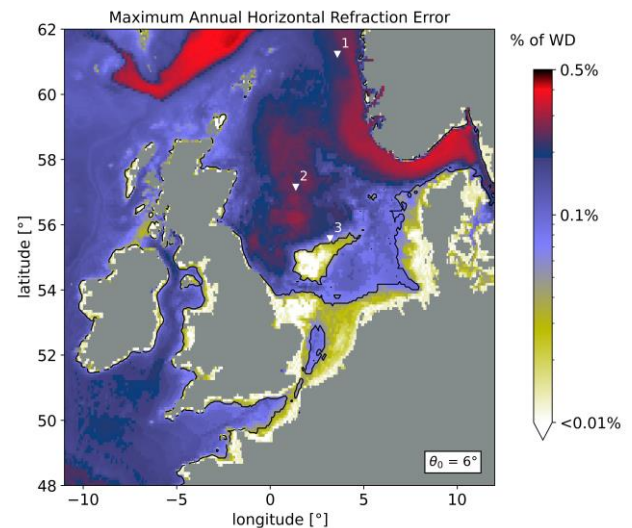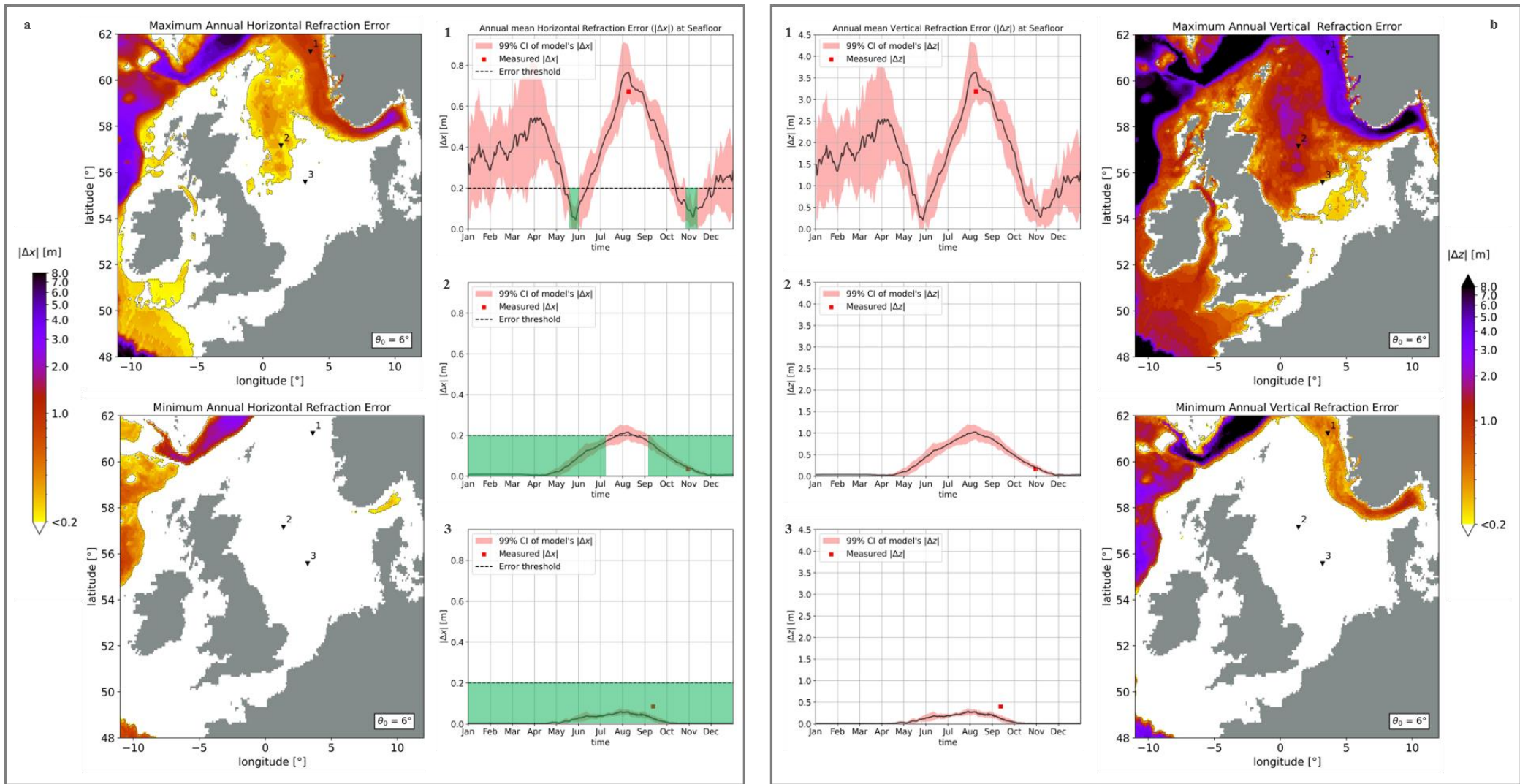
Figure 3.18 Colormaps of minimum/maximum annual horizontal (left) and vertical (right) refraction-induced positioning error at the seafloor for an incident angle $\theta_s = 6°$ when using the CSSV method. Timeseries (black solid lines) show the annual mean horizontal (left) and vertical (right) refraction error for the three project locations along with the measured error (red square) at the specific day of the year. Confidence interval (CI) is constructed using the t-statistic Eq. [I.2]. Green areas highlight the time window when the upper bound of the confidence interval (CI) for the horizontal refraction error is below the threshold of $\delta_{|\Delta x|} = 0.20m$.

column. In combination with the high value of the sound speed, a wrongly estimated harmonic mean sound speed quickly results in significant vertical errors. Although the vertical positioning errors are much larger than the horizontal positioning errors, in practice the estimate of the vertical position is combined in a Kalman Filter technique with depth information obtained from pressure sensors (Wang *et al.*, 2018). The depth level is obtained on the difference in hydrostatic pressure: one sensor mounted on the framework of the FPROV measures the water pressure, and one sensor on the vessel measures the atmospheric pressure. In addition, the FPROV has multiple MBESs with which the relative position to the seafloor is estimated. Because the depth estimate is a combined estimate of information coming from various sensors, the contractor does not have to rely only on depth information from the USBL system. For these reasons, the study assesses the applicability of the CSSV method based on the horizontal positioning error. The vertical positioning error is presented for completeness.

3.3.3 Applicability of the CSSV method

The colormaps of the maximum and minimum horizontal positioning error (Figure 3.18a) indicate that sea areas exist where one can rely on the ISS sound velocity only. Potentially, it determines where and when the contractor needs to stop for an SVP or can continue using the CSSV method. For that interest, the maximum annual horizontal refraction error in Figure 3.18a is analyzed per season and presented in Figure 3.19a.

What stands out are the winter and spring season when most of the North Sea does not experience horizontal refraction errors. For those periods, the water column is well-mixed in terms of the sound velocity due to the influence of wind-mixing and the reduced heat input from atmospheric warming in the Northern Hemisphere. Only the Skagerrak, the Norwegian Trench, and deeper parts along the continental slope experience horizontal refraction errors all year. For those sea areas, the persisting difference between the surface sound velocity and the harmonic mean sound velocity in combination with the deep waters lead to significant horizontal refraction errors ($\delta_{|\Delta x|} > 0.20m$) being present all year. The significant errors appearing in summer season between Britain and Norway largely follow the shape of the bathymetry of the Fladen Ground (see Figure 3.3, approximately the $80m$ isobath near location 2). As already mentioned in section 3.2.3, the errors are associated with thermal stratification. Even though the shallower areas receive approximately the same buoyancy input from heat, the water depth limits the refraction error to grow larger than $0.20m$. In fact, up to $40m$ depth (see Figure 3.6a), the refraction-induced horizontal error is $\delta_{|\Delta x|} \lessapprox 0.05m$ all year. Lastly, in autumn the errors in the Fladen Ground slowly disappear when thermoclines start to flatten.

Alternative to the seasonal analysis, one can sum the days when the threshold is passed e.g. $|\Delta x| > \delta_{|\Delta x|}$. The result is given in Figure 3.19b expressed as the horizontal refraction-induced positioning error being larger than the depth-dependent threshold (Figure 3.19b). In agreement with the time windows in Figure 3.18a, we estimate 80-90% time of the year the error is larger than the threshold at project location 1, 10-20% at project location 2, and 0% at project location 3, respectively. In general, the refraction errors in the Fladen Ground persist at most 40% time of the year, which is about 4-5 months, from June until the October. In that period, the contractor should use the SVP because the surface sound speed differs significantly from the harmonic mean. For the rest of the year, and for the white sea areas it holds that the CSSV method is valid to use for the application of FPROVs acoustic positioning.
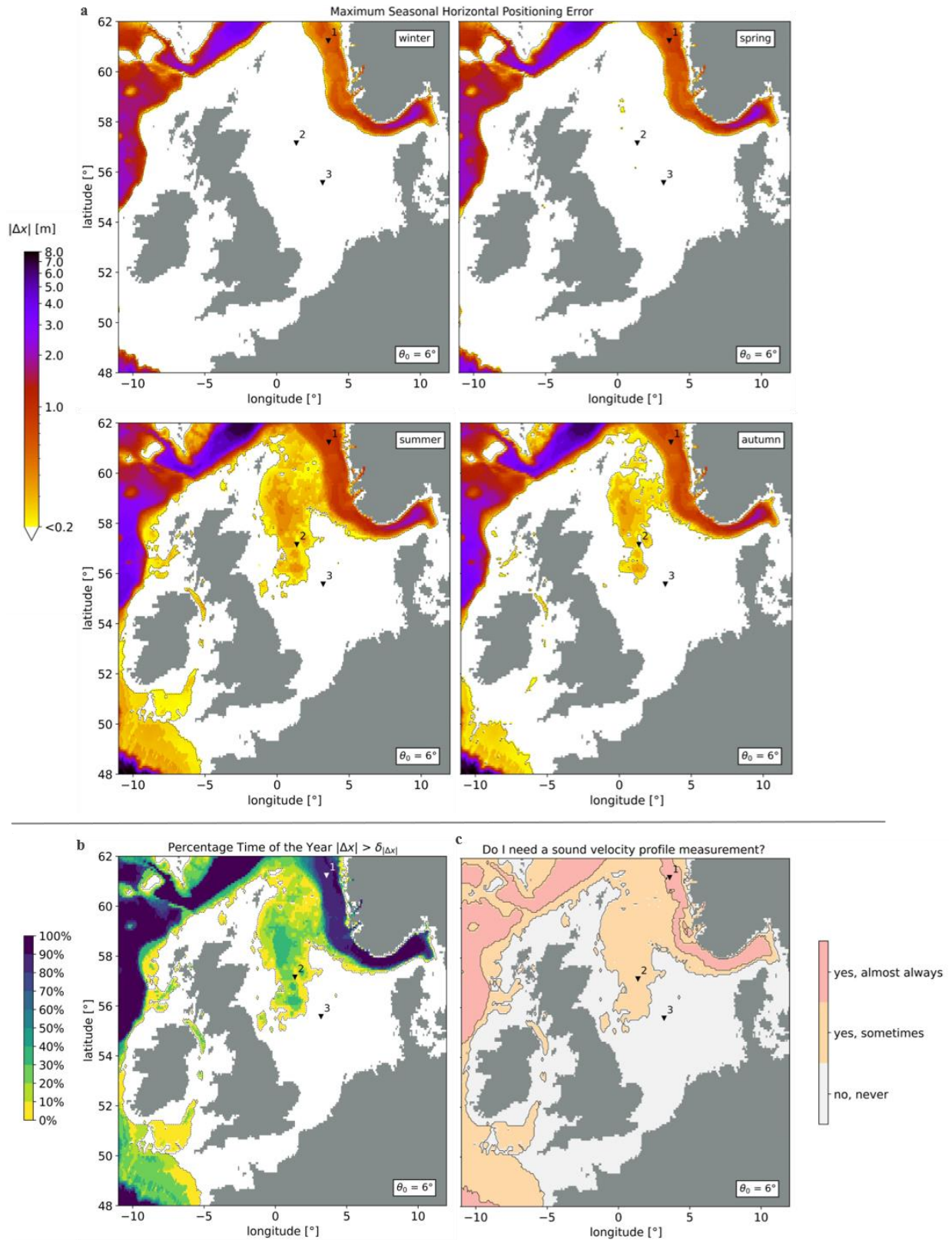
Figure 3.19 a) Colormaps of seasonal maximum refraction-induced horizontal positioning error at the seafloor for an incident angle $\theta_s = 6°$ in winter/spring/summer/autumn period when using the CSSV method; **b)** Colormap op percentage time of the year the refraction-induced horizontal positioning error passes the threshold of $\delta_{|\Delta x|}$; **c)** Colormap indicating the sea areas where SVP measurements are necessary i.e. where the surface sound velocity differs from the actual SVP such that positioning errors are unavoidable when using the CSSV method. Areas are defined as time of the year $|\Delta x| > \delta_{|\Delta x|}$: *almost always* > 85%, *sometimes* ≤ 85%, *never* 0%.

Based on the percentage time of the year the horizontal refraction-induced positioning error passing the threshold, one can create roughly three zones based on the following question: *"Do I need a sound velocity profile measurement?"*. These zones are mapped in Figure 3.19c and are defined as the percentage time of the year the threshold is passed:

- *"yes, almost always", more than* 85% *time of the year (red zone in Figure 3.19c);*
  These are the sea areas where large sound velocity gradients persist all year and/or areas where the depth is large such that refraction errors are significant all time of the year (i.e. 100% time of the year). The red zone also includes locations where one possibly can neglect the actual SVP (for instance at project location 1). Though, it is advised to take a SVP measurement because of the model's uncertainty. Since day-time variability of the profile (e.g. internal wave motion) is averaged out or not resolved in GLORYS 12V1, more complicated gradients can develop in reality. In combination with the large depth, refraction errors could be introduced that are beyond the model's expectations.

- *"yes, sometimes", less than* 85% *time of the year (orange zone in Figure 3.19c);*
  These are the locations where the threshold is passed less than 85% of the year, mostly in summer and autumn period as result of atmospheric heating. Thus, for a maximum offset of one-tenth of the water depth for FPROVs (e.g. $\theta_s \approx 6°$), from a depth of approximately $80m$, the contractor should take an SVP measurement in this orange zone, except for the winter/spring period. Project location 2 is one of those locations.

- *"no, never",* 0% *time of the year (white zone in Figure 3.19c).*
  Under similar constraints and for the application of FPROVs, the error is allowed all year (if set to be maximum of $0.20m$) in these areas. It comes down to approximately a depth less than $80m$, among which project location 3. In this zone, the contractor has certainty the vessel does not have to stop for additional SVP measurements. Instead of updating the USBL system with a new SVP, they are assured to continue with simplified constant profiles with its value based on the ISS sound velocity.

So, in this section the refraction error analysis is performed using data from a reanalysis model GLORYS 12V1 to determine roughly the sea areas where refraction errors are occurring. This quantifies the challenges in underwater acoustic positioning due to spatiotemporal variations of the sound velocity. For planning purposes, the offshore contractor can execute the refraction error analysis – using the ray-tracing algorithm Eq. [3.4] – on forecast systems. These product are also freely available and provided by Copernicus Marine Service, for instance the Mercator product, that provides forecasts 10 days in advance (Copernicus Marine Service, 2022). Of course, any other model could be used for planning.

3.3.4 Validation of the CSSV method

In the previous sections, only three observations were analysed and compared with model estimates. In order to assess whether the model provides reliable estimates of SVPs – and the associated refraction errors – all observations taken by Van Oord's Stornes SRI vessel were checked for this sea area. In total, the set includes 72 SVP measurements from 13 SRI projects executed in North Sea between June and November in the year 2020. Following the exact same working procedure, the horizontal ray-tracing algorithm Eq. [3.4] is used to calculate the horizontal refraction-induced positioning error for all observed SVPs when applying the CSSV method. The results are plotted in a colormap (Figure 3.20a) with the constant sound velocity gradient g on the horizontal axis, and the water depth z on the vertical axis up to $1000m$. The combination of these two parameters mostly influences the value of the refraction error. The colour represents a general modelled horizontal refraction error field for an incident angle of $\theta_s = 6°$, a surface sound velocity of $c_s = 1500 \ m/s$ and the harmonic mean sound

velocity with a value between $1450 \leq c_H \leq 1550\ m/s$. In general, the constant sound velocity gradient decreases with depth as the difference between the surface sound velocity and the harmonic mean sound velocity is scaled to the water depth (Eq. [3.2]). The refraction error grows with increasing stratification (value of $\boldsymbol{g}$) and depth.

Checking the observations in Figure 3.20a, almost all observations have a negative gradient, most likely induced by thermal stratification as all measurements are taken between June and November. The green coloured dots are the observations with a refraction error less than $0.20m$, and based on their depth and sound velocity gradient, those should be located in the white area of the modelled error field ($|\Delta x| < 0.20m$). As can be seen, the CSSV method still yields satisfactory results for the observations between $320\text{-}370m$ water depth (green dots). Despite their large depths, the constant sound velocity gradient is close to zero, and the consequence of considering the ISS sound velocity as constant with depth is small. Though, for the same water depths, the refraction error can be up to $1.0m$ if the constant sound velocity gradient deviates from zero e.g. when thermoclines further deepen in summer season.

Figure 3.20 a) Modelled refraction-induced horizontal error field for the application of the CSSV method, with the constant sound velocity gradient $\boldsymbol{g}$ on the horizontal axis and the depth z on the vertical axis. The incident angle is fixed with a value of $\theta_s = 6°$. The dots represent the calculated errors when applying the method to observed SVPs measured on board of Van Oord's SRI vessel Stornes in the year 2020 in the North Sea. **b)** Calculated errors and their measurement location in the North Sea. Figure 3.19c as underlay i.e. the model-defined zones where it is advised to take SVP measurements. **c)** Horizontal refraction error calculated using parameters from the measurement versus the modelled error using parameters from GLORYS 12V1. The diagonal means a perfect fit between measured and modelled mean error. As all measurements have depths smaller than $400m$, the error threshold $\delta_{|\Delta x|} = 0.20m$ (black dashed line). The greatest outliers are encircled.
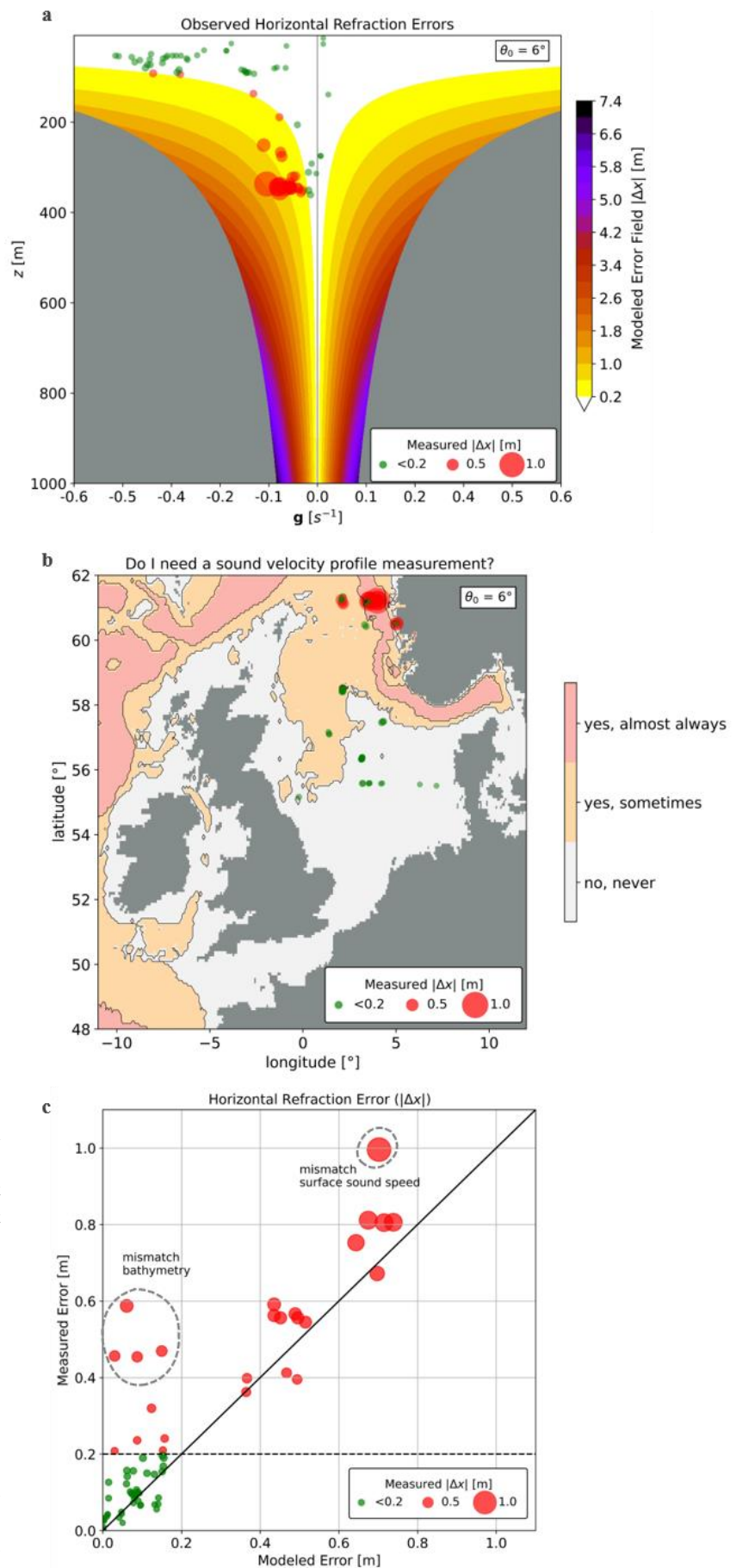
Figure 3.20b shows the geographical location of all observations. The model-defined white zone where no SVP measurements are necessary only includes observations with refraction errors less than $0.20m$. The orange zone – where SVP measurements should be taken depending on the season – include both errors that are less than $0.20m$ (green dots) and errors in the range of 0.20-$0.40m$ (red dots). The largest errors observed are located in red zone, where it is advised to take a SVP measurement almost all year, because of the relatively large sound velocity gradients in combination with depth. An exception to the classification are measurements taken close to the Norwegian coast at Bergen. There, significant refraction errors ($> 0.40m$) are measured, while the model defines the area as the white zone. The location is close to the steep bathymetry of the Norwegian Trench and the observed depth is $200m$ deeper than the bathymetric depth according to GLORYS 12V1.

The model's ability to estimate the expected horizontal refraction error is shown in Figure 3.20c, where the calculated refraction errors from the measurements are compared with the model-based estimated errors. The black diagonal line represents the perfect fit between the measured and the modelled mean error. In general, the model slightly underestimates the refraction error when compared to the model mean, but most errors fall within three standard deviations (3σ) from the estimated mean (i.e. the upper bound of the 99% confidence interval). Though, two groups of measurements stand out and are encircled in Figure 3.20c. The group of measurements with the bathymetric mismatch are the one located along the Norwegian coast at Bergen. The model predicts horizontal refraction errors being less than $0.20m$ all year (i.e. white zone in Figure 3.20b), while the measured errors are between 0.4-$0.6m$.

As already mentioned, the inaccurate depth representation of the model is the root cause of the invalid assessment of the method's applicability in this area. The other mismatch is because of the significant difference (of $+7\,m/s$) between the measured and modelled surface sound velocity. Another amplifying factor is the difference in harmonic mean that does not have a similar shift but is opposite in sign ($-2\,m/s$). Consequently, the wrong refraction is applied and the positioning error is much larger than expected. These groups of outliers are extremes of the model's inability to predict the correct refraction error as the model-based SVPs do not correspond with observations. In general – and thus also for other measurements – the deviation from the mean (black diagonal line) is determined by a combination of two factors:

- *Mismatch in bathymetry*
  An inaccurate depth representation leads to incorrect estimation of the refraction error when the constant sound velocity gradient deviates from zero. When sound velocity gradients develop as result of buoyancy input from heat and/or freshwater, the harmonic mean sound velocity changes. As seen in Figure 3.15a, for shallow water depths the harmonic mean will follow the surface sound velocity. For deeper water depths, the harmonic mean is less influenced by changes in upper layers. Therefore, inaccurate depth representation leads to wrong estimates of the difference between the harmonic mean and the surface value. In the worst case (e.g. at Bergen), the real error is 5 times greater than estimated by the model. Either the model's bathymetry should be better represented or the contractor should be more careful applying the method to locations close to a steep bathymetry.

- *Mismatch in constant sound velocity gradient (either due to surface sound velocity or harmonic mean sound velocity)*
  When the real constant sound velocity gradient does not correspond with the model's estimate, the wrong refraction is applied. This is due to incorrect estimates of the surface sound velocity or the harmonic mean sound velocity. In combination with depth, errors can grow significantly. However, if the difference in estimated and measured values for these two parameters are of similar magnitude and sign (e.g. both modelled c_s and c_H differ with $+2\,m/s$ from observation), the constant sound velocity gradient is the same, and the estimated refraction error is of similar order.

It is thus a combination of correct depth representation <u>and</u> a proper estimate of how sound varies with depth and in time.

All in all, one can state that for many project locations no SVP measurement was necessary at time of operation if a ISS sound velocity was used. In general, these are the locations with a water depth less than $80m$, but observations prove the that the CSSV method is also applicable to a depth of approximately $370m$ depending on the time of the year. It means that no additional stops were required to update the USBL system, therewith saving costly operation time.

3.4 The MSVP Method

For SRI at deeper depths, Figure 3.20a highlights that the applicability of the CSSV method decreases as the refraction error amplifies with increasing depth and stronger sound speed gradients. However, for deeper depths the constant sound velocity gradient shows less annual variation, because seasonal changes in upper layers are averaged out for greater depths. Its value is more stable throughout the year (see for instance Figure 3.10). Therefore, an estimate of the harmonic mean sound velocity can be provided easily using Copernicus products.

To this end, the contractor can either choose to rely on model-based estimated profiles (MSVPs) completely or combine them with the ISS sound velocity. In short we have two variants:

- complete MSVP method: uses both the estimate of the harmonic mean sound velocity and the surface sound velocity from the MSVP;
- combined MSVP method: combines the estimate of the harmonic mean sound velocity from the MSVP with the ISS sound velocity.

The performance of these variants are assessed using the 72 observations. Figure 3.21 shows the resulting refraction-induced horizontal positioning error. For the CSSV method (3.21a), one can see the general decrease in applicability with increasing depth. The mean horizontal refraction error of all observations is $|\widehat{\Delta x}| = 0.235m$.

In contrast, for the complete MSVP method (3.21b,c) almost all refraction errors are within the allowable range! The combined MSVP method performs slightly better on average with a mean horizontal refraction error of $|\widehat{\Delta x}| = 0.041m$ compared to $|\widehat{\Delta x}| = 0.050m$ for the complete MSVP method. One can reason that the daytime-specific response of surface layers on the air temperature can differ from the 10-year-daily-mean. Therefore, using the ISS sound velocity, a better estimate of the refraction can be given being closer to the observed refraction of the ray's path.

While the extensive analysis of the CSSV method revealed where and when in the North Sea the contractor should take a SVP measurement, the MSVP method can potentially assist in estimating the SVPs at the project location if necessary. According to Figure 3.21, the small refraction errors indicate that the Copernicus product provides estimates of the SVPs that are accurate enough for underwater acoustic positioning of FPROVs (e.g. with small incident angles). Benefiting from the general fact that the harmonic mean sound velocity becomes more stable for large water depths, the MSVP method is promising for the application in deep water. This could save costly operation time, as the contractor can rely on MSVPs instead of measuring new SVPs.
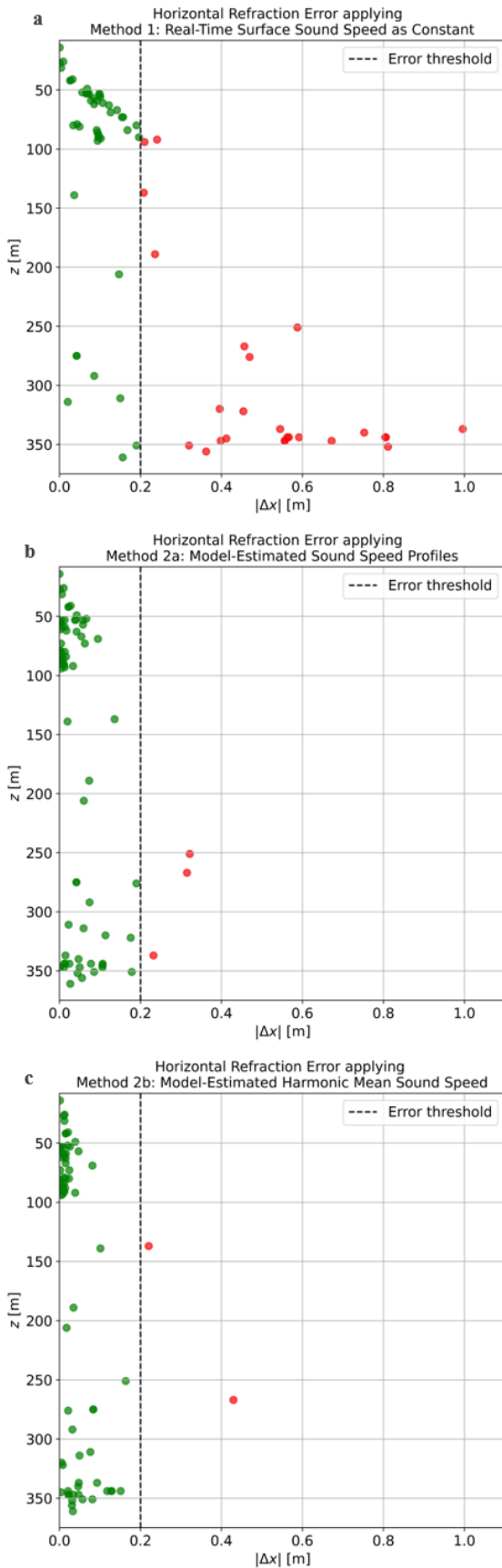
Figure 3.21 Refraction-induced horizontal positioning errors when calculating the horizontal displacement Eq. [3.5] when applying **a)** the CSSV method; **b)** the complete MSVP method; **c)** the combined MSVP method, and compare to the displacement based on observed SVPs measured on board of Van Oord's SRI vessel Stornes in the year 2020 in the North Sea. The error threshold $\delta_{|\Delta x|} = 0.20m$ (black dashed line).

4. OMBES METHOD

In the previous chapter, the harmonic mean sound velocity c_H was estimated either by considering the ISS sound velocity c_s as being constant with depth (CSSV profile, and thus $c_H \approx c_s$), or calculated from MSVPs that are empirically-derived using daily-mean temperature and salinity model data. As we restrict ourselves to the application of underwater acoustic positioning of FPROVs – e.g. close to the seafloor ($\pm 5m$), and working at small incident angles ($\theta_s < 6°$) – sea areas could be defined where as a result of using a constant SVP, the horizontal refraction-induced positioning error is still within acceptable margins for subsea rock installation projects. Depending on the geospatial location and the time of the year, the offshore contractor could omit the complexity of the SVP, and use the ISS sound velocity instead. In case a constant SVP leads to unacceptable positioning errors, the contractor can rely on MSVPs derived from Copernicus Marine products. A comparison with observations showed that daily-mean MSVPs suffice for accurate USBL positioning of FPROVs.

When extending the range of applications to the positioning of ROVs that are located with greater offset from the vessel compared to FPROVs, the use of simplified or model-based estimated SVPs (i.e. both erroneous SVPs) results in a greater mismatch in the estimated horizontal position. This is because the acoustic pulse refracts more with increasing incident angle (Snell's law). Therefore, the use of erroneous SVPs is more penalized. Consequently, the horizontal refraction-induced positioning error grows rapidly with increasing incident angle, and also grows with increasing depth and increasing stratification. Positioning of these ROVs requires a method that inverts the instantaneous SVP and therewith captures the more complex, short-term, spatiotemporal variations of the SVP.

Following a similar approach as Mohammadloo *et al.* (2019) and Keyzer *et al.* (2021), this chapter proposes a method to invert the SVP from multibeam echosounder (MBES) measurements. With high efficiency and wide coverage, MBES systems have become a vital instrument for conducting bathymetric surveys (Mohammadloo *et al.*, 2019; Bu *et al.*, 2021). The MBES transmits a ping of fan-shaped sonar beams – known as the swath (Figure 4.1) – perpendicular to the sailing direction. Beamforming at reception allows to estimate the water depths from the two-way travel time of the signals for a set of predefined beam angles, in combination with the SVP (Lurton and Augustin, 2010). This SVP is measured by lowering a sound velocity sensor or a conductivity-temperature-depth (CTD) sensor. To perform such a measurement, the vessel must stop and stay in a drift for the period of the SVP measurement. This is a laborious and time-consuming procedure. Just like with FPROV operations, the impracticality results in the acquisition of these measurements at low rates e.g. typically only a few are taken per survey. In case inaccurate or insufficient SVPs are used, refraction errors are introduced and the estimated bathymetry shows deformations, generally

Figure 4.1 Example of single-head multibeam echosounder with fan-shaped swath covering the seabed.

known as smileys and frownies because of the convex and concave shape of the estimated bathymetry along a swath (Keyzer *et al.*, 2021). Since it is common practice to carry out MBES surveys with a small overlap between adjacent swaths – by sailing adjacent tracks sufficiently close to each other – the depths as determined from the measured travel times along two overlapping swaths sometimes show significant differences in the estimated points on the seafloor (Mohammadloo *et al.*, 2019). These differences are in general due to the use of incorrect
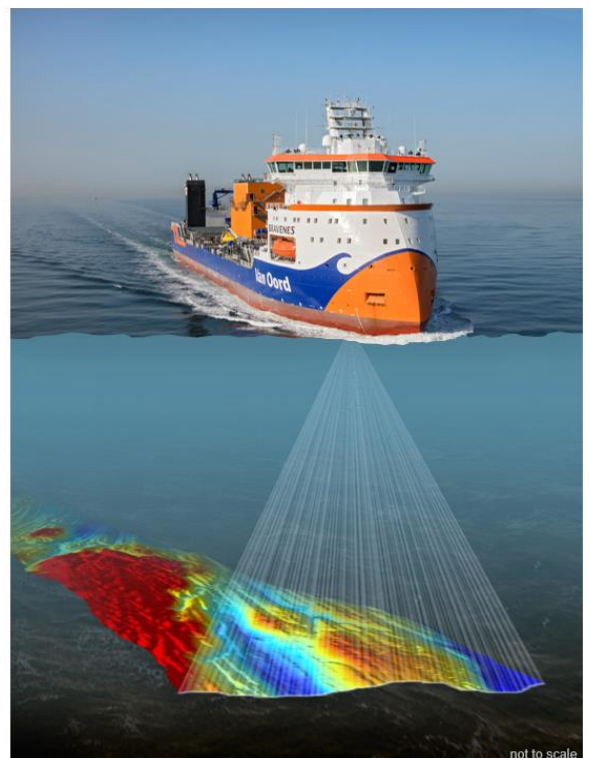
sound velocity information. Mohammadloo *et al.* (2019) proposes an algorithm that takes advantage of the overlap between survey lines by harnessing the power of redundancy of multiple observations in the overlapping area. By minimizing the depth differences along overlapping swaths, the mean sound velocity is resolved. This is essentially the harmonic mean sound velocity at the seafloor. Where the contributions of Mohammadloo *et al.* (2019) and Bu *et al.* (2021) focus on correcting MBES bathymetric measurements to obtain accurate underwater topography and yield the harmonic mean sound velocity as by-product, Keyzer *et al.* (2021) proposes a method to use the MBES measurements to invert the SVP. Keyzer *et al.* (2021) parameterized the SVP using 3 empirical orthogonal functions (EOFs) which are obtained from a sufficient number of historically-collected SVPs. Their method gives insight in the spatiotemporal variability of the sound velocity in the area of interest.

We would like to follow the method of Keyzer *et al.* (2021) but we do not have a set of historically-measured SVPs at a particular location. However, benefiting from the fact that the ROV is located close to the seafloor most of the time, the harmonic mean suffices. Therefore, the method presented in this chapter is similar to the one first presented by Mohammadloo *et al.* (2019). But instead of obtaining semi-synchronized overlap in MBES swaths by sailing adjacent tracks (e.g. single-head MBES configuration), we propose to obtain synchronized overlap in one single sailing track using a dual-head MBES configuration. This method allows to estimate the harmonic mean sound velocity near real-time along the track. The estimated harmonic mean sound velocity can serve as additional input for USBL positioning of ROVs that operate close to the seafloor. Another application is the acquisition of the harmonic mean sound velocity for survey vessels that cannot stop to take sound velocity dips manually, for instance when performing a bathymetric survey in a busy waterway. The along-the-track-estimated harmonic mean sound velocity can potentially improve the interpolation of the seabed topography when post-processing the hydrographic data.

In the industry, dual-head multibeam installations have been used to maximize survey productivity (Pocwiardowski, 2021). For example, in shallow waters the heads are tilted outwards to spread the soundings over a wider area, therewith increasing the across-track coverage while achieving a sufficient survey sounding density along the track. With each head producing 1024 soundings per ping, the survey efficiency is doubled when using a dual-head MBES system, with a total of 2048 soundings per ping. The increased coverage speeds up the survey (Figure 4.2a). Alternatively, the heads are tilted inwards to increase the sounding density (e.g. from 1024 to 2048 soundings per ping). This could be relevant when the client demands increased observable pipe surface and the avoidance of shadows when tracking a pipeline at the seabed. With this set-up the hit count of measurements per square meter is doubled (Figure 4.2b).

The chapter outline is as follows: paragraph 4.1 elaborates on the proposed method to invert the harmonic mean sound velocity from overlapping MBES measurements. It explains the adjustments made to the algorithm of Mohammadloo *et al.* (2019) for inversion with a dual-head MBES configuration. Next, it introduces the optimization solver used to minimize the depth differences in the overlap. In paragraph 4.2, a proof-of-concept is presented to show the working principle by means of a simulated survey with dual-head MBES. At last, paragraph 4.3 presents the results of multiple simulation experiments for assessing the performance of the optimization in its search to find the governing harmonic mean sound velocity.
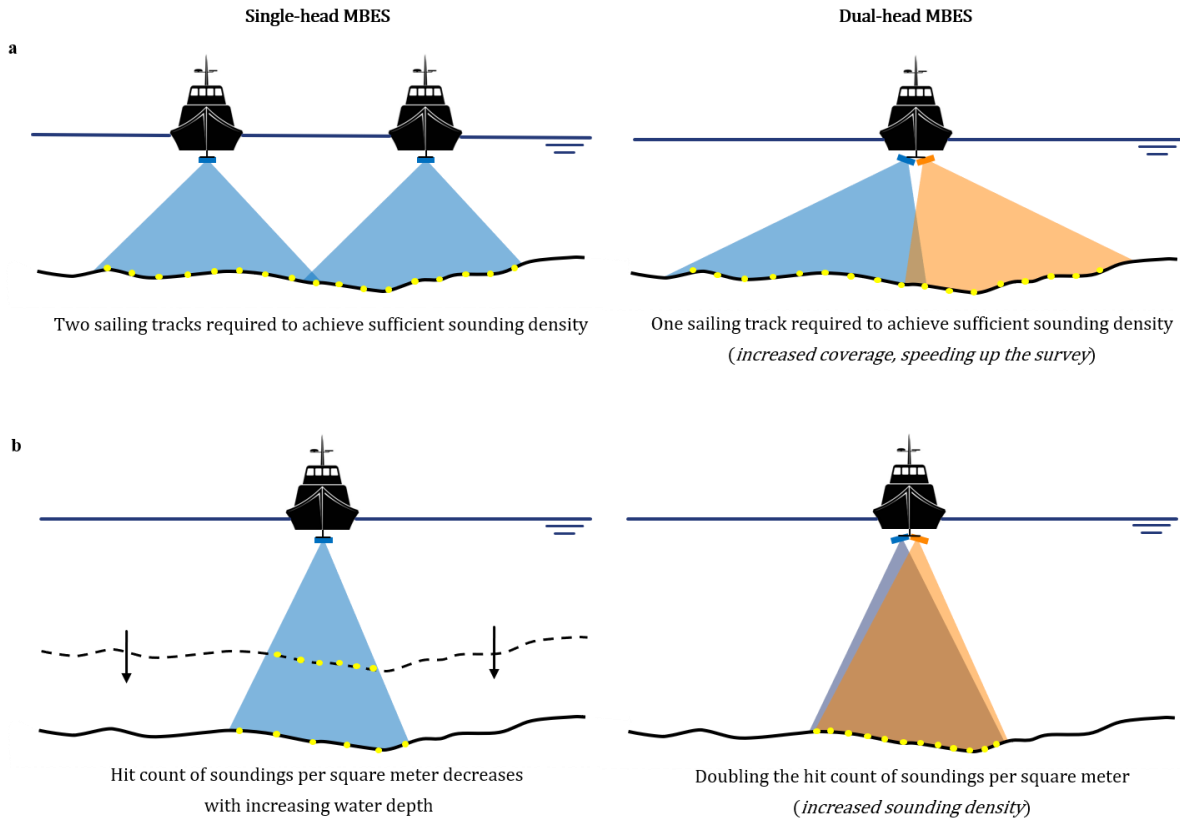
Single-head MBES   **Dual-head MBES**

a

Two sailing tracks required to achieve sufficient sounding density

One sailing track required to achieve sufficient sounding density
(*increased coverage, speeding up the survey*)

b

Hit count of soundings per square meter decreases
with increasing water depth

Doubling the hit count of soundings per square meter
(*increased sounding density*)

Figure 4.2 Single-head vs. dual-head MBES systems. **a)** increasing survey efficiency; **b)** increasing sounding density e.g. hit count of soundings per square meter seabed. The yellow dots indicate the soundings.

4.1 Inversion of the Harmonic Mean Sound Velocity

In this paragraph, we elaborate on the proposed method to invert the harmonic mean sound velocity from overlapping MBES measurements. Fundamental to the inversion method is the mismatch in the estimated bathymetry between two (semi-)synchronized overlapping swaths when using an erroneous SVP. Here, semi-synchronous overlap means that the two overlapping swaths are measured at a different time with a single-head MBES. Consequently, adjacent overlapping swaths are misaligned because for each track line the vessel is subject to different pitch and yaw. Because of the misaligned swaths, gridding and averaging of the soundings is required prior to using the inversion method. This will be explained in section 4.1.1. Synchronous overlap means that the two overlapping swaths are measured practically at the same time with a dual-head MBES. Hence, the swaths are aligned because the transducer heads are subject to approximately the same pitch and yaw. The inversion method can be applied to these aligned swaths without the need for gridding.

Figure 4.3a illustrates the concave-shaped (or smiley-shaped) estimated bathymetry when derived from two single-head MBESs of different sailing tracks, which is the set-up proposed by Mohammadloo *et al.* (2019) and adopted by Bu *et al.* (2021) and Keyzer *et al.* (2021). It is the ideal case for which the overlapping swaths (derived from adjacent sailed tracks) are perfectly aligned. The overlap between the two swaths is highlighted in green, and for this example, the overlap percentage is 16%. The overlap can be increased by widening the swath or by sailing tracks that are closer together. The close-up clearly shows the deformations for the two swaths due to the use of an erroneous SVP, which results in a mismatch in the estimated bathymetry, e.g. different depth estimates are provided in the overlapping area (between $x = 195\,m$ and $x = 205\,m$). Figure 4.3b illustrates the proposed configuration when using a dual-head MBES. In this example, the heads are $1.0\,m$ away from their centre line, and the overlap is 95%. When placing the multibeam heads closer together, the differences in depth measurements in the overlapping area are – while present – less pronounced. These differences are quantified using an energy

(objective) function. The inversion of the harmonic mean sound velocity follows from minimization of this energy function using an optimization algorithm. With an estimate of the harmonic mean sound velocity near real-time, the spatiotemporal variability of the underwater sound velocity can be captured without stopping the vessel for a manual SVP measurement.
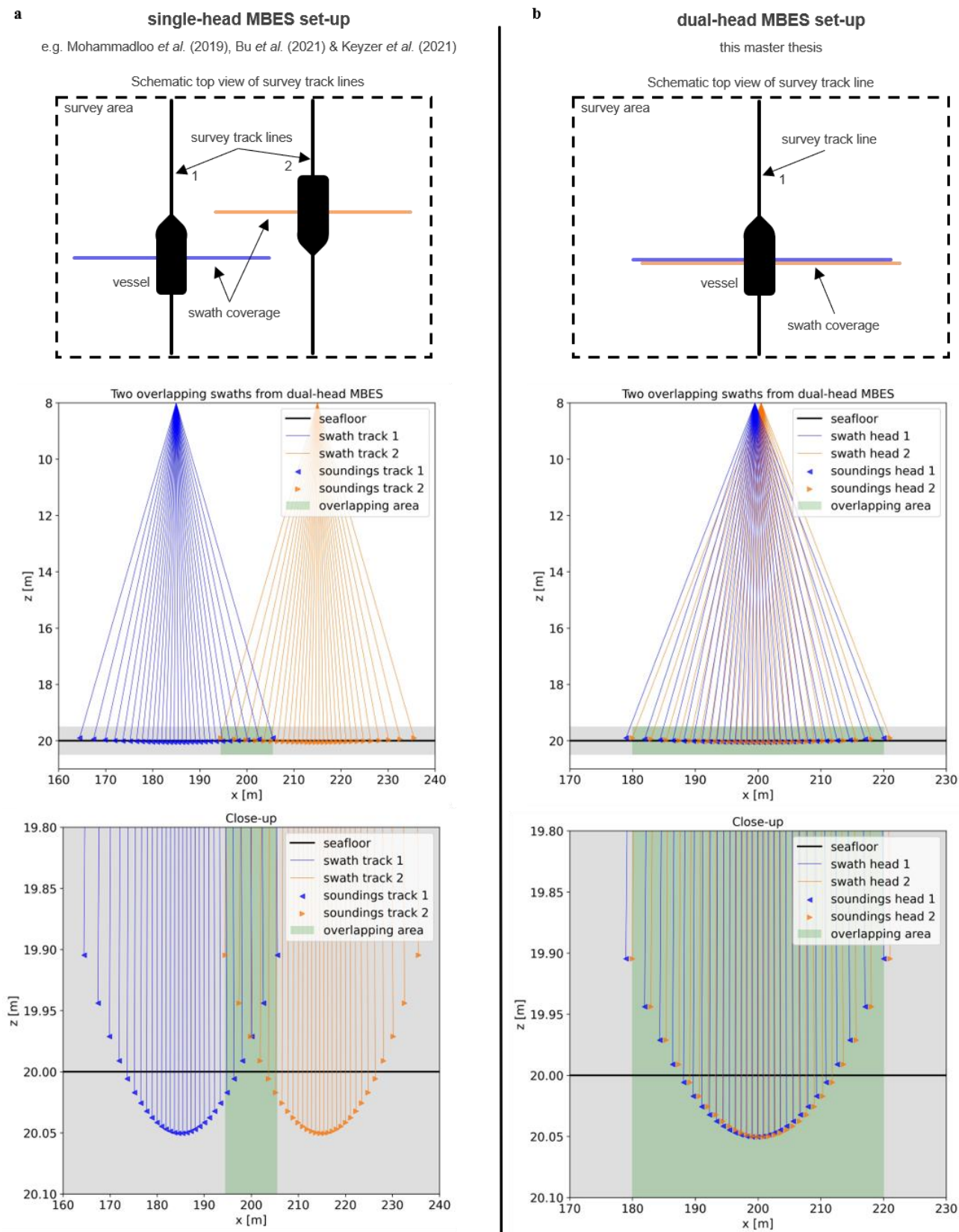

Figure 4.3 Different set-ups for obtaining overlap between swaths with MBESs. **a)** overlap from two single-head MBESs by sailing adjacent tracks; **b)** overlap from dual-head MBESs in one sailing track.

4.1.1 Energy function

The inversion of the harmonic mean sound velocity is evaluated using an energy function, which quantifies the agreement in water depths in the overlapping area. The algorithm was first proposed by the Acoustics Group of the TU Delft. Through cooperation with the Quality Positioning Services (QPS) company, the algorithm has been implemented as the *TU Delft Sound Speed Inversion Tool* in QPS Qimera (Mohammadloo *et al.*, 2019). The meaningful inversion method allows for a completely automated refraction error correction, and aims to obtain more accurate bathymetric data while honouring the physics of acoustic ray bending.

For practical application, the bathymetric data must be processed prior to using the energy function. It requires noise removal, patch test (e.g. roll/pitch/heading offsets) and tide correction (Mohammadloo *et al.*, 2019). Then, the soundings are gridded and averaged. For this data processing method, we follow Mohammadloo's study. It will lead to the definition of a 3D energy function – as currently being implemented in QPS Qimera – applicable for overlap obtained from both single-head and dual-head MBES configuration.

For the proof-of-concept, we simplify the problem to 2D when omitting that the vessel is subject to pitch and yaw. This simplification allows to evaluate the inversion of the harmonic mean sound velocity of two synchronized pings e.g. one per head, and thus, two aligned swaths. We adopt the 2D energy function defined by Keyzer *et al.* (2021), which is a modified version of the 3D energy function from Mohammadloo *et al.* (2019).

3D energy function

The first step is to partition the soundings of the two multibeam swaths into several subregions r_n along the direction of the survey track line. Then, a grid aligned to the mean heading of the pings in the subregion is defined, as shown in Figure 4.4. Here, the X and Y axis of the grid are defined perpendicular and parallel to the mean heading direction, respectively. The partitioning of the two swaths into subregions allows to ray-trace consecutive pings in a subregion with the same harmonic mean sound velocity.
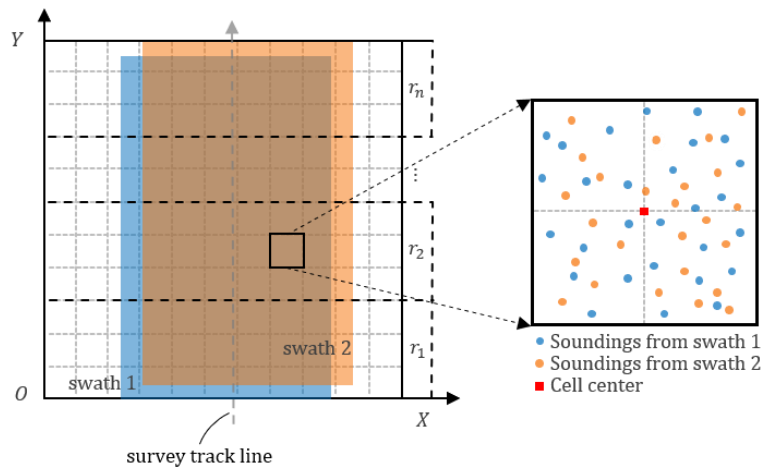

Figure 4.4 Definition of the grid and data partition for the two swaths (redrawn from Bu *et al.* 2021); r_1 to r_n represent the divided subregions.

Following Mohammadloo *et al.* (2019), the energy function is defined as:

$$E(\hat{\boldsymbol{g}}) = \sum_{m=1}^{M} \sqrt{\frac{1}{\sum_{n=1}^{N} K_{m,n}} \sum_{n=1}^{N} \sum_{k=1}^{K_{m,n}} \left(z_{m,n,k}(\boldsymbol{g}_n) - \bar{z}_m(\boldsymbol{g}_n) \right)^2}$$

4.1

where M is the total number of grid cells covering the overlap in a subregion r. N is the number of swaths ($N = 2$). $K_{m,n}$ is the total number of depth measurements (or soundings) from the nth swath located within a cell m. $z_{m,n,k}$ [m] is the kth depth measurement from the nth swath in the mth cell considered (which is calculated with Eq. [4.3]). $\bar{z}_m$ [m] is the depth of the mth cell centre, which is the weighted mean of $z_{m,n,k}$ with the weight function being the inverse cubed horizontal distance between the location of the measurements and the cell centre i.e. the cubed Euclidean distance d [m] between the Cartesian coordinates of the measurement point k and point m_0 (the cell centre):

$$\bar{z}_m(\boldsymbol{g}_n) = \sum_{n=1}^{N}\sum_{k=1}^{K_{m,n}} \frac{1}{\mathrm{d}^3(k,m_0)} \sum_{n=1}^{N}\sum_{k=1}^{K_{m,n}} \frac{z_{m,n,k}(\boldsymbol{g}_n)}{\mathrm{d}^3(k,m_0)} \qquad 4.2$$

$$\mathrm{d}(k,m_0) = \sqrt{\left(x_k - x_{m_0}\right)^2 + \left(y_k - y_{m_0}\right)^2}$$

In Eq. [4.1], $\hat{\boldsymbol{g}}$ [s^{-1}] denotes a vector containing the estimated constant sound velocity gradients for the number of swaths $N = 2$. For a dual-head set-up, the two estimates are approximately equal as the multibeam heads are mounted close together and the soundings are obtained simultaneously along one-single track line. For a single-head set-up, the distance between the two multibeams – which is the distance between adjacent track lines – is much larger and the time it takes before sailing the adjacent track may be considerable depending on the water depth and survey type (e.g. 20 to 30 minutes). Therefore, the two estimated gradients can be different as a result of the spatiotemporal varying SVP.
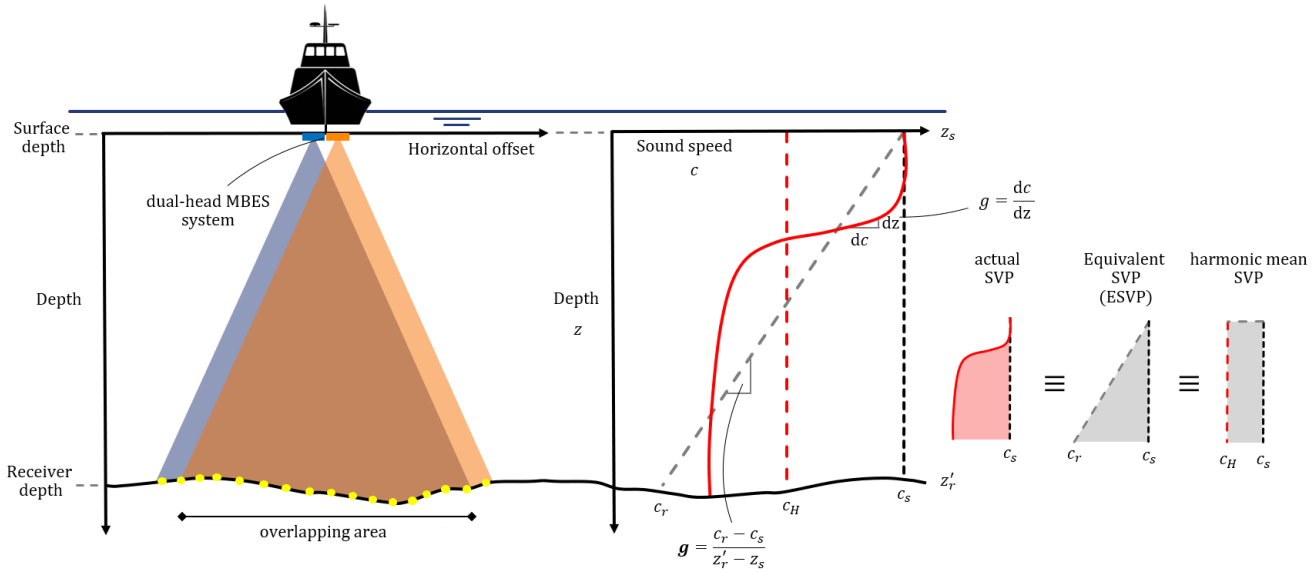

Figure 4.5 Left: schematization of dual-head multibeam echosounder system mounted on a survey vessel. Right: relationship between the actual SVP, the equivalent SVP, and the harmonic mean SVP. The yellow dots indicate the soundings.

The depth of each sounding is calculated with the ESVP ray-tracing algorithm. A detailed derivation of the algorithm is presented in chapter 2, where Geng and Zielinksi (1999) fundamentally prove that the ESVP can effectively replace the actual SVP. Figure 4.5 shows the similarities between the actual SVP, the ESVP and the harmonic mean SVP. We recall the formula for calculating the location where the acoustic pulse impinges on the seafloor. The expression is derived in chapter 2 (Eq. [2.23]) and is used to calculate the depth position $z_{m,n,k}$ in the energy function:

$$z_{m,n,k}(\boldsymbol{g}_n) = z_{s_{m,n}} + \frac{\sin\left(2\arctan\left(e^{t_{m,n,k}\boldsymbol{g}_n}\tan\left(\theta_{s_{m,n,k}}/2\right)\right)\right) - \sin\theta_{s_{m,n,k}}}{p_{m,n,k}\boldsymbol{g}_n} \qquad 4.3$$

where:

- $z_{s_{m,n}}$ $[m]$, is the depth of the multibeam transducer head;
- $t_{m,n,k}$ $[s]$, is half of the one-way travel time of the acoustic signal, recorded by the multibeam transducer;
- $\theta_{s_{m,n,k}}$ $[°]$, incident ray angle at multibeam transducer head, surface level $z_{s_{m,n}}$;
- $p_{m,n,k} = \sin\theta_{s_{m,n,k}}/c_{s_n}$, is Snell's constant, with c_{s_n} $[m/s]$ the surface sound velocity at the multibeam transducer head. A sound velocity sensor is often integrated in the multibeam head.

2D energy function

In 2D, the energy function of Eq. [4.1] can be simplified (Keyzer *et al.*, 2021):

$$E(\widehat{\boldsymbol{g}}) = \sum_{n=1}^{N} \sqrt{\frac{1}{K_n} \sum_{k=1}^{K_n} \left(z_{n,k}(\boldsymbol{g}_n) - \bar{z}(\widehat{\boldsymbol{g}})\right)^2}$$ 4.4

where N is the number of swaths ($N = 2$). K is the total number of depth measurements (or soundings). $z_{n,k}$ $[m]$ is the kth depth measurement (or sounding) from the nth swath, and is similarly expressed in terms of the constant sound velocity gradient using the ESVP theory:

$$z_{n,k}(\boldsymbol{g}_n) = z_{s_n} + \frac{\sin\left(2\arctan\left(e^{t_{n,k}\boldsymbol{g}_n}\tan\left(\theta_{s_{n,k}}/2\right)\right)\right) - \sin\theta_{s_{n,k}}}{p_{n,k}\boldsymbol{g}_n}$$ 4.5

In Eq. [4.4], $\bar{z}$ $[m]$ is the true depth approximated by combining the depth estimates of the two swaths.

$$\bar{z}(\widehat{\boldsymbol{g}}) = \sum_{n=1}^{N} \frac{1}{K_n} \sum_{k=1}^{K_n} z_{n,k}(\boldsymbol{g}_n)$$ 4.6

Since gridding is no longer needed, it is required that the two swaths are aligned and overlap. This 2D definition is less versatilely applicable for a single-head MBES set-up than for a dual-head MBES set-up. The overlapping swaths of single-head MBESs do not comply with the requirement to align, because the vessel is – for each survey track line – subject to pitch and yaw (Figure 4.6). To this end, data processing is required before applying the inversion algorithm. This includes gridding and averaging of the soundings, and thus application of the 3D energy function, as defined by Mohammadloo *et al.* (2019). In contrast, for our proposed dual-head MBES set-up, the two swaths are aligned because the transducer heads are subject to approximately the same pitch and yaw. Therefore, gridding and averaging is not required. This set-up allows to invert the harmonic mean sound velocity near real-time by computing the 2D energy function with soundings from one ping per head.
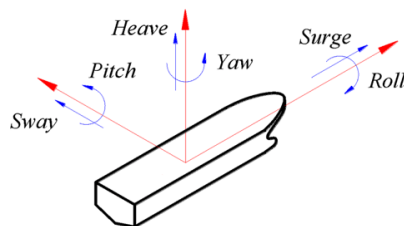

Figure 4.6 The vessel's motions

From constant sound velocity gradient to harmonic mean sound velocity

Both energy functions (Eq. [4.1] and Eq. [4.4]) yield an optimized vector $\hat{\boldsymbol{g}}$ containing two constant sound velocity gradients. In order to obtain the harmonic mean sound velocities, a simple translation is needed. Based on Figure 4.5, and using $c_r = 2c_H - c_s$, it follows that the constant sound velocity gradient is $\boldsymbol{g} = (c_r - c_s)/(z_r' - z_s) = (2c_H - 2c_s)/(z_r' - z_s)$.

Rewriting yields:

$$\hat{c}_H = \hat{c}_s + \frac{1}{2}\hat{\boldsymbol{g}}(\bar{z} - \hat{z}_s)$$

4.7

where:

- $\hat{c}_H$ $[m/s]$, a vector containing the two optimized harmonic mean sound velocities;
- $\hat{c}_s$ $[m/s]$, a vector containing the two surface sound velocities at the multibeam transducer head, measured at surface level $\hat{z}_s$ $[m]$;
- $\bar{z}$ $[m]$, the estimate of the true depth. Either using Eq. [4.2] or Eq. [4.6], the optimized gradients provide the average seafloor depth in the overlapping part.

As already mentioned, when the inversion follows from overlap of two single-head MBES systems, the optimized harmonic mean sound velocities $\hat{c}_H$ can be different as the depth estimates are subject to spatiotemporal-varying sound velocity conditions (e.g. distance between adjacent track lines and time between obtaining the overlap). However, when the inversion is performed with a dual-head MBES configuration, the two optimized harmonic mean sound velocities $\hat{c}_H$ are approximately equal as the overlap is obtained simultaneously along the same track line. To this end, one can select one of the two estimates (or simply take the average) and consider this value as the inverted harmonic mean sound velocity.

4.1.2 Constrained Optimization BY Linear Approximation (COBYLA)

The search for the best harmonic mean sound velocity is an optimization problem. When the energy function $E(\hat{\boldsymbol{g}})$ is minimum, the depth variations are minimized. This means maximum agreement is found between the two overlapping swaths and the bathymetry is free of refraction-induced errors. The function then returns the associated harmonic mean sound velocity, which is a simplified but accurate representation of the true SVP.

In order to find the harmonic mean, information about the derivative of the energy function is required. However, it is difficult to calculate the derivative of the energy function with the nonlinear ESVP ray-tracing algorithm Eq. [4.5] embedded into it. Therefore, we prefer the use of derivative-free optimization. We choose to use one of Powell's nonlinear derivative-free optimization solvers named COBYLA (Powell, 1994). COBYLA stands for Constrained Optimization BY Linear Approximation. The algorithm is an extension to the Nelder-Mead simplex algorithm (Nelder and Mead, 1965) and can handle (non)linear constraints. As with methods like Nelder-Mead, COBYLA constructs successive approximations being formed by linear interpolation at $N + 1$ function evaluation points in the space of N variables ($N = 2$). One can regard these interpolation points as vertices of a simplex. Visualization of the algorithms is quite striking, as the simplex appears to crawl downhill like some sort of mathematical amoeba.

The motivation for using COBYLA instead of Nelder-Mead is the possibility to add constraints. Placing hard limits on the value of the variables prevents us from searching in the wrong direction in case the minimum is difficult to locate. This is illustrated with Figure 4.7. The contours of the energy field $E(\hat{c}_H)$ – translated with Eq. [4.7] – are plotted as function of the harmonic mean sound velocity of multibeam swath 1 and swath 2 (which are approximately equal). Figure 4.7a shows the clearly-defined minimum of the energy function for the case where

the heads have a swath width of 120°. Both Nelder-Mead and COBYLA would perform well and can accurately find the optimized values. When decreasing the swath width to 30°, the energy field changes dramatically into a V-shaped valley (Figure 4.7b). Once arrived in the valley, the algorithm has difficulty to determine where the minimum is located because of the mild gradients in the alongside direction. Both Nelder-Mead and COBYLA do not guarantee to find the minimum and often get stuck in the valley. However, without setting constraints, the algorithm can crawl outside the illustrated domain and may return physically unrealistic values. Moreover, these unrealistic values do not maintain the overlap between multibeam swaths. Without this overlap, the problem is undefined and inversion is impossible.
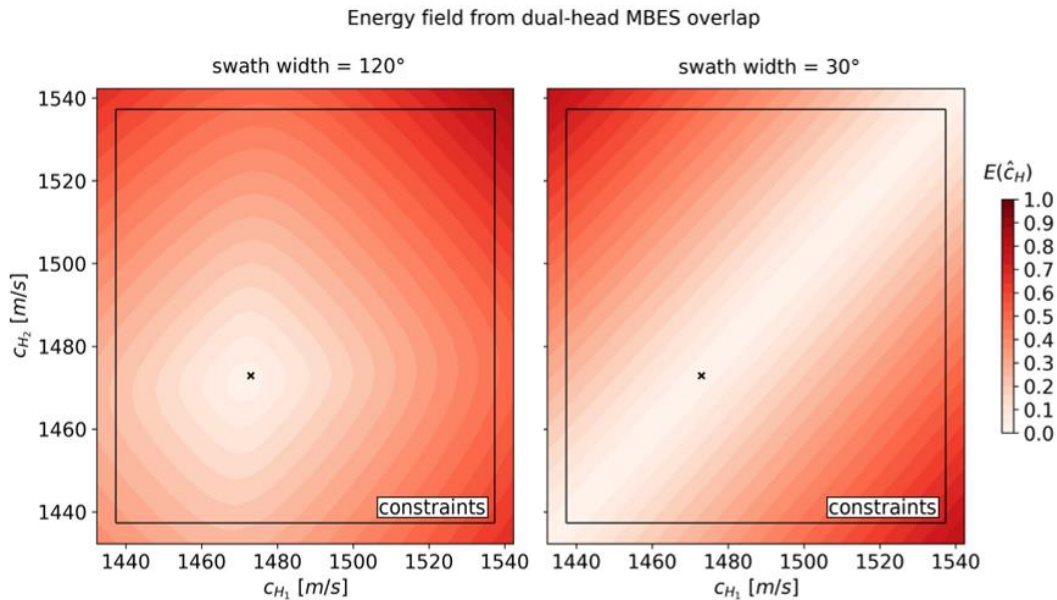

Figure 4.7 Contour plot of energy function Eq. [4.4] as function of the harmonic mean sound velocity of two multibeam heads. The overlap between swaths is obtained from a dual-head MBES set-up; both heads have a swath width of **a)** 120° and **b)** 30°. The cross indicates the true minimum. Black lines squaring the domain are the constraints as defined by Eq. [4.8] and Eq. [4.9], translated from constant sound velocity gradient to the harmonic mean sound velocity using Eq. [4.7].

To prevent the algorithm from searching in the wrong the direction, constraints must be set, something Nelder-Mead cannot deal with. Fortunately, COBYLA is able to deal with inequality constraints. So the problem can be written as:

$$\min E(\hat{\boldsymbol{g}})$$
$$\text{subject to } \hat{\boldsymbol{g}}_{low} \leq \hat{\boldsymbol{g}} \leq \hat{\boldsymbol{g}}_{up}$$

4.8

where the lower and upper bound of the constraints are given as:

$$\begin{cases} \hat{\boldsymbol{g}}_{low} = (1400 - \hat{c}_s)/\bar{z} \\ \hat{\boldsymbol{g}}_{up} = (1600 - \hat{c}_s)/\bar{z} \end{cases}$$

4.9

These constraints form a square box as can be seen from Figure 4.7. Following Bu *et al.* (2021), COBYLA is also randomly initialized with a vector $\hat{\boldsymbol{g}}$ that honours these bounds, but the guess may not be zero. From there the algorithm crawls downhill and finds the optimal solution in approximately 50 function evaluations. The maximum number of evaluations were set to 200 to force termination in case the algorithm does not converge.

4.2 Proof-of-concept

Similar to Keyzer *et al.* (2021), we present a proof-of-concept, where synthetically generated SVPs are inverted from a simulated survey with a dual-head MBES. We construct a Gaussian random field with a constant depth of $40\ m$ and a standard deviation of $5\ cm$ (Figure 4.8a). The survey is simulated by sailing a track line in northern direction. Every $25\ m$ (red dots), a ping is evaluated and the overlap in the two swaths is used to invert the harmonic mean sound velocity. The multibeam heads are distanced $100\ cm$ from their centrelines and have no angular offset. The swath width is set to 120°, corresponding to 98% overlap (e.g. covering the seafloor between $x = 145\ m$ and $x = 255\ m$, Figure 4.8a).
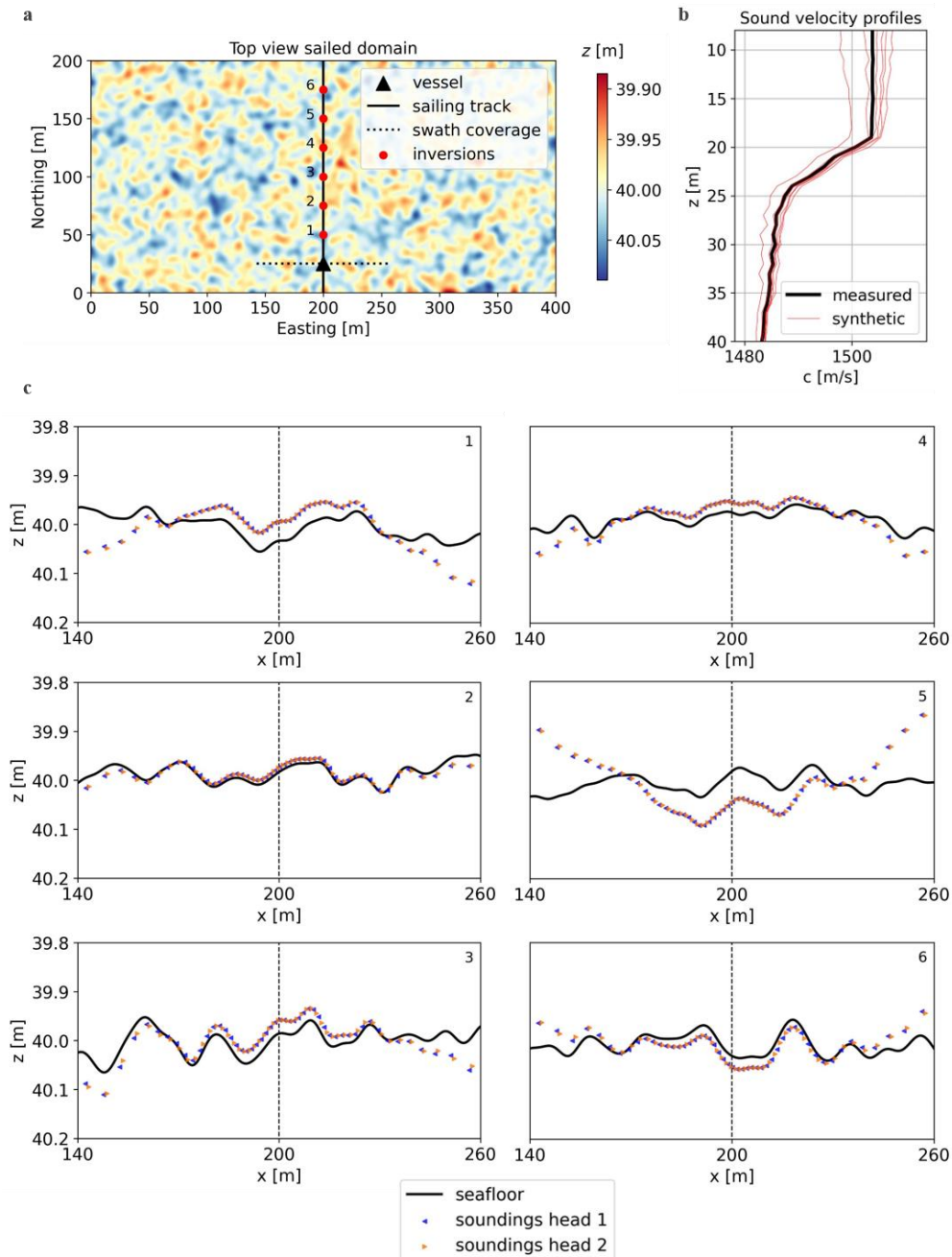

Figure 4.8 a) The domain with a Gaussian random seafloor at the depth $40\ m$ and the sailed track. The red dots indicate the locations where the harmonic mean sound velocity is inverted by minimizing the depth differences between overlapping swaths of a dual-head MBES; **b)** The measured and synthetic SVPs. The measured profile correspond with the vessel's position; the synthetic profiles correspond with the red dots along the sailing track. **c)** The estimated bathymetry from a dual-head MBES. For clarity, the swaths consist of 50 soundings instead of the 256 or 1024 in practical applications. The deformations from the seafloor are a result of the use of an erroneous SVP, in this case the measured profile in **b**.

In order to calculate the travel times of the soundings, an SVP is required. For the simulation, we used an SVP measured by Van Oord's SRI vessel Stornes in the North Sea (black profile in Figure 4.8b). The profile is usually taken at the start of the survey and is used to calculate the locations where the sound pulses impinge on the seafloor. During the survey, the SVP will show spatiotemporal variation. Therefore, synthetic profiles are randomly generated by adding white noise and by transforming the measured profile with a hyperbolic tangent function. In this way, the variations are most prominent in upper water layers, therewith mimicking the short-term variations of the sound velocity. The resulting synthetic SVPs are given in Figure 4.8b and correspond with the 6 locations indicated with red dots in Figure 4.8a. They are considered as the <u>true SVPs</u>, while the measured profile becomes the <u>erroneous SVP</u> from the moment the survey starts.

Without replacing the erroneous SVP, refraction errors are introduced. This is illustrated for 6 ping evaluations. Their soundings are shown in Figure 4.8c. In general it holds that the estimated bathymetry has a convex (concave) shape in case the harmonic mean sound velocity is overestimated (underestimated), which deformations are known as smileys (frownies) (Keyzer *et al.*, 2021). Figure 4.9a summarizes this phenomena.
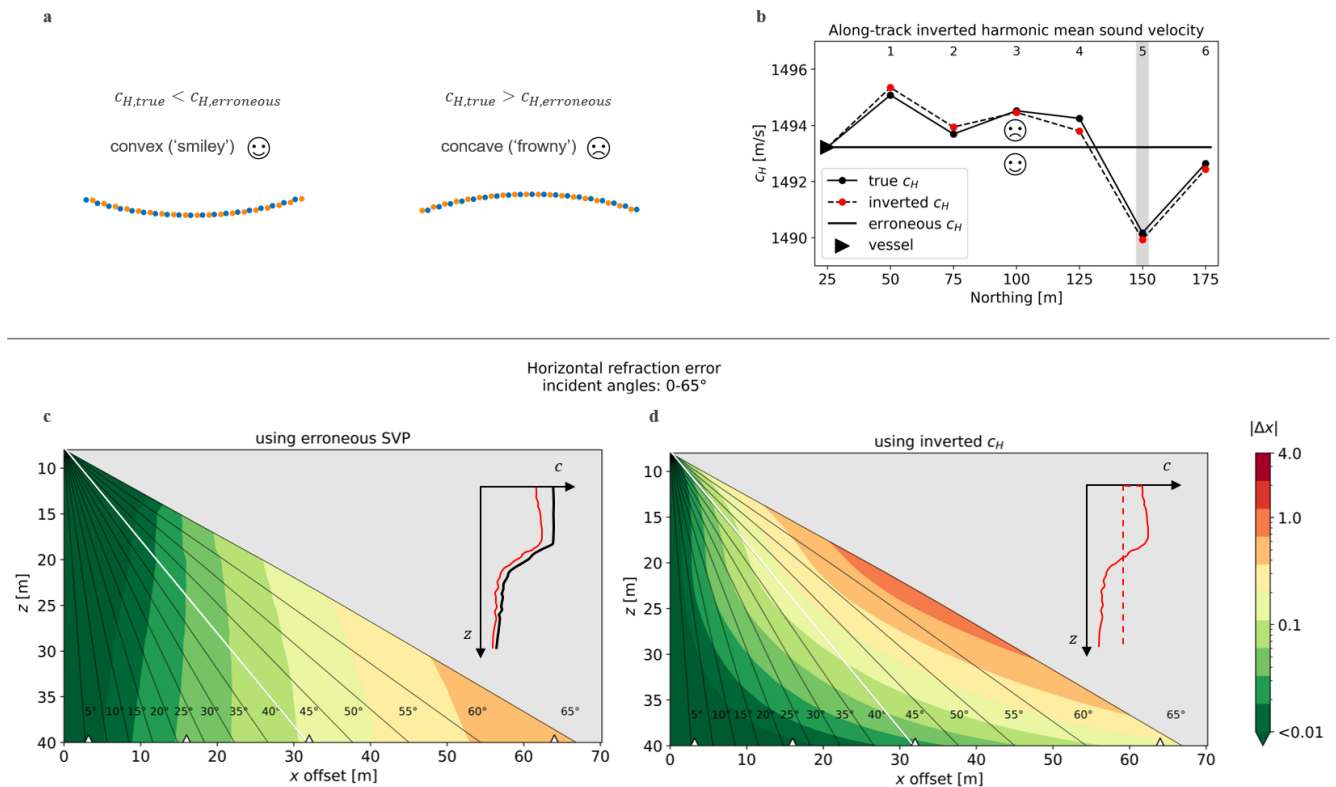

Figure 4.9 a) Shape of refracted bathymetry and its relationship with the incorrect estimated harmonic mean sound velocity c_H.**b)** Inverted harmonic mean sound velocities along the survey line track simulated in Figure 4.8a. **c, d)** Horizontal refraction-induced error with depth for acoustic pulses sent with angles θ between 0-65°. The true SVP (red synthetic profile) is ray-traced and compared with the (**c**) erroneous SVP (black measured profile) and the (**d**) inverted harmonic mean SVP (red dashed profile). MBESs are located at $z = 8\ m$. White triangles at bottom indicate fixed distances in the horizontal offset, 0.1/0.5/1/2 WD (water depths) from the centre of the USBL transceiver. White line highlights the 1 WD horizontal offset over the entire water column.

Figure 4.9b shows the inverted harmonic mean sound velocities for the 6 ping evaluations along the survey track line, estimated using the (2D) energy function and the ESVP ray-tracing algorithm described in paragraph 4.1. There is good agreement between the inverted and true harmonic mean sound velocities, with deviations less than 0.5 m/s. This means refraction errors are reduced, resulting in corrected MBES bathymetric measurements. The slight mismatch in estimation exist due to the effect of an uneven seabed topography. This systematic error is introduced when using one constant gradient ESVP for a large angular coverage, while in reality the ESVP per beam is slightly different because of varying seabed topography. It was found that in the idealized case – a flat seabed – the algorithm is able to exactly estimate the true value.

While the contributions of Mohammadloo *et al.* (2019) and Bu *et al.* (2021) focus on correcting MBES bathymetric measurements to obtain accurate underwater topography and yield the harmonic mean sound velocity as by-product, we focus on the quality of the inverted harmonic mean. In fact, we go a step further and analyse whether the inverted harmonic mean sound velocity can be used for acoustic positioning of ROVs with USBL. We assess the quality by quantifying the horizontal refraction-induced error with the ESVP ray-tracing algorithm (Eq. [2.24] in paragraph 2.4) [6]. For demonstration we zoom in on location 5 (highlighted with grey colour in Figure 4.9b), and show the horizontal refraction errors for common sounding geometries. The refraction errors follow from comparison of two SVPs: the erroneous SVP versus the true SVP (4.9c) and the inverted harmonic mean SVP versus the true SVP (4.10d).

Figure 4.9c shows the scenario when one decides to continue using the erroneous SVP. Despite vertical variations of the sound velocity, the use of the erroneous SVP yields quite satisfactory results i.e. approximately less than $10\ cm$ error when the ROV is within 1 WD (water depth) away from the USBL transceiver (which is below the $\theta = \arctan(1) = 45°$ line, highlighted in white). When the ROV is located at shallower depths, the accuracy can be guaranteed even for larger incident angles. However, as expected, the horizontal positioning accuracy decreases with increasing depth and incident angle.

Figure 4.9d shows the scenario when using the inverted harmonic mean sound velocity. Up to 2 WD (water depths) away from the USBL transceiver, the horizontal refraction error does not exceed $20\ cm$ when manoeuvring over the seabed, compared to $60\ cm$ when using the erroneous SVP. Because the inversion only provides the harmonic mean at the seafloor, its applicability for acoustic positioning is limited to ROVs that are operating close to the seafloor. Moreover, close to the transceiver's nadir the error is small because refraction is limited for small incident angles. In fact, the horizontal positioning accuracy shows signs of an exponential decay, which makes sense as the constant sound velocity gradient (and indirect the harmonic mean sound velocity) is raised to Euler's number in the ESVP ray-tracing formula (Eq. [2.24]). Higher up in the water column, the accuracy quickly decreases for large incident angles. For this set of angles and depth levels, the harmonic mean does not suffice. Instead, one should use an SVP that fully covers the details of the vertical variations in the sound velocity. However, if the job is to inspect the seafloor, we advise to descend the ROV along the transceiver's nadir towards the seafloor before moving away from the transceiver. In this way, the ROV stays within an accurate positioning zone. This inversion method is able to provide frequent updates on the change in the harmonic mean sound velocity, and therewith, it will increase the accuracy of USBL positioning. There is no need to take additional SVP casts, as long as the ROV stays close to the seafloor or transceiver's nadir.

4.3 Experiments

In this paragraph, we conduct a set of experiments that give information about the configuration of the dual-head multibeam for optimal performance when inverting the harmonic mean sound velocity. As mentioned previously, for functionality of the inversion method, overlap between the two swaths is required. Therefore, an important issue is to investigate the performance of the optimization algorithm for varying swath widths in different water depths. Firstly, in the distance between the multibeam heads is investigated for the case where both heads are mounted close together (e.g. 50-200 cm), and for the case where the heads are separated and mounted on the port and starboard side with a distance of $25\ m$ (section 4.3.1). Secondly, the angular offset is investigated with both multibeam heads tilted inwards, and the scenario where different angular offsets per head (section 4.3.2). At last, the effect of water depth and an uneven seabed topography is investigated (4.3.3). Table 4.1 gives an overview of the experiments and their scenarios. We highlighted (with green colour) the set-up that led to the best performance of the inversion algorithm i.e. wide configuration with one or two inward-tilted multibeam heads.

---

[6] The ROV's depth estimate is a combined estimate of information obtained from pressure sensors. Therefore, the vertical refraction-induced errors originating from the use of erroneous SVPs by the USBL positioning system are inferior.
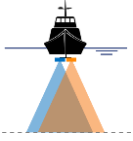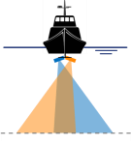
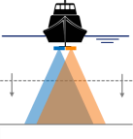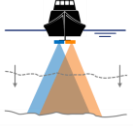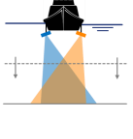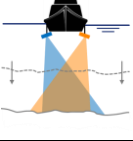| Description experiment	Scenario	Distance heads [cm]	Angular offset heads [°] Starboard side (blue)	Port side (orange)	Water depth [m]	Seabed type	Schematic
Effect of distance between multibeam dual-heads (**4.3.1**)	close configuration	50	0	0	40	flat	
		100	0	0	40	flat	
		200	0	0	40	flat	
	wide configuration	2500	0	0	40	flat	
Effect of angular offset of multibeam dual-heads (**4.3.2**)	close configuration with both heads tilted inwards	100	10	10	40	flat	
		100	20	20	40	flat	
	close configuration with one head tilted inwards	100	0	10	40	flat	
		100	0	20	40	flat	
	wide configuration with both heads tilted inwards	2500	10	10	40	flat	
		2500	20	20	40	flat	
	wide configuration with one head tilted inwards	2500	0	10	40	flat	
		2500	0	20	40	flat	
Effect of water depth and uneven seabed topography (**4.3.3**)	close configuration	100	0	0	20	flat	
		100	0	0	40	flat	
	close configuration	100	0	0	20	uneven	
		100	0	0	40	uneven	
	wide configuration with both heads titled inwards	2500	20	20	20	flat	
		2500	20	20	40	flat	
	wide configuration with both heads titled inwards	2500	20	20	20	uneven	
		2500	20	20	40	uneven	

Table 4.1 Overview of experiments conducted to investigate effect of multibeam head configuration on performance of optimization solver.

TUDelft

Van Oord
Marine ingenuity

All experiments use the <u>measured (erroneous)</u> and <u>synthetic (true)</u> SVP as shown in Figure 4.10a, and will be cut off at depths of $20\ m$ and $40\ m$, depending on the experiment. Using the erroneous SVP, the depth measurements are derived from the one-way travel time for a set of predefined beam angles. This results in refraction errors affecting the position of the depth estimate.
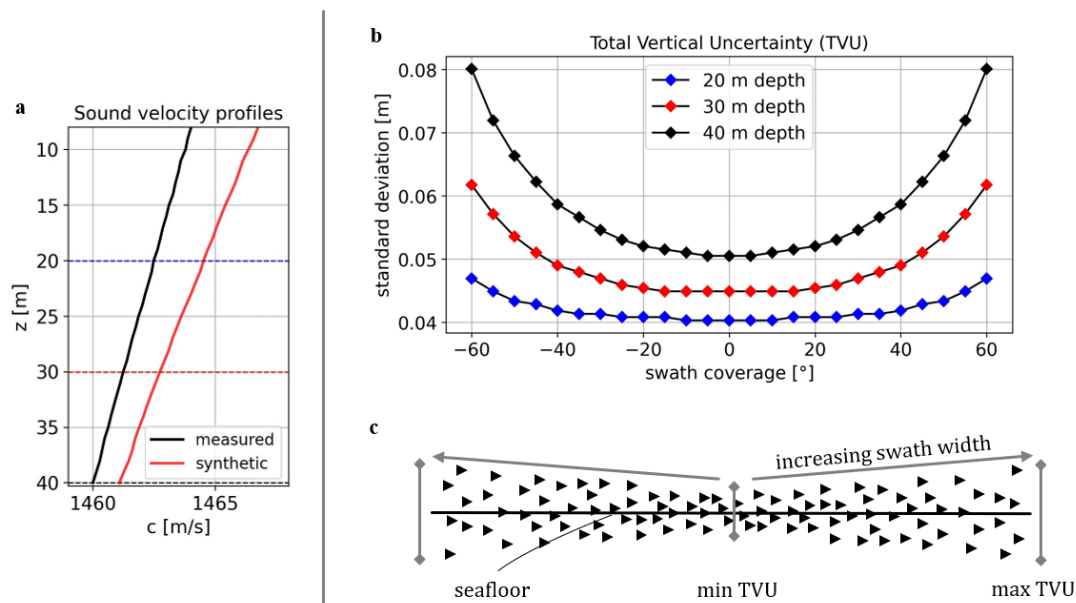

Figure 4.10 a) The measured and synthetic SVP. The measured profile is taken at the start of the survey and is considered as the erroneous SVP. The synthetic profile is the true profile at the location where the inversion takes place. **b)** Standard Deviation (SD) of the total vertical uncertainty (TVU) for different water swath widths and water depths. **c)** Schematization of effect of TVU on depth measurements with increasing swath width. The standard deviations in **(b)** are default specs for TVU calculation in the software HYDROBIB (HydroCharting ApS, 2021) with MBES R2Sonic 2024 at $8\ m$ depth. Frequency: 400 kHz. Pulse length: $30\ \mu s$.

Apart from the uncertainty in the SVP, other sources of uncertainties affect the derived depth, such as those in the motion and attitude sensors. They constitute to the so-called Total Vertical Uncertainty (TVU), which is the vertical component in the error budget. The TVU does <u>not</u> include the refraction error due to varying SVP. But it includes the measurement error associated with the sound velocity sensor e.g. random noise in the circuit, systematic calibration error, and systematic clock error.

The quantification of the contributing uncertainty sources is outside the scope of this thesis. An interesting reader is referred to the model developed by Hare (1995), which is widely used for bathymetric uncertainty prediction (Mohammadloo, Snellen and Simons, 2020). In this thesis, we use the software tool HYDROBIB, which is a hydrography training utility developed by Jesper Højdal (HydroCharting ApS, 2021). The R2Sonic 2024 head was selected and the accuracy specs were set to default. Subsequently, the standard deviation of the TVU was collected for different swath widths and water depths (Figure 4.10b). Figure 4.10b shows that the uncertainty increases with increasing water depth, in particular for the outer beams. Figure 4.10c highlights the effect of increased uncertainty with increasing swath width. The minimum uncertainty is found at the nadir while the outer beams have the largest uncertainty in the depth estimate.

The general idea is that including these uncertainties to the estimated soundings in the following experiments results in better and more realistic assessment of the performance of the optimization solver, and thus, the ability to invert the harmonic mean sound velocity. In order to analyse the performance of the optimization algorithm, we ran the COBYLA solver 100 times and initialized the algorithm randomly with values that honour the bounds as specified in Eq. [4.9]. This enables us to evaluate whether the output is consistent when redoing the same calculation with different starting values. In addition, we varied the swath width between 50-120° to see the performance of the different configurations for different widths.

4.3.1 Investigating the effect of distance between multibeam dual-heads

In this section, we assess the distance between the multibeam dual-heads. Generally, an increase in the distance between the heads increases the depth differences between the overlapping swaths (Figure 4.3 shows the extreme comparison). Therefore, it is expected that the inversion algorithm has better performance for multibeams that have greater spacing between their centre lines.

Figure 4.11 shows a schematization of two multibeam dual-head configurations. The scenarios are defined as follows and were tested for a flat seabed at $40\ m$ depth:
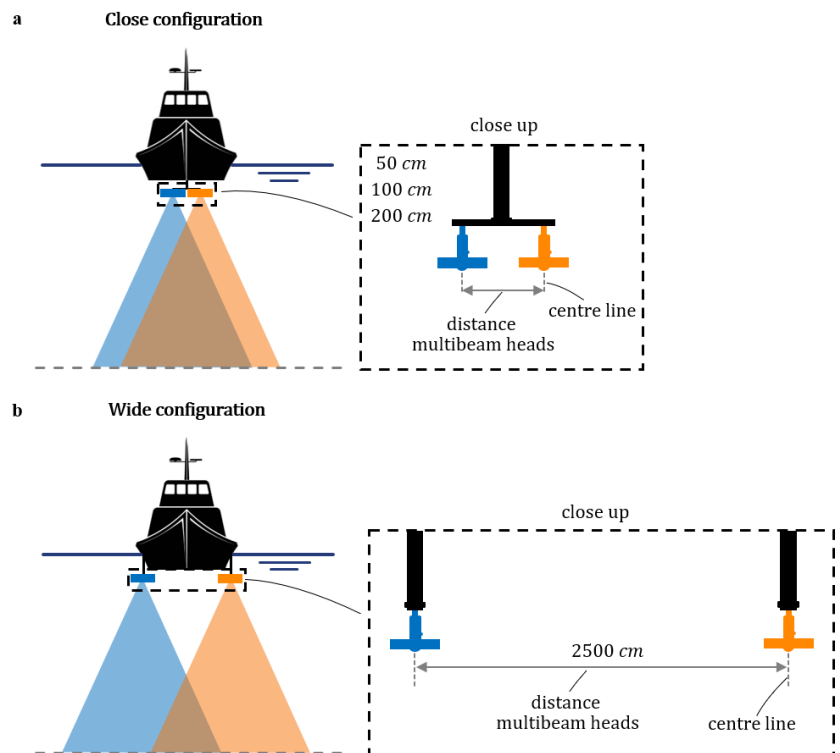

Figure 4.11 Different multibeam dual-head configurations. **a)** close configuration with the heads mounted on the same pole; **b)** wide configuration with the heads mounted on separate poles.

- **Scenario close configuration (4.11a):** two multibeam heads are mounted on the same stiff pole (usually mid-ship). We tested the performance of the algorithm for varying spacings: $50\ cm$, $100\ cm$ and $200\ cm$, where $50\ cm$ is practically the minimum head spacing.
- **Scenario wide configuration (4.11b):** the multibeam heads are mounted on separate poles on the port and starboard side of the vessel. Van Oord's cable-laying or rock installation vessels have an approximate width of $2500\ cm$.

The results of the optimization performance are shown in Figure 4.12b along with examples of soundings for the close and wide configuration in Figure 4.12a. The differences in performance for $50\ cm$, $100\ cm$ and $200\ cm$ were negligibly small. Therefore, only the $100\ cm$ case is shown. Figure 4.12b shows the median (red dot) of 100 inversions and its variability in the estimate. The blue region indicates the vertical tolerance for NL Order A[7], which is $0.32\ m$ at a depth of $40\ m$ (which is already more strict than the IHO standards for hydrographic surveys). When the swath width is set sufficiently wide, the estimate approaches the true value (dashed line) and the error is much smaller than the NL Order A norm e.g. in the order of millimetres. However, we subsequently use the estimate for ROV positioning with USBL, which again comes with the contribution of uncertainties from several sources (total error budget, chapter 1). To this end, we want the estimate to be as accurate as possible e.g. approaching the true value (dashed line).

In general, the estimated harmonic mean sound velocity approaches the true value for increased swath width. This makes sense as the refraction error increases with increasing incident angle. In that case, the depth differences between the overlapping swaths increase. Consequently, the minimum of the objective function is defined more clearly (Figure 4.7), and thus the chance of finding the true value increases. Likewise, widening the spacing between the multibeam heads increases the depth differences between the overlapping swaths. However, the vertical bathymetric uncertainty also increases with increasing swath width (Figure 4.11). Therefore, the wide configuration results in overlap of outer beams that are subject to large uncertainty in the depth estimate. For these

---

[7] NL Order A is the Dutch standard for the maximum allowable TVU (95% CI) for surveys in harbours and shipping lanes (HydroCharting ApS, 2021). Calculation in general form is: $\sqrt{a^2 + (bh)^2}$ with $a = 0.10\ m$, $b = 0.0075$, and h is the water depth.

cases (e.g. 50-70°), the optimization solver has difficulty finding the harmonic mean. In contrast, for the close configuration, the overlap percentage is much larger and the shape of the refracted bathymetry can be extracted more easily despite the uncertainty in the derived depth estimates. Therefore, the close configuration already performs better for smaller swath widths. However, under these circumstances (flat seabed, $40\ m$ depth), almost no differences are found between the two multibeam configurations when setting the swath width to 80°.
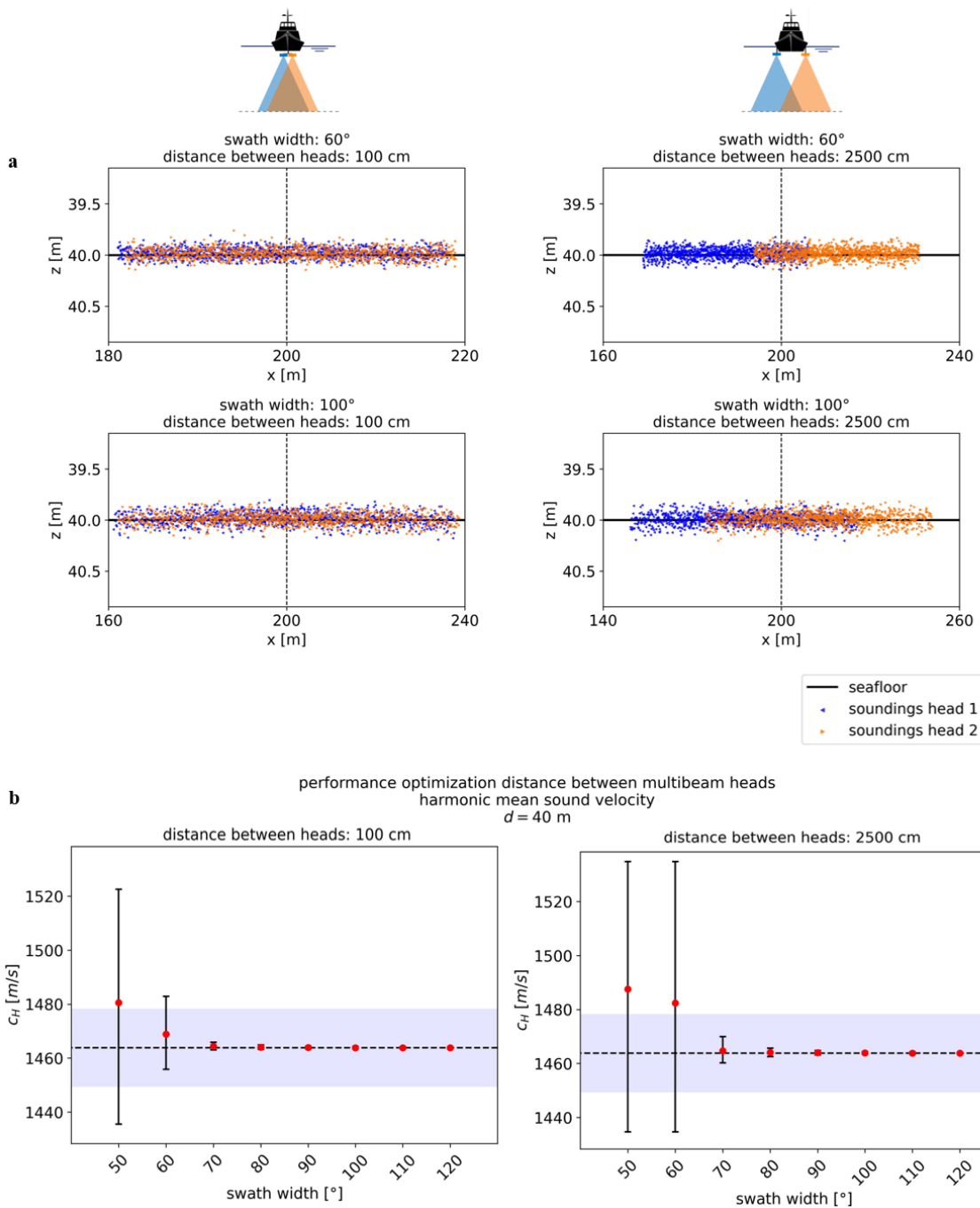
Figure 4.12 a) Soundings (1024) for flat seabed at $40\ m$ depth with head spacing $100\ cm$ (close configuration) and $2500\ cm$ (wide configuration) for swath width of 60° and 100°, respectively. **b)** Statistics of 100 evaluations for the inversion of the harmonic mean sound velocity for the different configurations and different swath widths. Red dot indicates the median of the inverted harmonic means. Black lines are the whiskers indicating the spread of the estimated harmonic means. Black dashed line is the true harmonic mean, derived from the synthetic profile in Figure 4.10a. Blue area indicates the vertical tolerance for NL order A: $0.32\ m$ for a depth of $40\ m$, translated into the harmonic mean sound velocity.

4.3.2 Investigating the effect of angular offset of multibeam dual-heads

In this section, we assess the angular offset of the multibeam dual-heads. The practical motivation for tilting the heads inwards is to increase the sounding density (Pocwiardowski, 2021), as sketched in Figure 4.2b. However, from Figure 4.12a (paragraph 4.3.1), it follows that the close configuration with no angular offset already achieves a doubling of the sounding density in a water depth of $40\ m$. So, in case the heads are tilted inwards, the overlap percentage will reduce for this geometry. The inversion is then based on soundings that are less subject to refraction. Therefore, it is expected that an angular offset will worsen the performance of the inversion method for multibeam heads that are mounted close together.

For the wide configuration, tilting increases the overlap. Therefore, it is expected that an angular offset will improve the performance of the inversion. The question remains whether this improvement is better than the close configuration with no angular offset as presented in paragraph 4.3.1.

In the above described scenarios both heads are tilted inwards. Alternatively, one could think of applying an angular offset to one head only. This set-up might also benefit the performance of the optimization solver as the depth differences are greater due to the significant refraction from soundings originating from the port side head, compared to the ones from the starboard side.
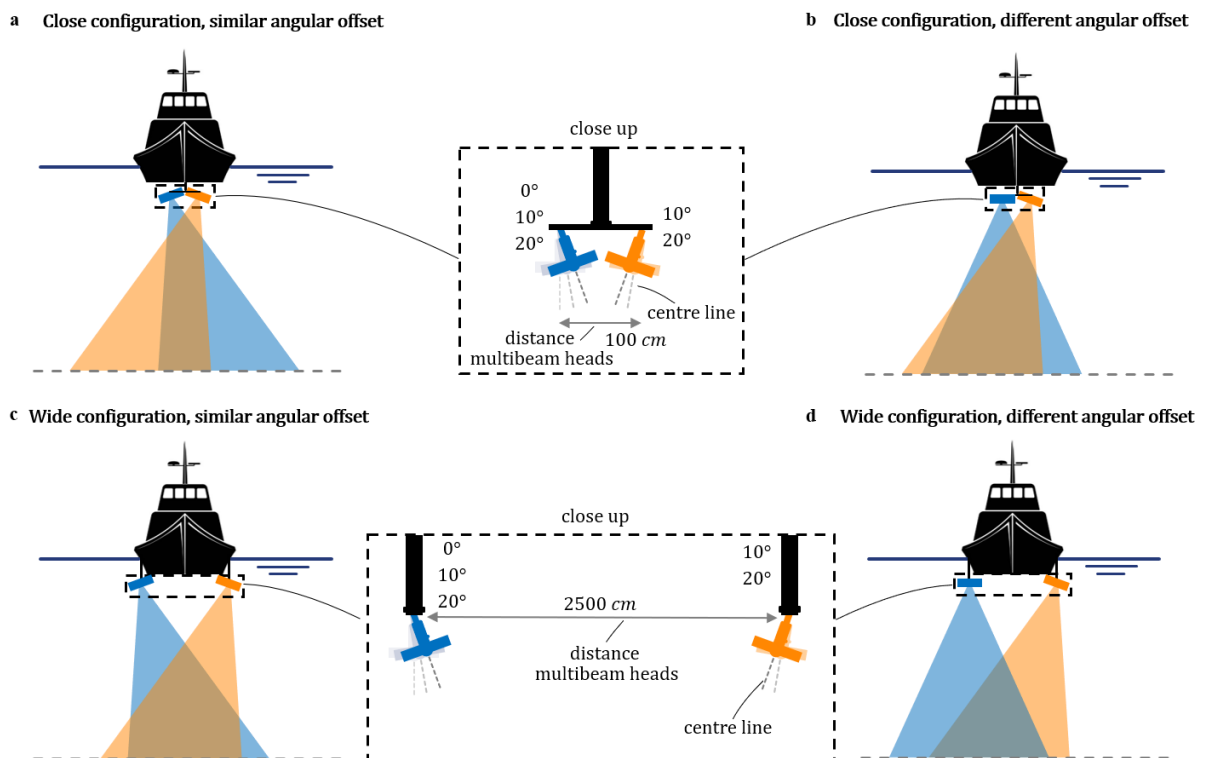

Figure 4.13 Different multibeam dual-head configurations. Close configuration with the heads mounted on the same pole, and **a)** both heads tilted inwards; **b)** one head tilted inwards. Wide configuration with the heads mounted on separate poles, and **c)** both heads tilted inwards; **d)** one head tilted inwards.

Figure 4.13 shows a schematization of four multibeam dual-head configurations. The scenarios are defined as follows and were tested for a flat seabed at $40\ m$ depth:

- **Scenario close configuration and angular offset (4.13a,b):** two multibeam heads mounted on the same stiff pole with spacing $100\ cm$. We tested the performance of the algorithm for two angular offsets: $10°$ and $20°$. In 4.13a, both heads are tilted inwards; in 4.13b, only the port side head is tilted inwards.

- **Scenario wide configuration and angular offset (4.13c,d):** the multibeam heads are mounted on separate poles on the port and starboard side of the vessel with spacing $2500\ cm$. Likewise, we tested for two angular offsets: 10° and 20°. In 4.13c, both heads are tilted inwards; in 4.13d, only the port side head is tilted inwards.

Close configuration and angular offset

A similar analysis – as presented in paragraph 4.3.1 – was performed to investigate the effect of angular offsets for different spacings and a varying swath width of 50-120°. The results of the optimization performance for the close configuration are shown in Figure 4.14b. Figure 4.14a shows examples of soundings obtained from dual-

Figure 4.14 a) Soundings (1024) for flat seabed at $40\ m$ depth with head spacing $100\ cm$ (close configuration) for an angular offset of 10 ° and 20° applied to both heads, and a swath width of 60° and 100°, respectively. **b)** Statistics of 100 evaluations for the inversion of the harmonic mean sound velocity for the different angular offsets and different swath widths. See for more detailed description Figure 4.12b.

heads with different angular offsets. Note that the soundings of the port side (orange coloured) appear now on the left, and the soundings of the starboard side (blue coloured) appear on the right. This is also schematized in Figure 4.13a.

For the scenario with multibeam heads mounted close together, the angular offset reduces the number of soundings in the overlap. In addition, the inversion of the harmonic mean sound velocity is now performed using depth estimates that have small incident angles, and thus their refraction is limited. As expected, tilting the multibeam heads worsens the performance of the inversion method significantly. For comparison: without angular offset, a reliable estimate is provided with a swath width of 70° (Figure 4.12b), whereas inward tilting of 10° and 20° require a swath width of 90° and 110°, respectively (Figure 4.14b). Hence, a close configuration without angular offset requires the smallest swath width for inversion.
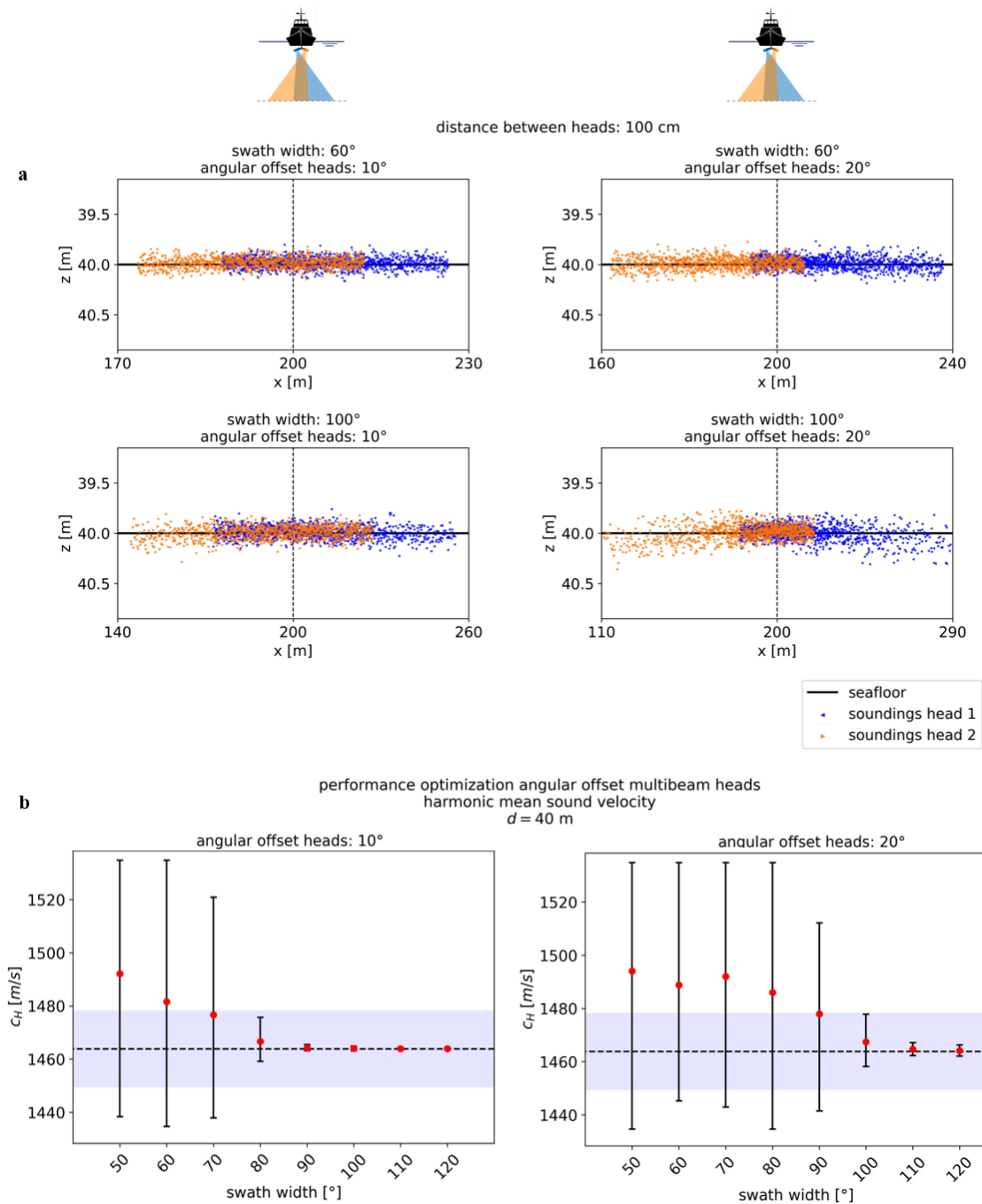

Figure 4.15 a) Soundings (1024) for flat seabed at 40 m depth with head spacing 100 cm (close configuration) for an angular offset of 10 ° and 20° at the port side head only, and a swath width of 60° and 100°, respectively. **b)** Statistics of 100 evaluations for the inversion of the harmonic mean sound velocity for the different angular offsets and different swath widths. See for more detailed description Figure 4.12b.

Figure 4.15b shows the results of the optimization performance when applying the angular offset to one multibeam head only (in this case the port side). Figure 4.15a shows examples of the soundings for this configuration. For the close configuration, the effect of an angular offset applied to one head – while keeping the other head's angular offset at zero – is nihil compared to the scenario where both heads have no angular offset (Figure 4.12b). Although the depth differences in the overlapping area increase, beams that are subject to strong refraction are no longer included in the overlap. However, compared to the case where both heads have an angular offset (Figure 4.14b), applying an angular offset to one head leads to better performance. But, this configuration does not outperform the configuration where both heads have no angular offset at all.
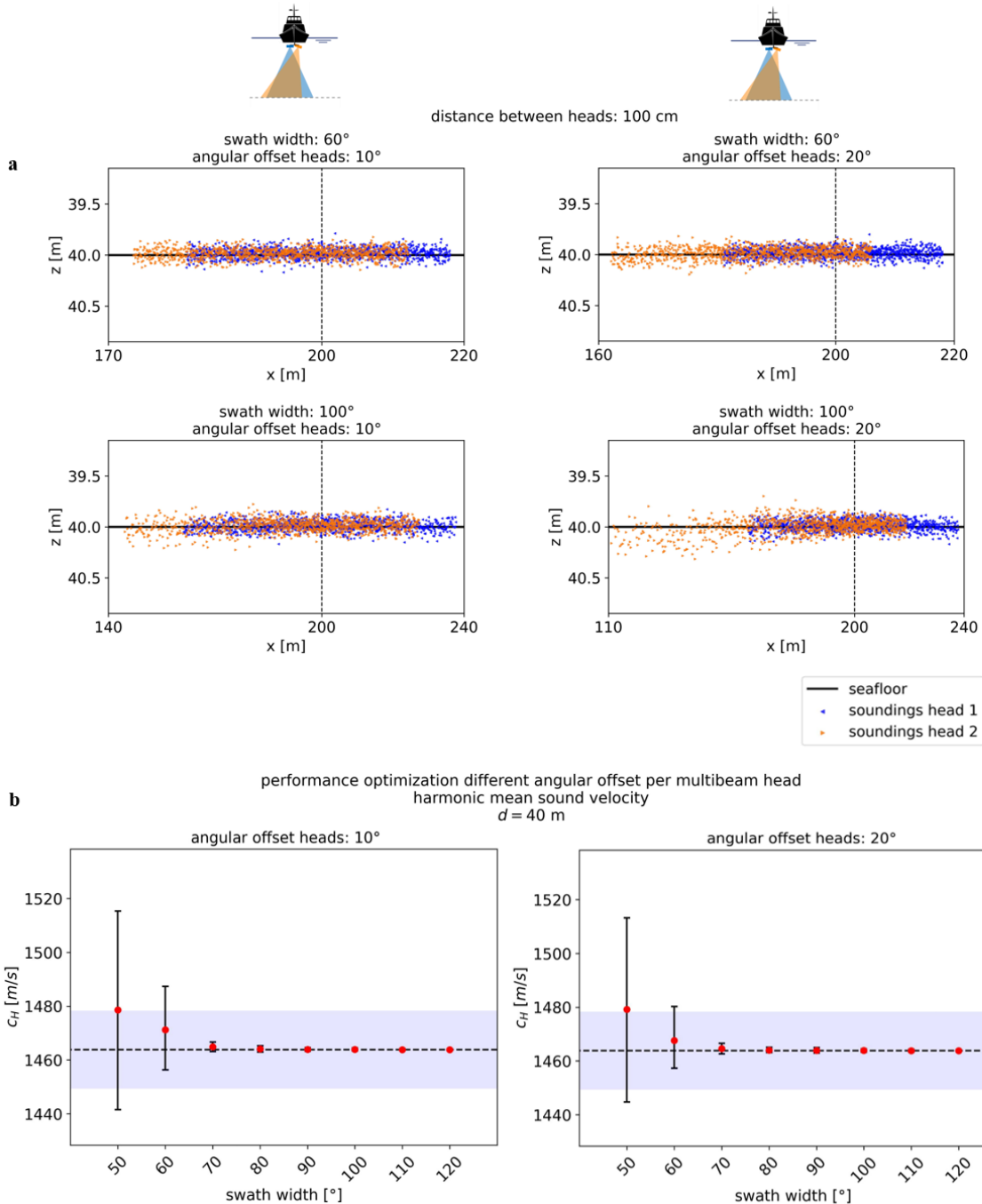
Wide configuration and angular offset

Figure 4.16 a) Soundings (1024) for flat seabed at 40 m depth with head spacing 2500 cm (wide configuration) for an angular offset of 10 ° and 20° applied to both heads, and a swath width of 60° and 100°, respectively. **b)** Statistics of 100 evaluations for the inversion of the harmonic mean sound velocity for the different angular offsets and different swath widths. See for more detailed description Figure 4.12b.

The results of the optimization performance for the wide configuration are shown in Figure 4.16b and the soundings obtained from dual-heads with different angular offsets are given in Figure 4.16a. For the scenario with multibeam heads on the port and starboard side of the vessel and spacing $2500\ cm$, we see an increase in the overlap percentage when tilting the heads inwards. In addition, a relatively small swath width already includes soundings that are subject to significant refraction. This improves the performance of the optimization solver as the objective function is more sensitive to changes in the unknowns (Mohammadloo *et al.*, 2019). Compared to a close configuration (e.g. spacing of $100\ cm$), these soundings fall outside the overlapping area and are therefore not used for inversion. In order to include soundings with significant refraction, the swath width must be increased.
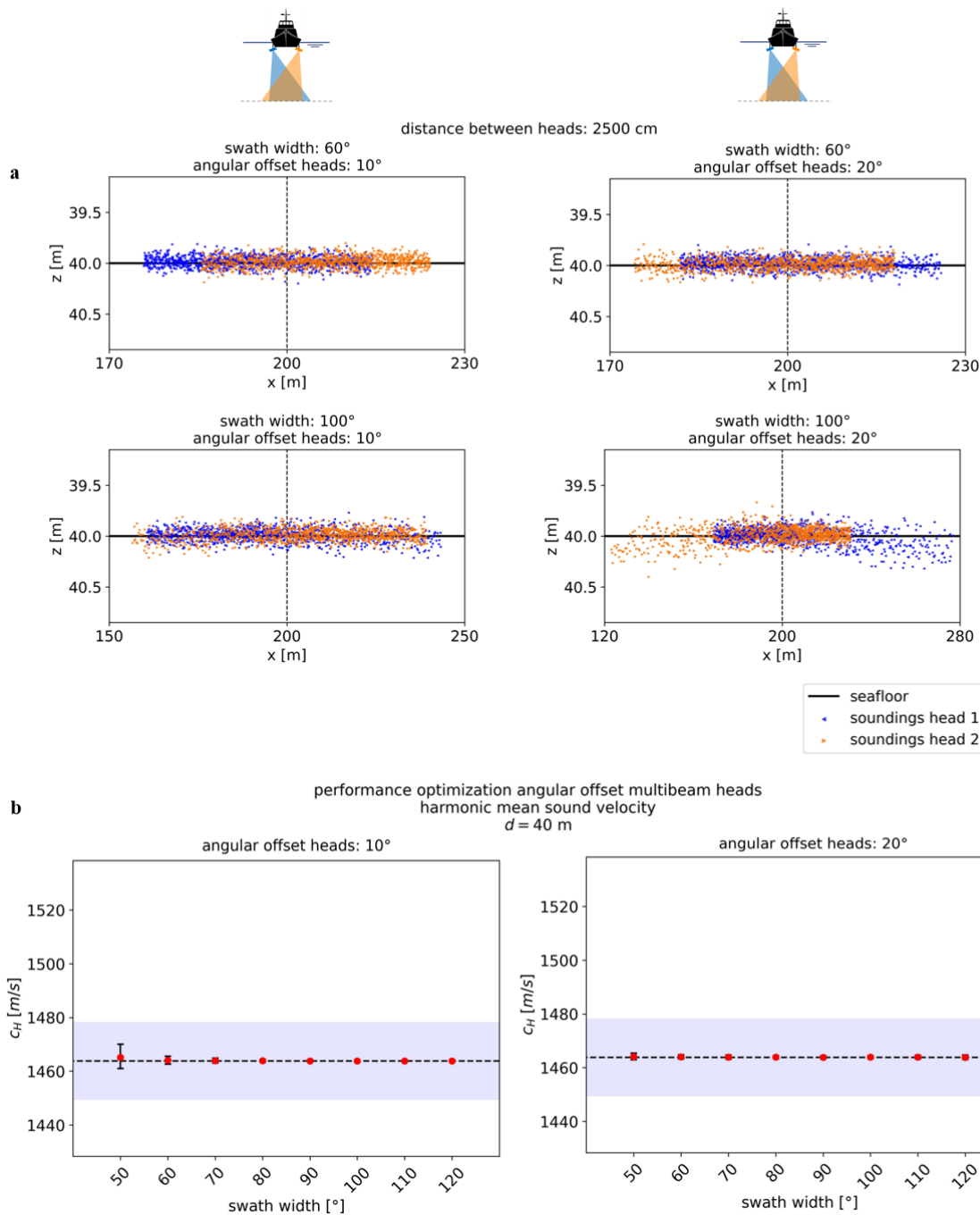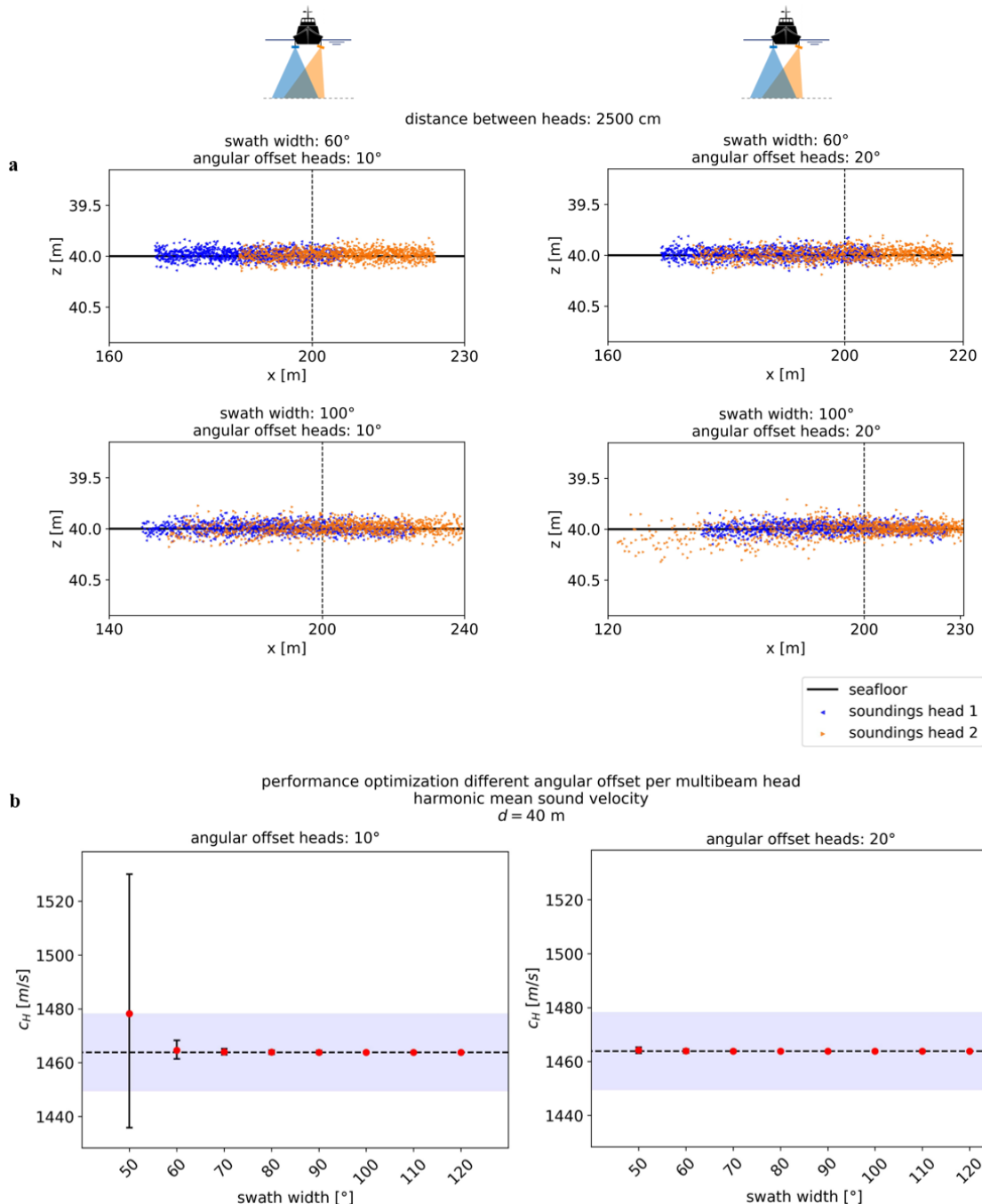

Figure 4.17 a) Soundings (1024) for flat seabed at $40\ m$ depth with head spacing $2500\ cm$ (wide configuration) for an angular offset of $10\,°$ and $20°$ at the port side head only, and a swath width of $60°$ and $100°$, respectively. **b)** Statistics of 100 evaluations for the inversion of the harmonic mean sound velocity for the different angular offsets and different swath widths. See for more detailed description Figure 4.12b.

At last, Figure 4.17b shows the results when applying the angular offset to the port side multibeam head only for the wide configuration, along with soundings obtained from dual-heads with different angular offsets in Figure 4.17a. While tilting one head inwards leads to better performance of the inversion compared to no angular offset (Figure 4.12b), applying the angular offset to both multibeam heads yields better results (Figure 4.16b). However, tilting one head with 20° (Figure 4.17b) instead of two heads with 20° (Figure 4.16b), has the same promising inversion quality.

To conclude this section, the overlap obtained from inward-tilted dual-head multibeam heads in a wide configuration yield a valuable set of depth estimates with significant vertical refraction errors, which in turn benefit the inversion algorithm in the search for the set of harmonic mean sound velocities. Compared to the close configuration, the algorithm is already effective for a small swath width. Figures 4.16b and 4.17b highlight the great performance of the algorithm for this geometry, especially for an offset of 20°. For comparison: without angular offset, a reliable estimate was provided with a swath width of 80° (Figure 4.12b), whereas inward tilting with 10° and 20° require a swath width of 60° and 50°, respectively (Figure 4.16b). The wide configuration with angular offset even outperforms the close configuration without angular offset.

4.3.3 Investigating the effect of water depth and uneven seabed topography

In this section, we assess the effect the water depth and the seabed topography have on the performance of the inversion algorithm. Since the vertical refraction error increases with increasing water depth, the dissimilarities between the overlapping swaths will be greater. Therefore, it is expected that in deeper water a smaller swath width already yields a reliable estimate of the harmonic mean, whereas in shallower water the swath width must be set wider in order to discern the refracted shape. However, with increasing water depth, other sources of uncertainty also propagate and grow (i.e. the TVU increases with depth, Figure 4.10b). Therefore, it is questioned for what swath width the refraction error can be distinguished from other systematic errors in different water depths.

Another factor that deteriorates the performance of the inversion method is an uneven seabed topography. In paragraph 4.2, we briefly discussed the slight mismatch in the estimated harmonic mean as result of an uneven seabed. This error is embedded in the ESVP method since the theory assumes one constant gradient ESVP for a large angular coverage, while in reality the ESVP per beam is slightly different because of the variation in water depth. So, the scaling of the ESVP with an inconsistent water depth complicates the search for the true harmonic mean. Because of this depth scaling, seabed features of a certain magnitude have more of an effect on the estimated harmonic mean in shallow water than in deeper water. Again, it can be questioned what swath width is required to overcome both the uncertainty associated with an uneven seabed topography and the uncertainty from other error sources that degrade the quality of the soundings.

Figure 4.18 shows a schematization of four multibeam dual-head configurations. Based on experiments in previous paragraphs, the two most effective configurations were chosen for this experiment: the close configuration without angular offset (paragraph 4.3.1), and the wide configuration with an angular offset of 20° applied to both heads (paragraph 4.3.2). The scenarios are defined as follows and were tested for a seabed of 20 and 40 m depth. The uneven seabed is a Gaussian random seafloor with a standard deviation of 20 cm.

- **Scenario close configuration and no angular offset (4.18a,b):** two multibeam heads mounted on the same stiff pole with spacing 100 cm without angular offset. We tested the performance of the algorithm for two water depths with a flat and uneven seabed.
- **Scenario wide configuration and angular offset (4.18c,d):** the multibeam heads are mounted on separate poles on the port and starboard side of the vessel with spacing 2500 cm, and the heads titled inwards with a 20° offset. Likewise, we tested for two water depths with a flat and uneven seabed.
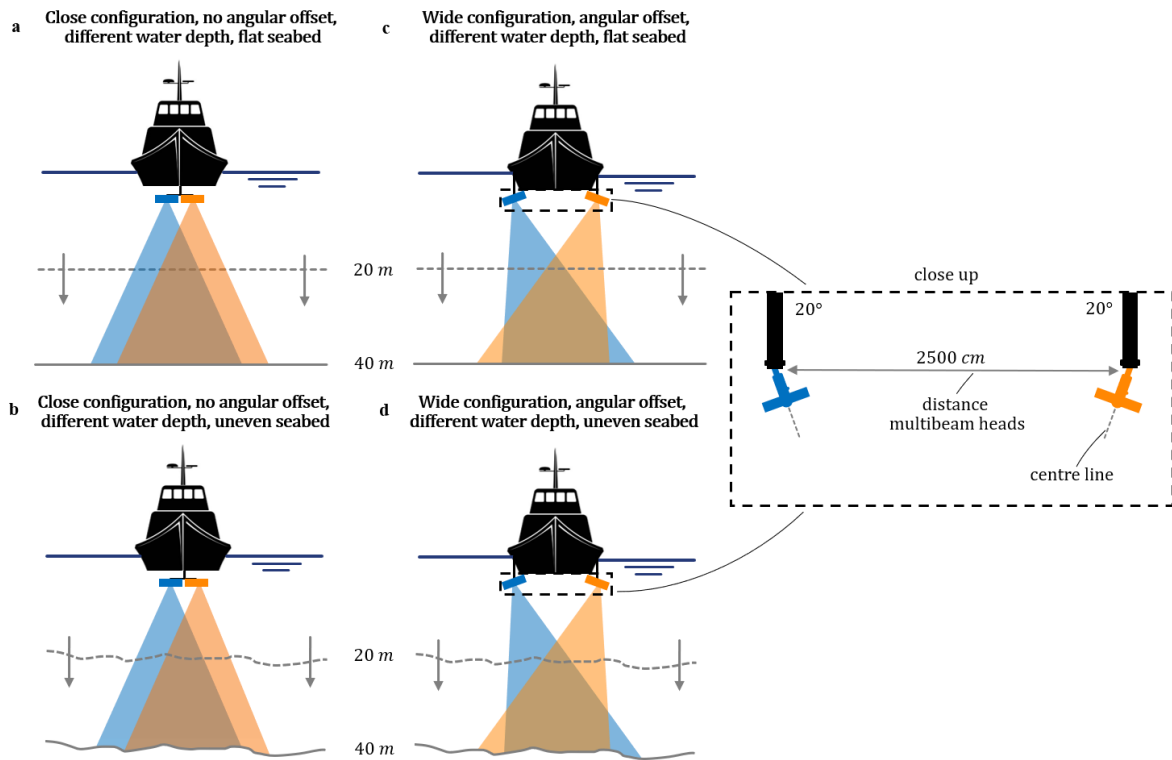
Figure 4.18 Different multibeam dual-head configurations. The close configuration without angular offset, and a **a)** flat seabed; **b)** random seabed. The wide configuration with angular offset, and a **c)** flat seabed; **d)** random seabed.

Close configuration and no angular offset

A similar analysis – as presented in paragraph 4.3.1 – was performed to investigate the effect of different water depths and seabed topographies when varying the swath width from 50-120°. The results for the close configuration without angular offset are shown in Figure 4.19b. Figure 4.19a shows examples of the soundings at the seafloor.

As expected, a water depth of $40\ m$ requires – compared to a water depth of $20\ m$ – a smaller swath width to accurately estimate the harmonic mean. This is because refraction errors grow with increasing water depth, therewith causing the objective function to be more sensitive to changes in the SVP. In other words, the gradients of the energy field are much steeper which in turn enhances the steering of the simplex to the minimum. Despite the larger uncertainty from other contributing errors in deeper water (i.e. increased TVU), the inversion algorithm is still able to retrieve the harmonic mean.

When redoing the experiment with an uneven seabed topography, we observe a significant degradation in quality of the estimated harmonic mean, especially for the water depth of $20\ m$. Apparently, the shape of the bathymetry misleads the algorithm in its job to find the minimum. This makes sense, as the objective function is defined such that it minimizes the refraction errors in the overlapping area. For a flat seabed, the theoretical minimum of the energy function has a value of zero. However, for an uneven seabed, the minimum of the energy function is greater than zero. The energy comes from depth differences between soundings, simply because of the existing bathymetric features. In other words, an uneven seabed already 'produces' energy. This bathymetric energy can be more than the energy from refraction. Therefore, bathymetric features cause deformation of the energy field. Consequently, the algorithm is consistently steered in the wrong direction and can get stuck in a minimum that has little to do with refraction. Besides minimizing the depth differences caused by refraction, the algorithm also attempts to minimize the depth differences of bathymetric features that were inherently present.
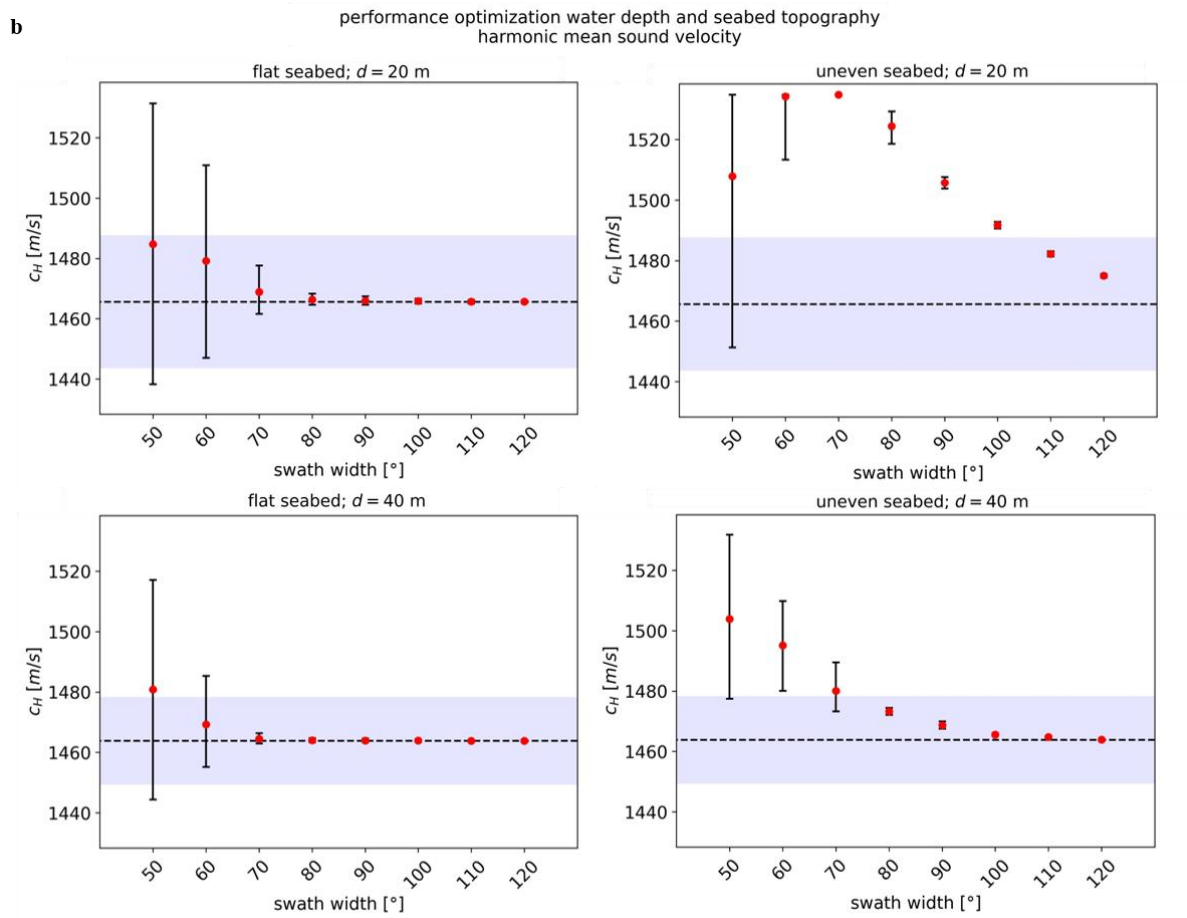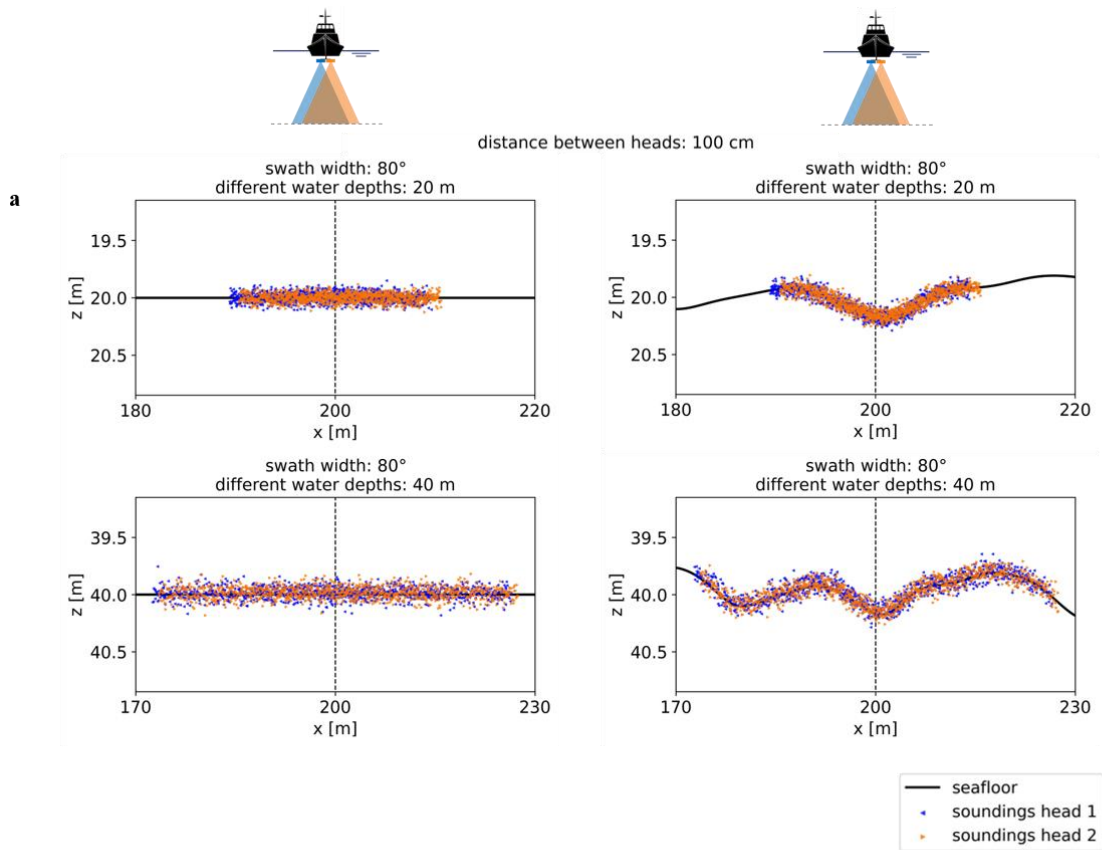
Figure 4.19 a) Soundings (1024) for flat and uneven seabed at 20 and 40 m depth with head spacing 100 cm (close configuration) without angular offset, and a swath width of 80°; **b)** Statistics of 100 evaluations for the inversion of the harmonic mean sound velocity for the different water depths and seabed topographies. See for more detailed description Figure 4.12b.

Wide configuration and angular offset

The results for the wide configuration with inward-tilted multibeam heads are shown in Figure 4.20b along with examples of soundings in Figure 4.20a. We already saw the great performance of the algorithm for this geometry in Figure 4.16b for a water depth of $40\ m$. In shallower water (e.g. $20\ m$), the performance degrades but the degradation is limited to swath widths of 60° and lower. Surprisingly, the introduction of an uneven seabed has minor effect on the estimate. Apparently, this dual-head multibeam set-up creates an overlap of depth estimates that are subject to significant vertical refraction (Figure 4.20a), and can already be created for small swath widths. Quantification of these refraction errors yields an energy field that is superior to the energy contribution from bathymetric features. This enables the algorithm to consistently arrive at the true minimum shaped by variations in the SVP. In other words, the harmonic mean sound velocity is inverted with great accuracy. Subsequently, the estimate can be used for USBL positioning with a similar level of accuracy as presented in the Figure 4.9d (proof-of-concept), with horizontal refraction errors less than $10\ cm$ when the ROV is close to the nadir or close to the seafloor (even for 1 WD away from the transceiver).
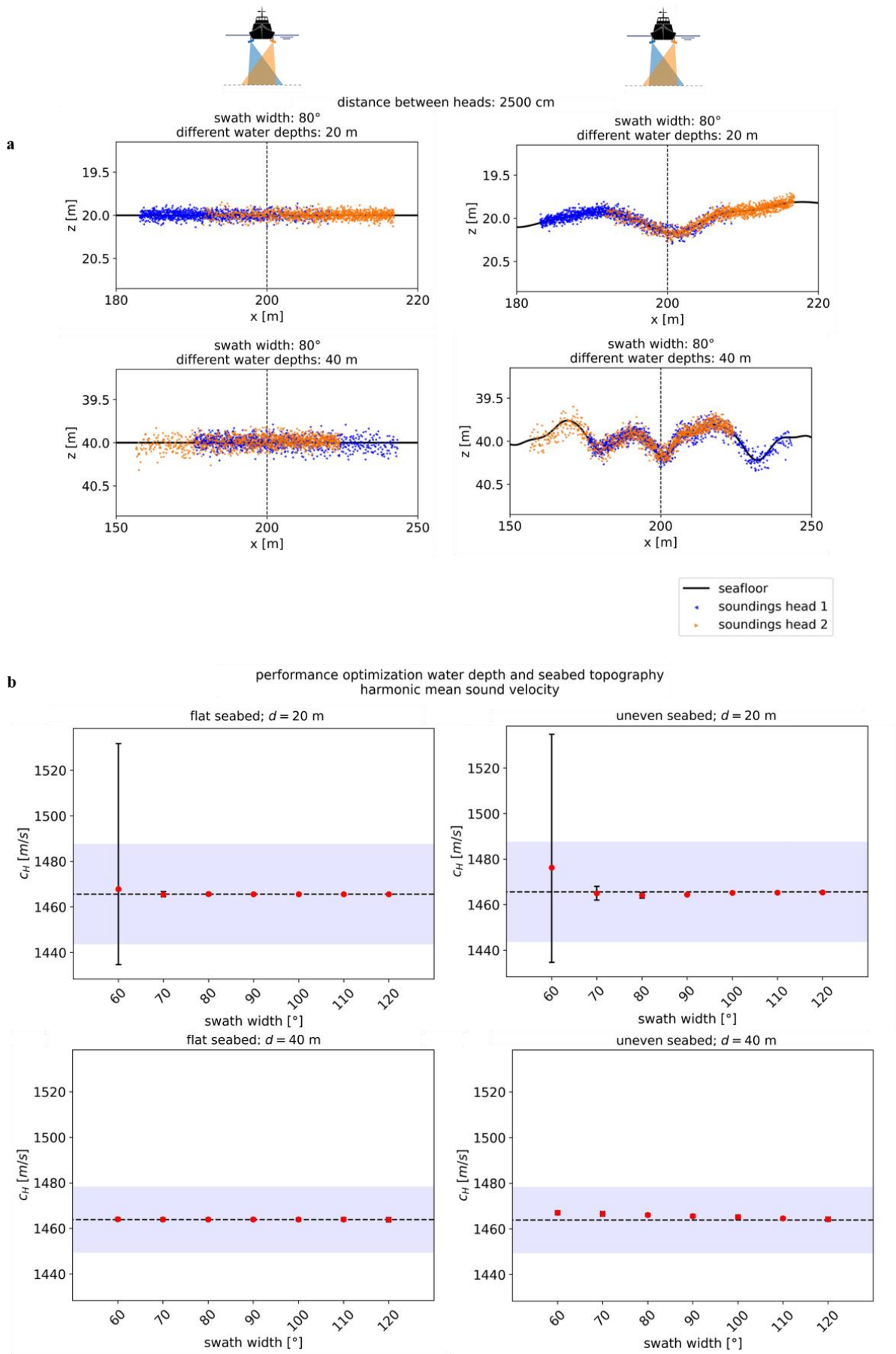
Figure 4.20 a) Soundings (1024) for flat and uneven seabed at 20 and 40 m depth with head spacing 2500 cm (wide configuration) for an angular offset of 20°, and a swath width of 80°; **b)** Statistics of 100 evaluations for the inversion of the harmonic mean sound velocity for the different water depths and seabed topographies. See for more detailed description Figure 4.12b.

5. DISCUSSION

In this chapter, a discussion on the thesis outcome is provided with focus on the mathematical tools, data, and simulations performed that were fundamental the for the working principle and assessment of both inversion methods: HISOM and OMBES. The chapter ends with a general note on the accuracy of USBL positioning systems.

First, a brief note on the methods presented in this thesis in relation to the use of sound velocity information for ROV positioning. For this engineering application, information about the actual SVP is not of interest. Instead, an equivalent SVP is used. This simplified profile does not yield the exact refracted path of the acoustic pulse but it provides the net effect the SVP variation had on the distance travelled within the measured time. Consequently, the ROV's location can be estimated. This approach is different to oceanographic studies that use SVP inversion methods for estimating the stratification in the water column. It requires additional information for the inversion of the actual SVP, for instance the use high-quality historical SVPs measurements at the location of the inversion, as done in Keyzer *et al.* (2021) with the OMBES method.

HISOM

In this thesis, the ocean product GLORYS 12V1 of Copernicus Marine Service was used for the construction of model-generated SVPs. If using data from Copernicus Marine Service, care must be taken when applying the refraction error analysis to locations close to steep bathymetries. It was found that the real error can be 5 times bigger than estimated by the model because of inaccurate depth representation in the model (GLORYS 12V1). In general, the potential use of Copernicus products (or any other oceanographic data source) for the construction of a reliable assessment tool for acoustic positioning depends on the quality of the data source. Since the sound velocity gradients and depth propagation are important ingredients for the refraction error, both SVP gradients and bathymetry must be represented well. It requires further investigation whether other oceanographic data sources can be used. For instance, three-dimensional oceanographic forecasting modelling systems from NOAA (Masetti *et al.*, 2017, 2020). Alternatively, the collection of more SVP observations can validate whether the model-based SVPs provide sufficient knowledge about the SVP. This thesis already showed that for more than 70 locations the model-based SVPs are accurate enough for FPROV positioning at least up to $370\ m$ in the North Sea. In order to scale this method to subsea rock installation project in deeper waters ($\pm1000\ m$). It is advised to compare model-based SVPs with Van Oord's set of observed SVPs in the Norwegian Sea. This collection includes SVPs taken during subsea rock installation projects in waters up to $1200\ m$.

Whereas the OMBES method minimizes the contribution of the sound velocity bias in the error budget of ROV positioning with USBL systems, HISOM methods try to get way with a refraction error that is still within acceptable margins. But what error do we accept? It really depends on the application, and thus, no straightforward answer can be given. In fact, for SRI projects it depends on client requirements, the project type and the design. Also the water depth is of importance because the accuracy of underwater acoustic positioning decreases with increasing water depth. Therefore, it makes sense that the client and contractor agree on a lower accuracy for a SRI project at $800m$ depth (e.g. 40 to 50 cm refraction error contribution) compared to one at $100m$ depth (e.g. 10 to 20 cm refraction error contribution). There is no general design manual that fits the accuracy requirements for all type of offshore projects. However, for the assessment of HISOM methods we must come up with a simple threshold function in correspondence with the survey specialists onboard of SRI vessels (Eq. [3.5], shown in Figure 3.16). Subsequently, the conclusions are based on this threshold which leaves the application of the HISOM method to be ambiguous. Fortunately, the Copernicus Marine Service enables connecting via their application programming interface (API) MOTU Client (appendix B), allowing to easily download marine data to redo the refraction error analysis for a different location with a different tolerance level.

OMBES

The search for a fast and robust optimization solver was a task on its own. Whereas contributions of Mohammadloo *et al.* (2019), Bu *et al.* (2021), and Keyzer *et al.* (2021) use the global optimization method Differential Evolution, we choose to use the local optimization method COBYLA (Powell, 1994). The motivation is that we reduced the dimensionality of the optimization problem. Previous contributions selected the soundings in the overlapping area of multiple survey track lines, and thus selected multiple unknowns that were simultaneously optimized. Our set-up with a dual-head MBES only has two unknowns. However, we first implemented Differential Evolution too, after which we switched to the more intuitive and faster simplex algorithm, namely COBYLA. We can afford to use a local optimization method because within the physical constraints (Eq. [4.9]), there is only one minimum defined. However, as explained by Figure 4.7, reducing the swath width deforms the energy field and shapes an elongated valley. Because of the defined constraints, COBYLA was able to deal with these difficult search jobs. However, it is recommended to further investigate whether optimization algorithms exists that are still able to find the correct minimum despite the very mild gradients. This might lead to more reliable estimates of the harmonic mean for reduced swath widths, and a more flexible configuration of the dual-heads.

We saw that the true harmonic mean sound velocity is difficult to find when introducing pronounced seabed features. We addressed this aspect to the definition of the objective function, which cannot distinguish between depth differences induced by refraction or topography. Bu *et al.* (2021) made a contribution by defining two harmonic mean sound velocities per swath: one for the port side and one for the starboard side. So, in case of a dual-head configuration, we solve for 4 unknowns. This adds some flexibility when using the ESVP theory, which assumes one constant gradient ESVP for a large angular coverage. In reality, the equivalent SVP per beam is slightly different due to the variation in water depth. However, the inversion method exists because of the coherence in the ESVP for the swath. Therefore, it is recommended to investigate whether the inversion method has better performance for additional splitting of the swath into more regions with similar ESVP, ultimately to better deal with uneven seabed topographies. For more information, we refer to Bu *et al.* (2021).

A MBES pulse geometry that was not tested is the geometry of the soundings (the so-called sounding patterns). We now used an equiangular setting, where the soundings are spaced with equal angle. However, it would be interesting to simulate the soundings when spaced at the same distance from one another at the seafloor (equidistant). It increases the number of soundings for the outer beams and might improve the inversion performance of the optimization solver.

The experiments in this thesis were performed by including the bathymetric uncertainty of the soundings based on the hydrography training tool HYDROBIB of Højdal (HydroCharting ApS, 2021). Unfortunately, no documentation was found on the underlying calculations for constituting the total vertical uncertainty. A more transparent option is to derive the uncertainty from AMUST (A Priori Multibeam Uncertainty Simulation Tool). AMUST is a tool developed by the Acoustics Group of the TU Delft in close cooperation with Rijkswaterstaat (Mohammadloo, Snellen and Simons, 2020). The tool is largely based on the model developed by Hare (1995). The software and documentation are online available. It is advised to redo the experiments and see whether results significantly change. The inclusion of bathymetric uncertainties in the estimated soundings also means that an optimum is present between the dual-head MBES configuration and the performance of the optimization solver. For instance, in a water depth of $20\ m$ the angular offset of a multibeam must be larger to create refracted beams in the overlap compared to a water depth of $40\ m$ where the depth propagation of the refraction error already creates significant depth differences. Further increasing the angular offset does not necessarily lead to better inversion results because the bathymetric uncertainty increases with increasing water depth, especially for the outer beams of the swath. These additional uncertainties in the depth estimate deform the energy field quantified by the objective function. This effect is quite similar to the negative effect seabed features have on the performance of the optimization solver. Therefore, it is of interest to work-out the optimal dual-head MBES set-up for a more continuous range of settings, in particular for the relationship between the angular offset and water depth.

General

In this thesis we focussed on the error contribution due to insufficient or incorrect SVP information. However, the positioning error analysis as derived in appendix C.2 revealed other contributing uncertainties associated with USBL positioning, most importantly the angle measurement error $\Delta\theta$. For small incident angles (e.g. $\theta < 6°$), its value is rather constant and depends on depth only. Depending on the signal-to-noise ratio (SNR), the horizontal positioning error can be significant due to the decrease in angular accuracy alone and may be much larger than the refraction error (e.g. order of centremeters to decimetres). For the application of FPROVs, the error is plotted in Figure 5.1. It shows that already for these small offsets (e.g. FPROV positioning), the error can be of the order of meters, in particular in deep water. At a depth of $1000\,m$, the angular error contribution is at least $1\,m$, but can be up to $5\,m$ depending on the quality of the received acoustic signal. Although, we focussed in this thesis on the sound velocity bias, the error from inaccurate angle measurements may contribute more in the total error budget model of USBL positioning.
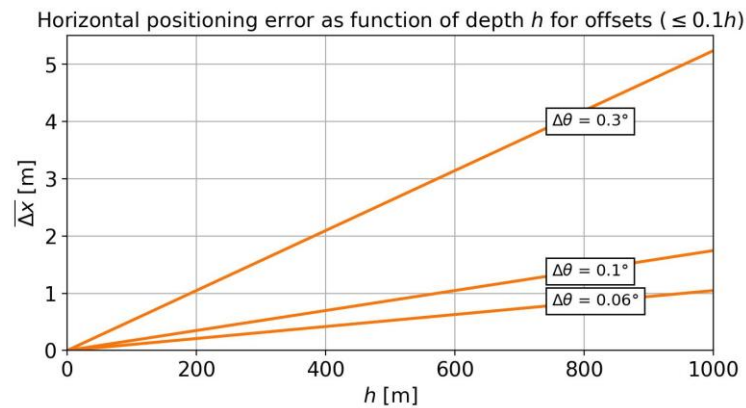

Figure 5.1 Horizontal positioning error as function of depth h for different angle measurement errors $\Delta\theta$, valid for horizontal offsets $\leq 0.1h$ (e.g. FPROVs). For the transducer HiPAP 502 from Kongsberg Maritime, $\Delta\theta = 0.3°$ for SNR = 0, $\Delta\theta = 0.1°$ for SNR = 10, $\Delta\theta = 0.06°$ for SNR = 20 (Kongsberg Maritime, 2016).

For the offshore contractor it means that strong background noise can negatively impact the positioning accuracy, even when the ROV is close to the transceiver's nadir (e.g. FPROV). According to Ross and Kuperman (1989), the strongest noise is typically the propeller/bow thrusters when cavitating. Cavitation involves the formation of bubble clouds, that grow, vibrate and collapse. Consequently, an overall broadband noise spectrum is produced (few Hz to over 100 kHz). Cavitation noise increases with vessel size, load and speed (Ross and Kuperman, 1989). Also, the machinery and engine onboard of the vessel, vibrating into the water through the vessel's hull. Furthermore, turbulence-induced flow past the hull can generate additional narrow-band noise (Urick, 1983). These noise sources lead to a complicated and dynamic noise field (Erbe *et al.*, 2019), thereby decreasing the signal-to-noise ratio. It can negatively influence the angular accuracy when the transducer is determining the direction of the acoustic signal emitted by the ROV's transponder.

In order to increase the angular accuracy, Kongsberg Maritime suggests to use dual mode USBL positioning (i.e. using two transceivers). For example, with SNR = 20, the angle measurement error $\Delta\theta$ reduces from 0.06° to 0.042° in ideal conditions (Kongsberg Maritime, 2016). Another suggestion is to use transponders with strong enough output source level to obtain a high SNR.

6. CONCLUSION

This chapter provides a summary and conclusion to the main findings followed by recommendations for further research.

6.1 Summary and Conclusion

It has been introduced that Van Oord is interested in minimizing the need for laborious SVP measurements required for underwater acoustic positioning of ROVs with USBL. At the same time, Van Oord aims to improve the accuracy of USBL positioning systems as client expectations, technical and contractual requirements in modern offshore operations, are moving forward. The goal of this thesis is to provide suitable methods for the inversion of the SVP that reduce the need for frequent SVP measurements. In addition, tools are provided for the quantification and inclusion of the sound velocity bias in the predictive error budget model for USBL positioning. The error analysis assists Van Oord in decision-making and planning of SVP measurements. This chapter will provide a conclusion to the main and sub questions defined in chapter 1. First, the sub-questions are discussed and then the main question is answered.

What are suitable methods to invert the underwater sound velocity profile and the spatiotemporal variability therein, and how can the estimate be used for ultra-short baseline positioning?

The thesis introduces two inversion methods: **HISOM** (Hull In Situ Ocean Model) (chapter 3) and **OMBES** (Overlapping MultiBeam EchoSounder) (chapter 4). The methods are schematized in Figure 6.1 and are highlighted below:
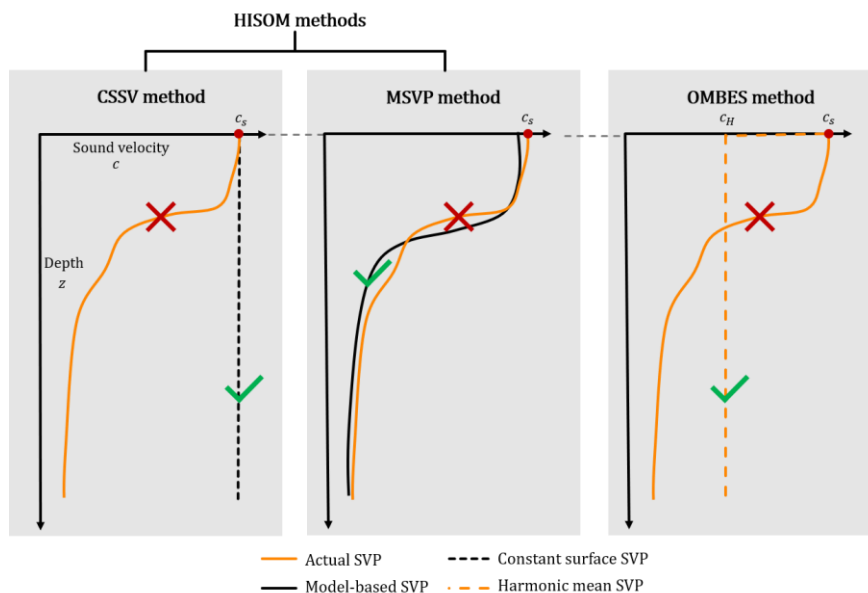
Figure 6.1 Overview of SVP inversion methods presented in this thesis.

1. **HISOM** analyses whether the contractor needs to take an SVP measurement or can rely on substitute (i.e. inverted) SVPs using either: i) a constant profile based on the in situ surface (ISS) sound velocity (c_s in Figure 6.1), or ii). a profile derived from ocean model data in combination with the ISS sound velocity.

   i. **CSSV method** (Constant Surface Sound Velocity). The CSSV method completely neglects the vertical variation of the SVP. Instead, a constant (zero-gradient) SVP is constructed with its value based on the in situ surface (ISS) sound velocity. The applicability of the CSSV method is analyzed for USBL positioning of FPROVs. FPROVs operate at small incident angles for which the use of simplified SVPs is less penalized. First, freely-available oceanographic environmental

model data of the North Sea (from Copernicus Marine Service) is translated into daily-mean SVPs. The variability of these model-based SVPs is quantified using the concept of a simplified SVP with a constant sound velocity gradient. This is the equivalent SVP (ESVP). It enables the derivation of the ESVP ray-tracing algorithm that can calculate the ray's displacements in one step, instead of ray-tracing through each depth layer of constant sound speed. The ESVP ray-tracing algorithm is used to quantify the mismatch between actual SVP and the constant surface SVP in terms of the horizontal refraction-induced positioning error. To assess the applicability of the CSSV method, an user-defined threshold must be defined for the maximum allowable refraction error (e.g. as shown in Figure 3.16).

It was found that, for the North Sea, much of the variability observed in refraction-induced positioning errors can be explained by the seasonal dependence on buoyancy input from heat and freshwater in combination with the bathymetry. In fact, the magnitude of the refraction error depends on the incident angle of the acoustic signal, and the spatiotemporal stratification of the SVP in combination with the depth propagation of the induced error. Temporarily it means that periods exist when the water column is well-mixed in terms of the sound velocity (e.g. winter/spring), with the constant sound velocity gradient being close to zero. Then, the ISS sound velocity suffices for USBL positioning of FPROVs. Spatially it means that the shallow parts of the North Sea (e.g. approximately less than $80\ m$) never experience horizontal refraction errors larger than $0.2\ m$ when sending acoustic signal under small angles ($\theta < 6°$ e.g. with FPROVs). Despite the large sound velocity gradients during summer period in the North Sea, the water depth is often not sufficient for the refraction error to grow problematically and pass the threshold. At those locations, no SVP measurement is necessary. Instead, the contractor can rely on the ISS sound velocity. This saves costly operation time.

The applicability of the CSSV method decreases as the refraction error amplifies with increasing depth in combination with stratification of the SVP. In such case, the use of a constant surface SVP is more penalized. The contractor could either decide to take SVP measurements or use the model-based SVPs.

ii. **MSVP method** (Model-based Sound Velocity Profile). Whereas the CSSV method uses the model-based SVPs to assess where the ISS sound velocity is sufficient for the construction of a constant profile, the MSVP method actually uses the model-based SVPs for USBL positioning (Figure 6.1). A comparison with observed SVPs showed that these model-based SVPs are accurate enough for the positioning of FPROVs at least up to $370\ m$ (e.g. 90% on the North Sea), with estimated refraction errors generally lower than $0.2\ m$.

The MSVP method shows that the contractor can get away with a daily-mean model-based SVP for the positioning of FPROVs for subsea rock installation projects. Especially in deep water, the model is able to accurately estimate the mean SVP because the effect of seasonal stratification – generally present in upper water layers – is averaged out for large depths.

2. **OMBES** uses the overlap in depth measurements between two MBESs to invert the mean sound velocity (c_H in Figure 6.1). Whereas previous studies obtain semi-synchronous overlap in MBES swaths by sailing adjacent track lines (e.g. single-head MBES configuration), we propose to obtain synchronous overlap in one single sailing track using a dual-head MBES configuration. Since the multibeam transducer heads are subject to approximately the same pitch and yaw, the two swaths of a dual-head MBES are aligned. This set-up allows to invert the mean sound velocity near real-time along the track by minimization of the mismatch in depth measurements combined from one ping per head. The inverted mean sound velocity can be used for USBL positioning of ROVs that operate close to the seafloor. Higher up in the water

column, the actual SVP is still needed depending on the sound velocity gradients in the water column. Moreover, close to the transceiver's nadir the error is small because refraction is limited for small incident angles. For this application range, simulations show promising results with horizontal refraction errors smaller than $0.2\ m$, even for large incident angles ($\theta_s \sim 65°$ e.g. approximately 2 water depths horizontally away from the surface vessel). The best performance of the inversion was found when maximizing the distance between the multibeam heads - mounted on the port and starboard side of the vessel (e.g. $25\ m$ difference) – and by inward-tilting one or two heads (e.g. $20°$). For this set-up, the minimum swath width is about $50°$ in $40\ m$ water depth.

The huge benefit of this inversion method is that the sound velocity bias in minimized by providing frequent updates on the change in the harmonic mean sound velocity. This will increase the accuracy of USBL positioning. There is no need to take additional SVP measurements, as long as the ROV stays close to the seafloor where the estimated mean is inverted. Other applications are the need to take SVP when the survey vessel cannot stop to take a manual cast, for instance when performing a bathymetric survey in a busy waterway. In addition, the along-the-track-inverted mean sound velocity can potentially improve the interpolation of the seabed topography when post-processing multibeam bathymetric data.

What is the contribution of the refraction-induced positioning error in the error budget model of underwater acoustic positioning systems?

As introduced, the sound velocity bias is part of the predictive error budget model. Without inversion methods it is difficult to quantify the refraction-induced positioning error because it depends on the dynamically changing marine environment, the depth and incident angle of the ROV during operation. It would require at least two SVP measurements for comparison, while SVP casts are preferably to be minimized. To this end, the sound velocity bias is not included in the error budget model of Van Oord.

The inversion methods allow to estimate the contribution of the refraction-induced positioning error. The CSSV method uses model-based SVPs to quantify the refraction error for the sea area of interest when one completely neglects the SVP. It could be considered as the worst-case scenario. Subsequently, the contractor can set a threshold for the allowable contribution of the sound velocity bias (e.g. $0.2\ m$), and decide upon whether to take an SVP measurement or use the MSVP. Figure 6.2 shows an example with the maximum annual horizontal refraction-induced positioning error for the application of FPROVs.

The reliability of the assessment tool depends on the quality of the ocean model data. With increasing access to reliable ocean forecast model predications, a similar interactive ocean map can be constructed with the horizontal refraction error the offshore contractor can expect in the upcoming days when positioning the FPROV with USBL.
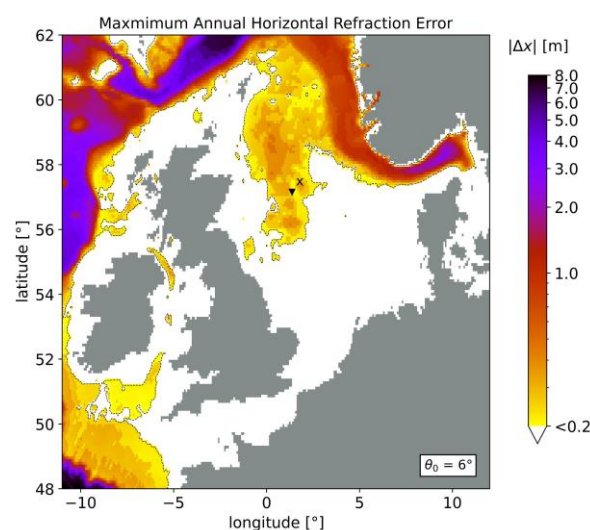
Figure 6.2 Maximum annual horizontal refraction-induced positioning error in the North Sea at the seafloor when using the CSSV method for FPROV acoustic positioning.

OMBES completely minimizes the refraction-induced positioning error by providing near real-time updates on the change in the mean sound velocity on the flight. The refraction errors are in the order of a couple centimeters if the ROV stays close to seafloor or close to the transceiver's nadir. The accuracy of the refraction error mostly depends on the ability to accurately invert the mean sound velocity. It was found that pronounced seabed features significantly reduces the performance of the inversion method. However, maximizing the distance of the

multibeam heads with one or two heads tilted inwards, together with a sufficient wide swath width, allows to overcome the difficulty in the search for the mean sound velocity that represents the actual SVP.

At last, the answer to the main question is provided:

How to minimize the need for underwater sound velocity profile measurements, while improving the accuracy of ultra-short baseline positioning in a dynamically changing marine environment?

Accurate underwater acoustic positioning requires knowledge of the spatiotemporally varying SVP. Using one of the above presented inversion methods allows to estimate the SVP and reduces the need for laborious SVP measurements. The difference between the methods is that HISOM primarily tries to get away with a sound velocity bias that is still acceptable, while OMBES completely minimizes the sound velocity bias. HISOM can potentially be used for deep water ($\pm 1000\,m$) acoustic positioning of FPROVs, while OMBES suites more to ROVs that operate in shallow water ($< 80\,m$) because multibeam data rapidly loses its accuracy and hit count with increasing depth. The advantage of HISOM is the ability to provide spatiotemporal insight in the sound velocity bias by using (forecast) ocean model data with a frequency of about a day, accurate enough for the application of FPROV positioning. For more short-term changes in the SVP, and for ROVs operating at larger incident angles, OMBES provides accurate near real-time updates.

6.2 Recommendations

Based on the discussion and conclusions, several recommendations are made for further research and real-world application of the proposed inversion methods.

HISOM

Despite advancing techniques, the uncertainty from the sound velocity will still heavily affect the accuracy of underwater acoustic positioning. Therefore, it crucial to understand the oceanographic environment. Nowadays, reliable ocean nowcast and forecast model predications can be assessed easily. HISOM proofs its estimating capability and is ready for an automated assessment tool specifically focussed to quantify the sound velocity bias for the application of FPROVs. Currently, there are few effective tools for ocean mapping of these sound velocity biases. Masetti *et al.* (2017, 2020) created a tool to estimate the depth uncertainty when ray-tracing with sonar: the Sea Mappers' Acoustic Ray-Tracing Monitor And Planning (SMARTMAP). It performs a spatial variability analysis of the sound velocity and translates it into uncertainty in the surveyed depth. Likewise, a tool can be created that uses SVPs from forecast systems and checks whether it is valid to neglect the complexity of the SVP. The result is an interactive ocean map with the horizontal refraction error one can expect when positioning the FPROV in the upcoming days (quite similar to Figures 3.17). This tool can potentially assist the contractor in the operational planning for execution of SRI projects by providing oceanographic conditions at the time on site e.g. when and where can one get away measuring the SVP.

OMBES

Recent contributions of Mohammadloo *et al.* (2019) and Bu *et al.* (2021) already showed the working principle of the OBMES method. In fact, the algorithm was first proposed by the Acoustics Group of TU Delft. Through cooperation with the Quality Positioning Services (QPS) company, the algorithm has been implemented as the *TU Delft Sound Speed Inversion Tool* in QPS Qimera (Mohammadloo *et al.*, 2019). While the focus of these contributions is on correcting MBES bathymetric measurements to obtain accurate underwater topography and yield the harmonic mean sound velocity as by-product, this thesis focusses on the quality of the inverted harmonic

mean for ROV positioning. In addition to a successful proof-of-concept, the OMBES needs a real working example because the overlap is obtained differently (e.g. one survey track with dual-heads) compared to previous case studies (e.g. two survey tracks with single-head). Ideally, this is a specialized survey test where different dual-head configuration are tested under controlled conditions (e.g. sailing the same survey track lines, relatively flat seabed, casting SVPs for validation). Therefore, it is advised to acquire test data with the suggested dual-head set-up (e.g. wide configuration with either one or two heads tilted inwards) for different swath widths, and compare with simulations coded in Python (as done in this thesis). Field work also reveals whether real soundings obtained from the proposed synchronous overlap with a dual-head MBES set-up yields a dataset that can be used for inversion on the flight, given the vessel's motions and their error contributions. Since both multibeams are subject to approximately the same pitch and yaw in our proposed set-up, it is expected that the quality of the soundings in the overlap is improved compared to overlap created by sailing adjacent track lines with a single-head MBES.

Despite the fact that we had a real-life case at our disposal, the bathymetric survey we used was performed such that the hit count was doubled, meaning that the dual-heads were in close configuration with the heads tilted inwards in a water depth of approximately $30\ m$. From the experiments it follows that this set-up does not yield satisfactory inversion results. It has been verified using the *TU Delft Sound Speed Inversion Tool* in QPS Qimera. As expected, the inverted harmonic mean sound velocity was different ($\pm 10\ m/s$) when re-running the inversion tool multiple times. For these shallow depths it has no major consequences for the accuracy in acoustic positioning when the ROV is close to the transceiver's nadir (e.g. horizontal refraction errors of a couple centimetres). However, this also means that QPS Qimera provides different solutions for correcting bathymetric data for this geometry with overlapping multibeam swaths. Therefore, it is of interest to research the suggested set-up, and check with QPS Qimera whether the inversion algorithm return more consistent values for the harmonic mean, and thus better minimizes the refraction errors in bathymetric data.

REFERENCES

de Boer, G.J., Pietrzak, J.D. and Winterwerp, J.C. (2009) "SST observations of upwelling induced by tidal straining in the Rhine ROFI," Continental Shelf Research, 29(1). doi: 10.1016/j.csr.2007.06.011.

Bu, X. et al. (2021) "Improved calibration method for refraction errors in multibeam bathymetries with a wider range of water depths," Applied Ocean Research, 114. doi: 10.1016/j.apor.2021.102778.

Christ, R.D. and Wernli, R.L. (2013) The ROV Manual: A User Guide for Remotely Operated Vehicles: Second Edition, The ROV Manual: A User Guide for Remotely Operated Vehicles: Second Edition.

Clark, E., Webb, B.W. and Ladle, M. (1999) "Microthermal gradients and ecological implications in Dorset rivers," Hydrological Processes, 13(3). doi: 10.1002/(SICI)1099-1085(19990228)13:3<423::AID-HYP747>3.0.CO;2-%23.

Copernicus Marine Service (2022) What is the format of Copernicus Marine products? NetCDF | Copernicus Marine Help Center. Available at: What is the format of Copernicus Marine products? NetCDF | Copernicus Marine Help Center (Accessed: March 29, 2022).

Crawford, T.J. (2017) An experimental study of the spread of buoyant water into a rotating environment (PhD thesis)). doi: 10.17863/CAM.10103.

Drévillon, M., Fernandez, E. and Lellouche, J.M. (2021) Global Ocean Physics Reanalysis Documentation. Available at: Data | Copernicus Marine (Accessed: March 29, 2022).

Erbe, C. et al. (2019) "The Effects of Ship Noise on Marine Mammals—A Review," Frontiers in Marine Science. doi: 10.3389/fmars.2019.00606.

Ferger, W.F. (1931) "Ferger (1931) The Nature and Use of the Harmonic Mean," Journal of the American Statistical Association, 26, pp. 36–40. doi: 10.1080/01621459.1931.10503148.

Geng, X. and Zielinski, A. (1999) "Precise multibeam acoustic bathymetry," Marine Geodesy, 22(3). doi: 10.1080/014904199273434.

Hovem, J.M. (2013) "Ray Trace Modeling of Underwater Sound Propagation," Modeling and Measurement Methods for Acoustic Waves and for Acoustic Microdevices [Preprint]. doi: 10.5772/55935.

HydroCharting ApS (2021) HYDROBIB – HydroCharting ApS. Available at: HYDROBIB – HydroCharting ApS (Accessed: April 29, 2022).

IMCA (2017) International Marine Contractors Association - Guidance on vessel USBL systems for use in offshore survey, positioning and DP operations – IMCA. Available at: Guidance on vessel USBL systems for use in offshore survey, positioning and DP operations – IMCA (imca-int.com) (Accessed: March 29, 2022).

Keyzer, L. et al. (2021) "Inversion of sound speed profiles from MBES measurements using Differential Evolution," in 6th Underwater Acoustics Conference and Exhibition. doi: 10.1121/2.0001508.

Kongsberg Maritime (2016) HiPAP® High Precision Acoustic Positioning - Kongsberg Maritime - PDF Catalogs | Documentation | Boating Brochures. Available at: HiPAP® High Precision Acoustic Positioning - Kongsberg Maritime - PDF Catalogs | Documentation | Boating Brochures (nauticexpo.com) (Accessed: March 29, 2022).

Li, J. et al. (2018) "A combined ray tracing method for improving the precision of the USBL positioning system in smart ocean," Sensors (Switzerland), 18(10). doi: 10.3390/s18103586.

Lu, X. et al. (2012) "An improved method for calculating average sound speed in constant gradient sound ray tracing technology," Wuhan Daxue Xuebao (Xinxi Kexue Ban)/Geomatics and Information Science of Wuhan University, 37(5). Available at: An Improved Method for Calculating Average Sound Speed in Constant Gradient Sound Ray Tracing Technology (whu.edu.cn).

Lurton, X. and Augustin, J.M. (2010) "A measurement quality factor for swath bathymetry sounders," IEEE Journal of Oceanic Engineering, 35(4). doi: 10.1109/JOE.2010.2064391.

Masetti, G. et al. (2017) "A Ray-Tracing Uncertainty Estimation Tool for Ocean Mapping," IEEE Access, 6, pp. 2136–2144. doi: 10.1109/ACCESS.2017.2781801.

Masetti, G. et al. (2020) "Applications of the Gulf of Maine Operational Forecast System to Enhance Spatio-Temporal Oceanographic Awareness for Ocean Mapping," Frontiers in Marine Science, 6, p. 804. doi: 10.3389/fmars.2019.00804.

Medwin, H. (1975) "Speed of sound in water: A simple equation for realistic parameters," Journal of the Acoustical Society of America. doi: 10.1121/1.380790.

Mohammadloo, T.H. et al. (2019) "Correcting Multibeam Echosounder Bathymetric Measurements for Errors Induced by Inaccurate Water Column Sound Speeds," IEEE Access, 7. doi: 10.1109/ACCESS.2019.2936170.

Mohammadloo, T.H., Snellen, M. and Simons, D.G. (2020) "Assessing the Performance of the Multi-Beam Echo-Sounder Bathymetric Uncertainty Prediction Model," Applied Sciences 2020, Vol. 10, Page 4671, 10(13), p. 4671. doi: 10.3390/app10134671.

Naankeu Wati, G., Geldof, J.B. and Seube, N. (2016) "Error Budget Analysis for surface and underwater survey system," International Hydrographic Review, pp. 21–46. Available at: https://journals.lib.unb.ca/index.php/ihr/article/view/25812/29960 (Accessed: March 29, 2022).

Nelder, J.A. and Mead, R. (1965) "A Simplex Method for Function Minimization," The Computer Journal, 7(4), pp. 308–313. doi: 10.1093/comjnl/7.4.308.

Peters, R. (2020) Van Oord: North Sea as Breeding Ground for Innovation. Available at: North Sea Energy | TNO (Accessed: March 29, 2022).

Pocwiardowski, P. (2021) Dual-head Application for Multibeam Echosounder | Hydro International. Available at: Dual-head Application for Multibeam Echosounder | Hydro International (hydro-international.com) (Accessed: April 11, 2022).

Powell, M.J.D. (1994) "A Direct Search Optimization Method That Models the Objective and Constraint Functions by Linear Interpolation," Advances in Optimization and Numerical Analysis, pp. 51–67. doi: 10.1007/978-94-015-8330-5_4.

Quazi, A.H. (1981) "An Overview on the Time Delay Estimate in Active and Passive Systems for Target Localization," IEEE Transactions on Acoustics, Speech, and Signal Processing, 29(3). doi: 10.1109/TASSP.1981.1163618.

Ross, D. and Kuperman, W.A. (1989) "Mechanics of Underwater Noise" The Journal of the Acoustical Society of America, 86(4). doi: 10.1121/1.398685.

Schmidt, V. (2012) Calculate the harmonic mean sound speed through a profile - File Exchange - MATLAB Central. Available at: Calculate the harmonic mean sound speed through a profile - File Exchange - MATLAB Central (mathworks.com) (Accessed: April 25, 2022).

Seatools (2022) AUVs & ROVs - Components & Vehicles for Any Purpose. Available at: AUVs & ROVs - Components & Vehicles for Any Purpose (seatools.com) (Accessed: May 29, 2022).

Simpson, J.H. (1993) "Periodic stratification in the Rhine ROFI in the North Sea," Oceanologica Acta, 16(1). Available at: Periodic stratification in the rhine ROFI in the north-sea (ifremer.fr).

Storch, H. von and Zwiers, F.W. (1984) Statistical Analysis in Climate Research, Statistical Analysis in Climate Research.

Sun, D. et al. (2019) "Sound velocity correction based on effective sound velocity for underwater acoustic positioning systems," Applied Acoustics, 151. doi: 10.1016/j.apacoust.2019.02.027.

Talib, K.H. et al. (2011) "Determination of speed of sound using empirical equations and SVP," in Proceedings - 2011 IEEE 7th International Colloquium on Signal Processing and Its Applications, CSPA 2011. doi: 10.1109/CSPA.2011.5759882.

Tong, J. et al. (2019) "An ultra-short baseline positioning model based on rotating array & reusing elements and its error analysis," Sensors (Switzerland), 19(20). doi: 10.3390/s19204373.

le Traon, P.Y. et al. (2019) "From observation to information and users: The Copernicus Marine Service Perspective," Frontiers in Marine Science. doi: 10.3389/fmars.2019.00234.

Urick, R.J. (1983) "Principles of underwater sound. 3rd Edition."

Valeport Limited (2020) miniSVS - Sound Velocity Sensor. Available at: MINISVS-Datasheet-April-2020.pdf (valeport.co.uk) (Accessed: March 29, 2022).

Wang, Y. et al. (2018) "Research of ultrashort baseline positioning method based on depth information," in Proceedings of the 2017 IEEE 2nd Information Technology, Networking, Electronic and Automation Control Conference, ITNEC 2017. doi: 10.1109/ITNEC.2017.8284770.

Xin, M. et al. (2018) "A TOA/AOA Underwater Acoustic Positioning System Based on the Equivalent Sound Speed," Journal of Navigation, 71(6). doi: 10.1017/S037346331800036X.

Zhang, B., Xu, T. and Gao, R. (2018) "Research on acoustic velocity correction algorithm in underwater acoustic positioning," in Lecture Notes in Electrical Engineering. doi: 10.1007/978-981-13-0029-5_72.

Zhang, T. et al. (2022) "Fast and Accurate Underwater Acoustic Horizontal Ranging Algorithm for an Arbitrary Sound-Speed Profile in the Deep Sea," IEEE Internet of Things Journal, 9(1). doi: 10.1109/JIOT.2021.3085331.

Zwolak, K. et al. (2021) "Automatic Identification of Internal Wave Characteristics Affecting Bathymetric Measurement Based on Multibeam Echosounder Water Column Data Analysis," Energies 2021, Vol. 14, Page 4774, 14(16), p. 4774. doi:10.3390/en14164774.

APPENDICES

A.1 Derivation of Displacements and Propagation Time for Equal Gradient Ray-Tracing Algorithm
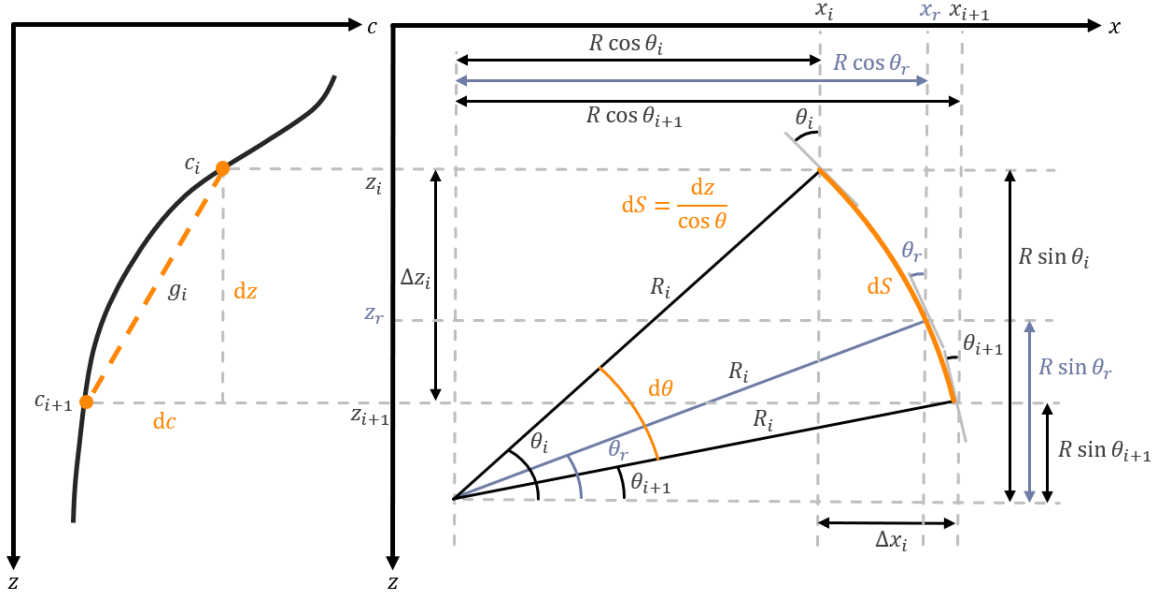
Figure A.1 Schematization of Equal Gradient ray-tracing method

From Figure A.1 it follows that $dz = R\cos\theta\,d\theta$. The vertical displacement $\Delta z\,[m]$ per depth layer i is then written as (Lu *et al.*, 2012; Xin *et al.*, 2018):

$$\Delta z_i = \int_{z_i}^{z_{i+1}} dz = R_i \int_{\theta_i}^{\theta_{i+1}} \cos\theta\,d\theta = R_i[\sin\theta]_{\theta_i}^{\theta_{i+1}} = R_i(\sin\theta_{i+1} - \sin\theta_i) \qquad \text{A.1}$$

Likewise, Figure A.1 shows that $dx = R\sin\theta\,d\theta$. The horizontal displacement $\Delta x\,[m]$ per depth layer i is (Lu, et al., 2012; Xin, et al., 2018):

$$\Delta x_i = \int_{x_i}^{x_{i+1}} dx = R_i \int_{\theta_i}^{\theta_{i+1}} \sin\theta\,d\theta = R_i[-\cos\theta]_{\theta_i}^{\theta_{i+1}} = R_i(\cos\theta_i - \cos\theta_{i+1}) \qquad \text{A.2}$$

The propagation time $\Delta t\,[s]$ per depth layer i can be obtained by substitution of Eq. [A.2]: $c_{i+1}(z) = c_i(z) + g_i\Delta z_i$ in the integral (Lu *et al.*, 2012):

$$t_i = \int_{z_i}^{z_{i+1}} \frac{dz}{c_{i+1}(z)} = \int_{z_i}^{z_{i+1}} \frac{dz}{c_i(z) + g_i\Delta z_i} = \int_{z_i}^{z_{i+1}} \frac{dz}{c_i(z) + g_i dz} = \frac{1}{g_i}\int_{z_i}^{z_{i+1}} \frac{dz}{c_i(z)} = \frac{1}{g_i}[\ln c(z)]_{z_i}^{z_{i+1}} \qquad \text{A.3}$$

$$= \frac{1}{g_i}\ln\left(\frac{c_{i+1}}{c_i}\right)$$

The total propagation time t [s] is defined as the time it takes for the pulse to pass through the water column i.e. half of the two-way travel time:

$$t = \sum_{i=1}^{N} t_i = \sum_{i=1}^{N} \frac{1}{g_i} \ln\left(\frac{c_{i+1}}{c_i}\right)$$

A.4

The average sound velocity with which the pulse travels the distance $z - z_s$ can be obtained using the total propagation time t. In this case, the harmonic mean sound velocity is the average sound velocity required to travel the distance $z - z_s$ within the total propagation time t (Lu et al., 2012):

$$c_H = (z - z_s)t^{-1} = (z - z_s)\sum_{i=1}^{N}\left(\frac{1}{g_i}\ln\left(\frac{c_{i+1}}{c_i}\right)\right)^{-1}$$

A.5

Using this expression, the propagation time in Eq. [A.3] can be written in terms of the harmonic sound velocity c_{H_i} per depth layer i and the arc length in Eq. [2.5] as: $\Delta S_i = R_i(\theta_{i+1} - \theta_i)$, yielding:

$$c_{H_i} = (z_{i+1} - z_i)t_i^{-1} = (z_{i+1} - z_i)\left(\frac{1}{g_i}\ln\left(\frac{c_{i+1}}{c_i}\right)\right)^{-1} = g_i\Delta z_i\left(\ln\left(\frac{c_{i+1}}{c_i}\right)\right)^{-1}$$

A.6

$$t_i = \frac{\Delta S_i}{c_{H_i}} = \frac{R_i(\theta_{i+1} - \theta_i)}{g_i\Delta z_i}\ln\left(\frac{\sin\theta_{i+1}}{\sin\theta_i}\right)$$

A.7

Rewriting Eq. [A.7] in terms of θ only using the expression for the vertical displacement Eq. [A.1], e.g. $\Delta z_i = R_i(\sin\theta_{i+1} - \sin\theta_i)$:

$$t_i = \frac{R_i(\theta_{i+1} - \theta_i)}{g_i\Delta z_i}\ln\left(\frac{\sin\theta_{i+1}}{\sin\theta_i}\right) = \frac{\theta_{i+1} - \theta_i}{g_i(\sin\theta_{i+1} - \sin\theta_i)}\ln\left(\frac{\sin\theta_{i+1}}{\sin\theta_i}\right)$$

A.8

Summarizing, the expressions derived provide an estimate for the vertical displacement Eq. [A.1], horizontal displacement Eq. [A.2], and the propagation time Eq. [A.8] per depth layer i.

$$\begin{cases} \Delta z_i = R_i(\sin\theta_{i+1} - \sin\theta_i) \\ \\ \Delta x_i = R_i(\cos\theta_i - \cos\theta_{i+1}) \\ \\ t_i = \frac{\theta_{i+1} - \theta_i}{g_i(\sin\theta_{i+1} - \sin\theta_i)}\ln\left(\frac{\sin\theta_{i+1}}{\sin\theta_i}\right) \end{cases}$$

Once the pulse reaches the seafloor at depth layer r (e.g. receiver depth z_r, see Figure A.1, highlighted in blue), the expressions are:

$$\begin{cases} \Delta z_r = R_i(\sin\theta_r - \sin\theta_i) \\ \\ \Delta x_r = R_i(\cos\theta_i - \cos\theta_r) \\ \\ t_r = \frac{\theta_r - \theta_i}{g_i(\sin\theta_r - \sin\theta_i)}\ln\left(\frac{\sin\theta_r}{\sin\theta_i}\right) \end{cases}$$

TUDelft

Van Oord
Marine ingenuity

A.2 Proof of Relationship Between Family of Simplified Sound Velocity Profiles

Starting with the integral of the actual sound speed profile, the area S_a is:

$$S_a = \int_{z_s}^{z'_r} c(z)\mathrm{d}z \qquad \text{A.9}$$

The area of the equivalent sound speed profile is (see Figure 2.6), and since the equivalent sound speed profile satisfies Eq. [2.9]: $c_r = c_s + g(z'_r - z_s)$.

$$S_e = \frac{|c_r - c_s|}{2}(z'_r - z_s) = \frac{|g|(z'_r - z_s)^2}{2} \qquad \text{A.10}$$

If the constant gradient g is unknown, it can be calculated by means of the harmonic mean sound velocity c_H using the actual SVP. From Figure 2.6 we infer that, based on equal areas:

$$c_H = \frac{c_s + c_r}{2} \qquad \text{A.11}$$

Rewriting Eq. [A.11]: $c_r = 2c_H - c_s$. Then the constant sound speed gradient is:

$$g = \frac{c_r - c_s}{z'_r - z_s} = \frac{2c_H - 2c_s}{z'_r - z_s} \qquad \text{A.12}$$

At last, the area of the harmonic mean SVP is:

$$S_H = |c_H - c_s|(z'_r - z_s) \qquad \text{A.13}$$

By analysing an actual SVP, one can verify that $S_a = S_e = S_H$ as schematized in Figure 2.6.

A.3 Derivation of Remaining Time for ESVP Ray-Tracing Algorithm

In case of a constant sound speed gradient g, a direct expression can be derived for the time at depth t_{i+1} (Lu *et al.*, 2012):

$$t_{i+1} = \int_{z_i}^{z_{i+1}} \frac{\mathrm{d}z}{c_i(z)\cos\theta} = \int_{\theta_i}^{\theta_{i+1}} \frac{R_i\cos\theta}{c_i(z)\cos\theta}\mathrm{d}\theta = \int_{\theta_i}^{\theta_{i+1}} \frac{\mathrm{d}\theta}{c_i(z)pg_i} = \int_{\theta_i}^{\theta_{i+1}} \frac{c_i(z)}{c_i(z)\sin\theta\, g_i}\mathrm{d}\theta = \frac{1}{g_i}\int_{\theta_i}^{\theta_{i+1}} \frac{\mathrm{d}\theta}{\sin\theta}$$

The reciprocal function of sine is defined as the trigonometric function cosecant: $\csc\theta = \frac{1}{\sin\theta}$. An approach to solve the integral of $\csc\theta$ is to multiply with $\frac{\csc\theta + \cot\theta}{\csc\theta + \cot\theta}$, where $\cot\theta = \frac{1}{\tan\theta}$. This yields numerator to be the opposite (the 'negative') of the derivative of the denominator.

$$t_{i+1} = \frac{1}{g_i}\int_{\theta_i}^{\theta_{i+1}} \csc\theta\, \mathrm{d}\theta = \frac{1}{g_i}\int_{\theta_i}^{\theta_{i+1}} \csc\theta\frac{\csc\theta + \cot\theta}{\csc\theta + \cot\theta}\mathrm{d}\theta = \frac{1}{g_i}\int_{\theta_i}^{\theta_{i+1}} \frac{\csc^2\theta + \csc\theta\cot\theta}{\csc\theta + \cot\theta}\mathrm{d}\theta$$

TUDelft

Van Oord
Marine ingenuity

Now, the chain rule can be applied to solve the integral:

Set $U = \csc\theta + \cot\theta$. To derive its derivative, the expression is split into two parts.

1. Starting off with the derivative of $\csc\theta$:

    Set $y_1 = \csc\theta = \sin^{-1}\theta$;

    Set $u_1 = \sin\theta$, then $y_1 = u_1^{-1}$;

    $\frac{du_1}{d\theta} = \cos\theta$ and $\frac{dy_1}{du_1} = -u_1^{-2}$;

    Thus:

    $$\frac{dy_1}{d\theta} = \frac{dy_1}{du_1}\frac{du_1}{d\theta} = -u_1^{-2}\cos\theta = -\frac{\cos\theta}{\sin^2\theta} = -\frac{\cos\theta}{\sin\theta}\frac{1}{\sin\theta} = -\cot\theta\csc\theta$$

2. The second part involves taking the derivative of $\cot\theta$:

    Set $y_2 = \cot\theta = \tan^{-1}\theta$;

    Set $u_2 = \tan\theta$, then $y_2 = u_2^{-1}$;

    $\frac{du_2}{d\theta} = \cos^{-2}\theta$ and $\frac{dy_2}{du_2} = -u_2^{-2}$;

    Thus:

    $$\frac{dy_2}{d\theta} = \frac{dy_2}{du_2}\frac{du_2}{d\theta} = -u_2^{-2}\cos^{-2}\theta = -\frac{1}{\tan^2\theta}\frac{1}{\cos^2\theta} = -\cot\theta\sec^2\theta = -\csc^2\theta$$

So, the derivative of $U = \csc\theta + \cot\theta$ is $dU = -\csc^2\theta - \cot\theta\csc\theta$. Substitution yields:

$$t_{i+1} = \frac{1}{g_i}\int_{\theta_i}^{\theta_{i+1}}\frac{\csc^2\theta + \csc\theta\cot\theta}{\csc\theta + \cot\theta}d\theta = \frac{1}{g_i}\int_{\theta_i}^{\theta_{i+1}} -\frac{dU}{U} = \frac{1}{g_i}[-\ln U]_{\theta_i}^{\theta_{i+1}} = \frac{1}{g_i}[-\ln|\csc\theta + \cot\theta|]_{\theta_i}^{\theta_{i+1}}$$

So, the antiderivative is minus the natural logarithm of the denominator. Using the tangent half-angle formula, the entire angle of the two trigonometric functions can be written in terms of tangent. The tangent half-angle formula reads: $\tan\pm\frac{1}{2}\theta = \pm(\csc\theta - \cot\theta)$. Substitution leaves:

$$t_{i+1} = \frac{1}{g_i}[-\ln|\csc\theta + \cot\theta|]_{\theta_i}^{\theta_{i+1}} = \frac{1}{g_i}\left[\ln\left|\tan\left(\frac{\theta}{2}\right)\right|\right]_{\theta_i}^{\theta_{i+1}} = \frac{1}{g_i}\ln\left(\frac{\tan(\theta_{i+1}/2)}{\tan(\theta_i/2)}\right) \qquad \text{A.14}$$

Using Snell's law $\theta_{i+1} = \arcsin\left(\frac{c_{i+1}}{c_i}\sin\theta_i\right)$, Eq. [A.14] can be rewritten as:

$$t_{i+1} = \frac{1}{g_i}\ln\left[\frac{\tan\left(\arcsin\left(\frac{c_{i+1}}{c_i}\sin\theta_i\right)/2\right)}{\tan(\theta_i/2)}\right] \qquad \text{A.15}$$

In Eq. [A.15], the ratio $\frac{c_{i+1}}{c_i}$ is rather constant and close to 1. The ratio depends on the value of the sound velocity gradient g, the value of sound velocity, and the thickness of the layers i.

$\frac{c_{i+1}}{c_i} \approx 1$ implies that the ratio $\frac{\tan\left(\arcsin\left(\frac{c_{i+1}}{c_i}\sin\theta_i\right)/2\right)}{\tan(\theta_i/2)}$ is also rather constant and close to 1, i.e. approximately equal but not equal to 1 because the sound velocity profile has a gradient g. The ratio as function of the incident angle

θ_i is plotted in Figure A.2b for an SVP with a constant sound velocity gradient $g = -0.2\ s^{-1}$ (Figure A.2a). The effect on the propagation time is given in Figure A.2c. Only for large incident angles the argument of $\ln(x)$ in Eq. [A.15] starts decreasing, therewith the propagation time is increasing. However, the offshore contractor is often working in a small range of cone angles directly under the transceiver.

From the above analysis we can note the following: if the depth layers are sufficiently small and approximately equal, the ESVP ray-tracing algorithm with its constant gradient g (therewith a constant radius R, and thus an almost constant angle change $\Delta\theta_i$ per depth layer i) allow us to approximate the propagation time $t_i \approx t_{i+1}$, so that:

$$t_i \approx t_{i+1} = \frac{1}{g_i} \ln\left(\frac{\tan(\theta_{i+1}/2)}{\tan(\theta_i/2)}\right) \qquad \text{A.16}$$

Consequently, the remaining time t_r can be approximated by:

$$t_r' = \frac{1}{g_i} \ln\left(\frac{\tan(\theta_r/2)}{\tan(\theta_i/2)}\right) \qquad \text{A.17}$$

The annotation " $'$ " denotes that we deal with an approximation. From Eq. [A.17], a set of equations can be derived for the displacement calculation, that does not require an iteration procedure (see paragraph 2.2).
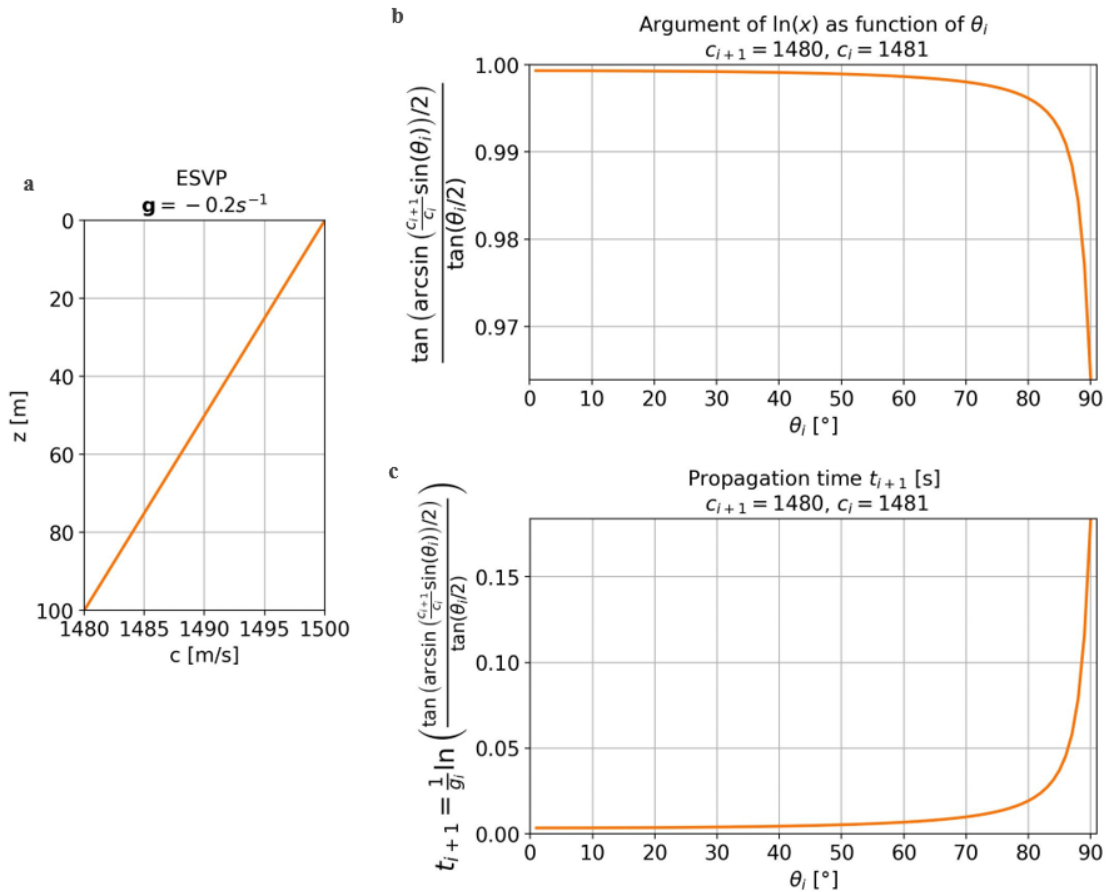
Figure A.2 Function's behaviour of the propagation time Eq. [A.15]. **a)** Equivalent sound velocity profile with constant gradient. **b)** Argument of $\ln(x)$ as function of the incident angle θ_i. **c)** Propagation time t_i [s] as function of the incident angle θ_i.

However, the improvement comes with a cost i.e. the approximation error. Lu *et al.* (2012) performed numerical experiments to address the vertical positioning error introduced by this approximation. They compared the vertical

displacement z_r calculated both iteratively with the Equal Gradient ray-tracing algorithm (paragraph 2.2), and with the direct ESVP ray-tracing algorithm (paragraph 2.4).

The results of the numerical experiment are given in tabular format in Table A.1. It reveals that the vertical positioning error $\epsilon_z = |z_r' - z_r|$ associated with the approximation increases with:

- increasing incident angle;
- increasing sound velocity;
- increasing depth.

Overall, this means that the position error of the multibeam increases towards the edges (up to several decimetres in deeper waters, which cannot be ignored). For small beam angles the error is negligible. One should be aware of the approximation error when using this direct ESVP ray-tracing algorithm. Care must be taken when choosing for instance the beam width for the application of multibeam echo sounding.

θ	$C_{i+1}/$ m$\cdot$s^{-1}	$z_{i+1}/$m									
		10	30	50	70	90	110	130	150	170	190
5°	1 495	0.000 1	0.000 2	0.000 3	0.000 5	0.000 6	0.000 7	0.000 9	0.001 0	0.001 1	0.001 3
	1 505	0.000 3	0.000 8	0.001 3	0.001 8	0.002 4	0.002 9	0.003 4	0.004 0	0.004 5	0.005 0
	1 520	0.000 6	0.001 8	0.003 0	0.004 1	0.005 3	0.006 5	0.007 7	0.008 9	0.010 1	0.011 2
	1 535	0.001 0	0.003 1	0.005 2	0.007 3	0.009 4	0.011 5	0.013 6	0.015 7	0.017 8	0.019 9
	1 550	0.001 6	0.004 9	0.008 1	0.011 4	0.014 6	0.017 9	0.021 1	0.024 4	0.027 7	0.030 9
20°	1 495	0.001 2	0.003 7	0.006 1	0.008 5	0.011 0	0.013 4	0.015 9	0.018 3	0.020 7	0.023 2
	1 505	0.004 9	0.014 6	0.024 3	0.034 0	0.043 8	0.053 5	0.063 2	0.072 9	0.082 7	0.092 4
	1 520	0.010 9	0.032 7	0.054 6	0.076 4	0.098 2	0.120 0	0.141 8	0.163 7	0.185 5	0.207 3
	1 535	0.019 3	0.058 0	0.096 7	0.135 4	0.174 1	0.212 8	0.251 4	0.290 1	0.328 8	0.367 5
	1 550	0.030 1	0.090 4	0.150 7	0.211 0	0.271 2	0.331 5	0.391 8	0.452 1	0.512 4	0.572 6
60°	1 495	0.054 3	0.162 8	0.271 4	0.379 9	0.488 5	0.597 0	0.705 6	0.814 2	0.922 7	1.031 3
	1 505	0.227 0	0.681 0	1.135 0	1.589 0	2.042 9	2.496 9	2.950 9	3.404 9	3.858 9	4.312 9
	1 520	0.535 6	1.606 9	2.678 2	3.749 4	4.820 7	5.892 0	6.963 2	8.034 5	9.105 8	10.177 0
	1 535	1.002 1	3.006 4	5.010 7	7.015 0	9.019 3	11.023 6	13.027 9	15.032 2	17.036 5	19.040 8
	1 550	1.654 5	4.963 6	8.272 7	11.581 7	14.890 8	18.199 9	21.509 0	24.818	28.127 1	31.436 2

Table A.1 Vertical positioning error $\epsilon_z = |z_r' - z_r|$ $[cm]$ between the two ray-tracing algorithms: Equal-Gradient and ESVP (Lu *et al.*, 2012).

B. Data Access via MOTU Client API

The oceanographic dataset is downloaded remotely by creating a connection with the MOTU server via an application programming interface (API). The MOTU Client API enables interaction between a Copernicus Marine user and the MOTU server through a Python script, launched in the open-source Integrated Development Environment (IDE) Jupyter notebook. In order to request the dataset, the following features are exposed:

- Authentication through Central Authentication Service (CAS), a web-based protocol requesting the credentials of the Copernicus Marine user (via a CMEMS account, which is easily created online for free);
- Specification of the geospatial, temporal and variables criteria for the Copernicus Marine Product (e.g. select the GLORYS 12V1 ocean product, the variables of interest, the geographical area, and the time range);
- Execution of the data request, remotely subsetting and downloading of the dataset.

The downloaded file type is a Network Common Data Form (NetCDF), which is a standardized format widely used in engineering and scientific fields (Copernicus Marine Service, 2022). Almost all programming interfaces can read NetCDF file format. Some other advantages of using NetCDF are:

- Self-Describing: NetCDF files include information about the data;
- Scalable: a small subset can efficiently be accessed without walking through the entire dataset;
- Sharable: one writer and multiple readers may simultaneously access the same NetCDF file.

C.1 USBL Principle

The relationship between the acoustic transmitter and transducer elements (e.g. USBL head mounted on a hull unit several meters below the vessel), and the transponder installed on the ROV, can be simplified as shown in Figure C.1, where transducer elements $1, 2, 3$, and 4 are arranged on the x, y-axis, respectively. The transmitter is located in the origin.
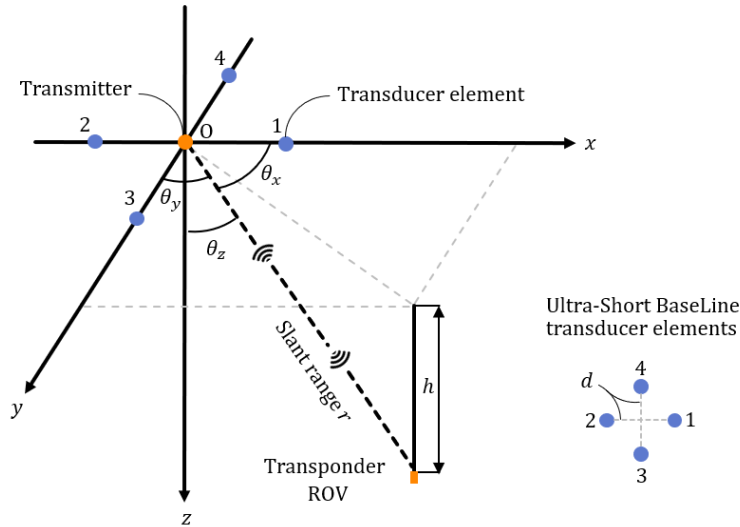

Figure C.1 Schematization of the Ultra-Short BaseLine structure based on four transducer elements. Redrawn from Tong *et al.* (2019).

From Figure C.1 follow the basic equations of the USBL positioning algorithm based on the slant range and azimuth (Wang *et al.*, 2018; Tong *et al.*, 2019):

$$x = r \cos \theta_x \qquad \text{C.1}$$

$$y = r \cos \theta_y \qquad \text{C.2}$$

$$z = \sqrt{r^2 - x^2 - y^2} = r \sqrt{1 - \cos^2 \theta_x - \cos^2 \theta_y} = r \cos \theta_z \qquad \text{C.3}$$

$$r = c_H t \qquad \text{C.4}$$

where (x, y, z) are the coordinates of the USBL positioning target (e.g. transponder of the ROV). $(\theta_x, \theta_y, \theta_z)$ are the angles between the slant range r and the x, y, z-axis, respectively. The slant range r $[m]$ is the (shortest) distance between the center of the acoustic transceiver and target. c_H $[m/s]$ is the harmonic mean sound speed which is calculated from the inserted sound speed profile. The sound velocity profile is measured either by a sound velocity sensor installed on the ROV framework (when launching the ROV to depth), or manually by lowering a sound velocity sensor. t $[s]$ is half of the two-way propagation time of the acoustic signal. The slant range is the product of the harmonic mean sound velocity and the one-way propagation time Eq. [C.4].

The angles $(\theta_x, \theta_y, \theta_z)$ in Figure C.1 are measured by the transceiver, which contains an array of transducer elements. Normally the transceiver head contains three or more transducers separated by fixed distances d $[m]$ (i.e. the baseline length), in the order of centimeters. The direction of the ROV transponder can be calculated using the time-phase difference between transducer elements (Li *et al.*, 2018). A simplified phase-difference model is schematized in Figure C.2. Assuming that the source is located far enough from the receiver, the acoustic waves are plane (Wang, et al., 2017), and the USBL phase-difference is:

$$\varphi_x = \frac{2\pi\tau}{T}$$

C.5

where $\tau \; [s]$ is the time-difference or relative delay between the two transducer elements of the acoustic wave passing. Using the geometry in Figure C.2, one can obtain that the relative delay equals:

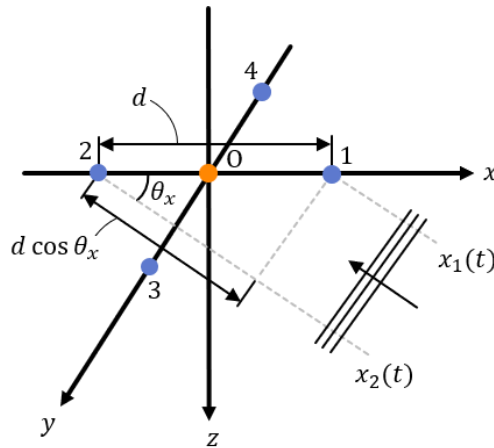$$\tau = \frac{d\cos\theta_x}{c_s}$$

C.6

Figure C.2 Schematization of the phase-difference between two transducer elements. Redrawn from Tong *et al.* (2019).

In Eq. [C.5], $T \; [s]$ is the period of the acoustic signal, which is defined with the wavelength $\lambda \; [m]$ and the center frequency $f \; [Hz]$ of the underwater acoustic signal:

$$T = \frac{1}{f} = \frac{c_s/f}{c_s} = \frac{\lambda}{c_s}$$

C.7

Using Eq. [C.6] and Eq. [C.7], the phase-difference in Eq. [C.5] can be rewritten as:

$$\varphi_x = \frac{2\pi d\cos\theta_x}{\lambda}$$

C.8

Similarly available:

$$\varphi_y = \frac{2\pi d\cos\theta_y}{\lambda}$$

C.9

$$\varphi_z = \frac{2\pi d\cos\theta_z}{\lambda}$$

C.10

From the difference in arrival time of the acoustic signal, the phase-differences (φ_x, φ_y) follow. Therefore, the direction angles (θ_x, θ_y) of the acoustic signal can be obtained by rewriting Eq. [C.8] and Eq. [C.9]:

$$\theta_x = \arccos\left(\frac{\lambda\varphi_x}{2\pi d}\right)$$

C.11

TUDelft

Van Oord
Marine ingenuity

$$\theta_y = \arccos\left(\frac{\lambda \varphi_y}{2\pi d}\right) \qquad\qquad \text{C.12}$$

Substituting Eq. [C.11] and Eq. [C.12] into Eq. [C.1] and Eq. [C.2] yield:

$$x = \frac{r\lambda \varphi_x}{2\pi d} \qquad\qquad \text{C.13}$$

$$y = \frac{r\lambda \varphi_y}{2\pi d} \qquad\qquad \text{C.14}$$

Eq. [C.13], Eq. [C.14] and Eq. [C.3] are the basic formulas of the USBL positioning system. The ROV's position is computed based on these principle equations. Though, the exact value of the ROV's position is impossible to determine, because the dependent variables stem from various sensors and procedures. It is however possible to estimate the uncertainty from these position equations and the measurement uncertainties associated with each sensor measurement. Using a statistical method called the uncertainty propagation law (or root-sum-of-squares), the error budget or total propagated uncertainty (TPU) can be estimated (Naankeu Wati, Geldof and Seube, 2016). The next paragraph shows the derivation of the error budget specifically for the USBL positioning system.

C.2 Positioning Error Analysis

The first derived error budget model is based on the basic range and bearing principle of USBL. The second derived error budget model incorporates depth information from pressure sensors, which often used in underwater acoustic positioning.

C.2.1 Positioning error analysis of slant range and azimuth method

The positioning error equation of the USBL positioning system in the x-axis can be obtained by taking the total derivative of Eq. [C.13] (Wang *et al.*, 2018; Tong *et al.*, 2019) which is the same as considering all partial derivatives simultaneously. Following Wang *et al.* (2018) and Tong *et al.* (2019), the errors are assumed to be independent of each other. Then the root-mean-square error in the x-axis direction is:

$$\overline{\Delta x} = \frac{r\lambda \varphi_x}{2\pi d}\sqrt{2\left(\frac{\Delta c_H}{c_H}\right)^2 + \left(\frac{\Delta t}{t}\right)^2 + \left(\frac{\Delta \varphi_x}{\varphi_x}\right)^2 + \left(\frac{\Delta d}{d}\right)^2} \qquad\qquad \text{C.15}$$

Where Δc_H is the harmonic mean sound speed estimation error, Δt is the time delay measurement error, $\Delta \varphi$ the phase-difference error and Δd is the spacing error between the transducer elements. A complete derivation can be found in appendix C.3.

The relative error is often used to note the positioning accuracy in relation to the slant range r:

$$positioning\ accuracy = \frac{\sigma_x}{r} \qquad\qquad \text{C.16}$$

Substituting Eq. [C.1] and Eq. [C.13] into Eq. [C.17], the positioning accuracy of relative range is:

$$\frac{\overline{\Delta x}}{r} = \cos\theta_x\sqrt{2\left(\frac{\Delta c_H}{c_H}\right)^2 + \left(\frac{\Delta t}{t}\right)^2 + \left(\frac{\Delta \varphi_x}{\varphi_x}\right)^2 + \left(\frac{\Delta d}{d}\right)^2} \qquad\qquad \text{C.17}$$

T U Delft

Van Oord
Marine ingenuity

From Eq. [C.17], it can be seen that the USBL positioning accuracy is inversely proportional to the harmonic mean sound speed estimation error Δc_H, the time delay measurement error Δt, the phase-difference error $\Delta \varphi$, and the spacing error Δd. In addition, one can see that all error terms are related to the angle θ_x. When the ROV is located right below the vessel's transceiver, that means, an angle θ_x close to $90°$, the positioning error is reduced. In other words, the positioning accuracy of the USBL has the best performance in the range of cone angles directly below the transceiver (Wang *et al.*, 2018; Tong *et al.*, 2019).

It is interesting to quantify the relative error factors and see which error terms contribute most to the USBL positioning error. With relative error factors we mean:

The relative harmonic mean sound velocity estimation error factor $\frac{\Delta c_H}{c_H}$

The harmonic mean sound velocity error Δc_H depends on the accuracy of the sound velocity sensor. The sound velocity measurement is made using a single pulse of sound traveling over a known distance, and time-tracking allows to estimate the sound velocity. Technical details on the accuracy are usually provided by the manufacturer. The error may include random noise in the circuit, systematic calibration error, and systematic clock error. If the sound velocity sensor is a Valeport miniSVS (sensor size: $100\ mm$), the maximum error is $\Delta c = 0.017\ m/s$ (Valeport Limited, 2020). For simplicity, the harmonic mean sound velocity is $c_H = 1500\ m/s$.

Evaluating the relative harmonic mean sound velocity estimation error factor: $\sqrt{2 \left(\frac{\Delta c_H}{c_H} \right)^2} = 0.000016$

The relative time delay measurement error factor $\frac{\Delta t}{t}$

Quantification of the time delay measurement error Δt is difficult as it depends on the signal's acoustic properties and the background noise. More in-depth information is given in intermezzo C.1. Tong *et al.* (2019) estimated the time delay measurement error $\Delta t = 1\ ms$ based on performance parameters of current positioning products. For the sake of ease we follow Tong *et al.* (2019). Considering the location environment with a slant range $r = 1000\ m$, using Eq. [C.4] yields the one-way propagation time $t = r/c_H = 0.667\ s$.

Evaluating the relative time delay measurement error factor: $\frac{\Delta t}{t} = 0.0015$

The relative phase-difference error factor $\frac{\Delta \varphi}{\varphi}$

Also, quantification of the phase-difference error $\Delta \varphi$ is complex as it has similar dependence on the signal's acoustic properties and background noise. An interesting reader is referred to intermezzo C.1. Unfortunately, Tong *et al.* (2019) did not elaborate on the phase-difference error term in their positioning error analysis of slant range and azimuth method. Later in the appendix, we come up with a different positioning error analysis method that does not explicitly require quantification of the phase-difference error. It uses an equivalent measure which is the angle measurement error.

For now we leave it open: $\frac{\Delta \varphi_x}{\varphi_x} = \cdots$

The relative spacing error factor $\frac{\Delta d}{d}$

According to Tong *et al.* (2019), the main cause of the spacing error Δd is the measurement error, which means that the baselines are systematically smaller/larger. It has a direct impact on the accuracy of the angle measurement, and thus the USBL positioning calculation. This error is constant in one measurement but can be different between groups of transducer elements. Therefore, prior to using an USBL positioning system in an underwater acoustic environment, the spacing error of the transducer elements must be

calibrated (Tong *et al.*, 2019). Let us assume that the baselines have a length of $d = 25\ mm$ and the spacing error $\Delta d = 0.2\ mm$, therewith following the error factor used in Tong *et al.* (2019).

Evaluating the relative spacing error factor: $\dfrac{\Delta d}{d} = 0.008$

Comparing the relative error factors, it can be seen that the relative spacing error contributes most to the positioning error. However, the scaling is debatable as it depends on the technical specifications of the positioning system and numbers used. Many of those parameters are not available for the public, and are therefore estimated.

What can be concluded is that the error of the sound velocity sensor has negligible effect on the positioning accuracy. For a range of $r = 1000\ m$, an offset from the transceiver no more than 10% of the water depth (see Figure C.3), and a relative error factor of $2\dfrac{\Delta c_H}{c_H} = 0.00002$, the horizontal positioning error of USBL caused by the harmonic mean sound velocity estimation error is:

$$\overline{\Delta x} = r\cos\theta_x \sqrt{2\left(\frac{\Delta c_H}{c_H}\right)^2} = 1000 \cdot \cos(84.29°) \cdot \sqrt{2 \cdot \left(\frac{0.017}{1500}\right)^2} = 0.0016\ m$$

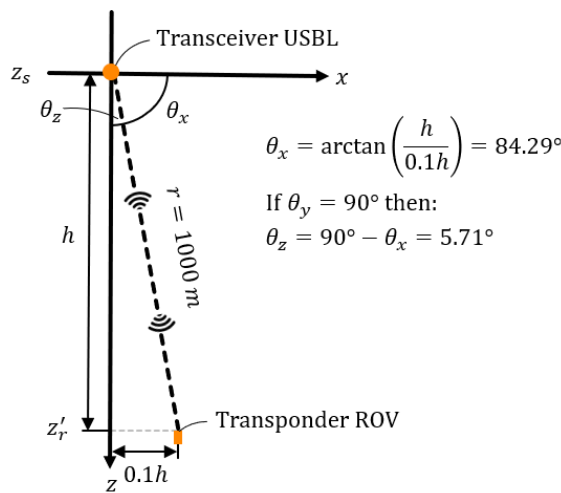**Figure C.3** Schematization of ROV positioning for the case with slant range of $r = 1000\ m$ and offset of $0.1h$.

For comparison, under the same conditions, the element spacing error could bring about a $0.80\ m$ horizontal positioning error! See the calculation below:

$$\overline{\Delta x} = r\cos(\theta_x)\frac{\Delta d}{d} = 1000 \cdot \cos(84.29°) \cdot \frac{0.2}{25} = 0.80\ m$$

The element spacing error can therefore not be neglected in engineering application. Though, the error analysis presented in Wang *et al.* (2017) did neglect the influence of the spacing error, while Tong *et al.* (2019) showed, based on theoretical analysis and simulation experiments, that the spacing error was the main error source of the USBL positioning system. An important sidenote is that Tong *et al.* (2019) did not quantify the phase-difference error for relative comparison.

Since we cannot simply estimate the phase-difference error with this positioning method based on slant range and azimuth, we move to a positioning method based on depth information.

_____

Quantification of these error terms is difficult, since the error terms Δt and $\Delta \varphi$ are functions of the signal-to-noise ratio (SNR), bandwidth, observation time, and center frequency of the acoustic signal (Quazi, 1981) where:

- the SNR ($\text{SNR} = \frac{P_{signal}}{P_{noise}}$) is the ratio of the power of a (meaningful) signal to the power of a (meaningless) background noise, often expressed in decibels. A signal-to-noise ratio higher than 1 indicates more signal than noise.
- the bandwidth B [Hz] refers to the capability of the USBL positioning system to process signals with a range of frequencies.
- the observation time T [s] is the time duration that the USBL positioning system listens to the received signal.
- the center frequency f [Hz] is the central frequency between the lower and upper cut-off frequencies, the boundaries that define the bandwidth.

Both the time delay t and phase-difference φ are estimated by measuring the instant when the acoustic signal arrives at a transducer element. Generally, this is accomplished by matched filtering, which is a process for detecting the (ROV's) transmitted signal that is embedded in noise. Estimating exactly when the signal's peak occurs is uncertain owing to the noise added. This uncertainty is embedded in the error terms Δt and $\Delta \varphi$.

To address the quantification of the error terms, Wang *et al.* (2018) use the Cramér-Rao Lower Bound (CRLB) theory for the time delay estimation and phase-difference estimation. The CRLB gives a lower bound on the standard deviation. It tells us the best we can ever expect to be able to do. Quazi (1981) presented the CRLB of the standard deviation of the time delay estimate σ_t, which can be transformed to the CRLB of the standard deviation of the phase-difference estimate σ_φ (Wang et al., 2018):

$$\Delta t = \sigma_t = \sqrt{\frac{1}{4\pi^2} \frac{1}{\sqrt{\text{SNR}}} \frac{1}{\sqrt{TB}} \frac{1}{f} \frac{1}{\sqrt{1 + B^2/12f^2}}} \qquad \text{I.1}$$

$$\Delta \varphi = \sigma_\varphi = \frac{1}{\sqrt{\text{SNR}}} \frac{1}{\sqrt{TB}} \frac{1}{\sqrt{1 + B^2/12f^2}} \qquad \text{I.2}$$

Based on theoretical analysis from Quazi (1981), some noteworthy results are that:

- the standard deviations σ_t and σ_φ are inversely proportional to the square-root of the SNR. This relation holds for high SNR (SNR $\gg$ 1). Thus, by increasing the SNR (i.e. more signal than noise), the standard deviations decrease with the square-root.
- the standard deviations σ_t and σ_φ are inversely proportional to the square-root of the product of the bandwidth B and observation time T. For instance, by doubling the observation time, the standard deviations decrease with almost 30%.
- the standard deviation σ_t is inversely proportional to the center frequency f. Increasing the signal's frequency leads to a decrease of the standard deviation for the time delay.

_____

C.2.2 Positioning error analysis of depth method

An alternative way is to analyse the positioning error based on depth information from a pressure sensor (Wang *et al.*, 2018), which is often mounted on the ROV framework. Depth information is provided by converting the pressure difference between the transceiver head and the ROV's transponder:

$$h = h_{ROV} - h_H \qquad \text{2.18}$$

where h_{ROV} [m] is the depth value of the ROV and h_H [m] the depth value of the USBL transducer head. If the relative depth h [m] is known (see Figure C.1), Eq. [C.3] becomes:

$$h = r \cos \theta_z \qquad \text{C.19}$$

Substitution of Eq. [C.19] into Eq. [C.1] gives the following expression:

$$x = h \frac{\cos \theta_x}{\cos \theta_z} \qquad \text{C.20}$$

Now, finding the differential on both sides, and assuming that the errors are independent of each other, yields the positioning error in the x-axis direction (see appendix C.3):

$$\overline{\Delta x} = h \frac{\cos \theta_x}{\cos \theta_z} \sqrt{\left(\frac{\Delta h_{ROV}}{h}\right)^2 + \left(\frac{\Delta h_H}{h}\right)^2 + \left(\frac{\Delta \theta_x}{\cot \theta_x}\right)^2 + \left(\frac{\Delta \theta_z}{\cot \theta_z}\right)^2} \qquad \text{C.21}$$

where Δh is the depth measurement error and $\Delta \theta$ is the angle measurement error. Substituting Eq. [C.19] into Eq. [C.21], and assuming $\Delta h = \Delta h_{ROV} = \Delta h_H$, the positioning accuracy of relative range is [8]:

$$\frac{\overline{\Delta x}}{r} = \cos \theta_x \sqrt{2\left(\frac{\Delta h}{h}\right)^2 + \left(\frac{\Delta \theta_x}{\cot \theta_x}\right)^2 + \left(\frac{\Delta \theta_z}{\cot \theta_z}\right)^2} \qquad \text{C.22}$$

From Eq. [C.22], it can be seen that the USBL positioning accuracy based on depth information is inversely proportional to the depth estimation error Δh, and the angle measurement error $\Delta \theta$. Similar to the positioning accuracy expression of Eq. [C.17], the USBL positioning accuracy has the best performance in the range of cone angles directly below the transceiver. Contrasting Eq. [C.22] and Eq. [C.17], it can be found that the USBL positioning calculation method based on depth information eliminates the error caused by the element spacing error Δd, the wavelength error $\Delta \lambda$ ($= \Delta c_H / f$) and the ranging error Δr ($= \Delta(c_H t)$), and thus indirectly the harmonic mean sound velocity estimation error Δc_H and time delay measurement error Δt. The phase-difference error $\Delta \varphi$ is replaced by the angle measurement error $\Delta \theta$ The latter is often provided in technical specifications by the manufacturer.

Again, quantification of the relative error factors yields:

The relative depth measurement error factor $\frac{\Delta h}{h}$

The depth measurement error Δh depends on the accuracy of the pressure sensor. If the pressure sensor is from Valeport and attached to the miniSVS, the maximum error is $\Delta h = 0.05\% \, h$ (Valeport Limited, 2020):

Evaluating the relative depth measurement error factor: $\sqrt{2\left(\frac{\Delta h}{h}\right)^2} = 0.00071$

The relative angle measurement error factor $\frac{\Delta \theta}{\cot \theta}$

As the angle measurement error $\Delta \theta$ replaces the phase-difference error $\Delta \varphi$ in the expression for the positioning accuracy, it also depends on the signal's acoustic properties and background noise.

---

[8] The positioning accuracy based on depth information in terms of the phase-difference error $\Delta \varphi$, instead of the angle measurement error $\Delta \theta$, was derived by Wang *et al.* (2018): $\frac{\overline{\Delta x}}{r} = \cos \theta_x \sqrt{2\left(\frac{\Delta h}{h}\right)^2 + \left(\frac{\Delta \varphi_x}{\varphi_x}\right)^2 + \left(\frac{\Delta \varphi_z}{\varphi_z}\right)^2}$

TUDelft

Van Oord
Marine ingenuity

Fortunately, manufacturers of high-precision acoustic positioning systems provide technical details about the angular accuracy for a specific signal-to-noise ratio. If the transducer head is a HiPAP 502 from Kongsberg Maritime, for $SNR = 20$, $\Delta\theta = 0.06° = 0.001\ rad$ (Kongsberg Maritime, 2016). Considering a range of $r = 1000\ m$, and an offset from the transceiver no more than 10% of the water depth (see Figure C.5), the angles in x-and z-direction are, respectively:

$$\frac{\Delta\theta_x}{\cot\theta_x} = \tan(\theta_x)\,\Delta\theta_x = \frac{h}{0.1h}\Delta\theta_x = 0.0105$$

$$\frac{\Delta\theta_z}{\cot\theta_z} = \tan(\theta_z)\,\Delta\theta_z = \frac{0.1h}{h}\Delta\theta_z = 0.0001$$

Evaluating the relative angle measurement error factor: $\sqrt{\left(\frac{\Delta\theta_x}{\cot\theta_x}\right)^2 + \left(\frac{\Delta\theta_z}{\cot\theta_z}\right)^2} = 0.0105$

Comparing the contributions of the relative error factors, it can be concluded that the angle measurement error is by far dominant over the error induced by the pressure sensor i.e. two orders of magnitude larger influence.

The horizontal positioning error as function of the incident angle θ_z (Eq. [C.22]) is plotted in Figure C.4. for different depths h, with an error $\Delta h = 0.05\%\ h$, and $\Delta\theta = 0.06°$ (SNR = 20). From Figure C.4 we can see that the horizontal positioning error increases with increasing depth h and increasing incident angle θ_z. In particular for large incident angles, the error increases rapidly. For small incident angles, the error is rather constant and depends on depth only. It is interesting to express the relationship for the error in case of small incident angles for engineering application, because a flexible fallpipe ROV (FPROV) has a limited angular range. In practice, the maximum offset of the FPROV is 10% of the depth h, which is $\theta_z = \arctan(0.1h/h) = 5.7°$ (highlighted in blue in Figure C.4)
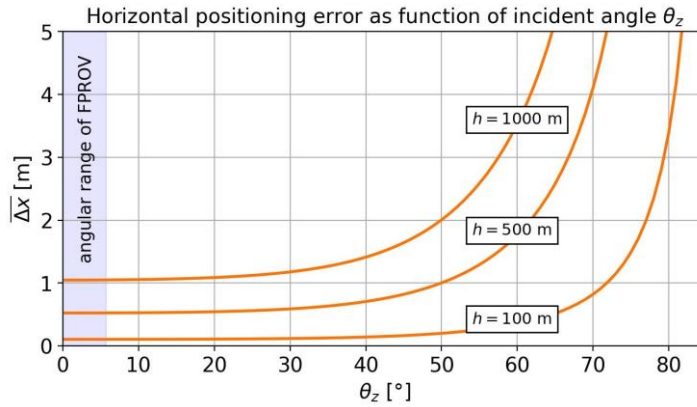

Figure C.4 Horizontal positioning error as function of incident angle θ_z for different depths h. Angular accuracy is 0.06° for SNR = 20 for the transducer head HiPAP 502 from Kongsberg Maritime. The limited angular range of a FPROV is highlighted in blue.

For the case of these small incident angles ($\theta_z \leq 5.7°$, offset $\leq 0.1h$) the horizontal positioning error remains constant. Therefore, the horizontal positioning accuracy in Eq. [C.22] can be written as:

$$\frac{\overline{\Delta x}}{r} = \cos\theta_x \sqrt{\underbrace{2\left(\frac{\Delta h}{h}\right)^2}_{\approx 0} + \left(\frac{\Delta\theta_x}{\cot\theta_x}\right)^2 + \underbrace{\left(\frac{\Delta\theta_z}{\cot\theta_z}\right)^2}_{\approx 0}}$$

$$\frac{\overline{\Delta x}}{r} = \cos\theta_x \sqrt{\left(\frac{\Delta\theta_x}{\cot\theta_x}\right)^2}$$

TUDelft

Van Oord
Marine ingenuity

$$\frac{\overline{\Delta x}}{r} = \sin(\theta_x)\Delta\theta_x \qquad \text{C.23}$$

From Figure C.3 it appears that: $\sin\theta_x = h/r$. Then, the horizontal positioning error becomes:

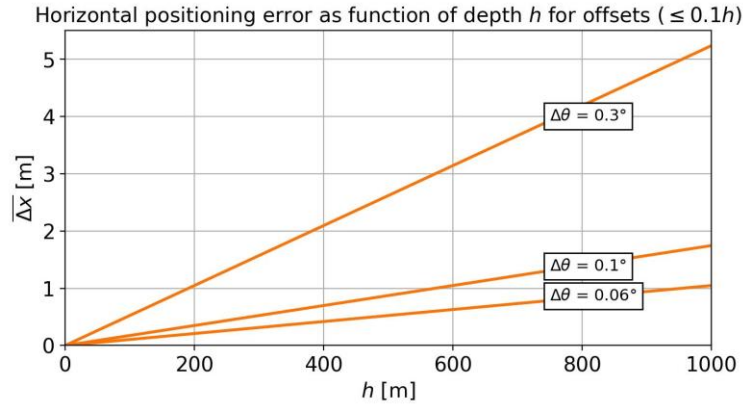$$\overline{\Delta x} = r\sin(\theta_x)\Delta\theta_x = h\Delta\theta_x \qquad \text{C.24}$$

Figure C.5 Horizontal positioning error as function of depth h for different angle measurement errors $\Delta\theta$, valid for incident angles $\theta_z \leq$ 5.7° or offsets $\leq 0.1h$. For the transducer HiPAP 502 from Kongsberg Maritime, $\Delta\theta = 0.3°$ for SNR $= 0$, $\Delta\theta = 0.1°$ for SNR $= 10$, $\Delta\theta = 0.06°$ for SNR $= 20$ (Kongsberg Maritime, 2016).

What remains is a simple linear relationship between the horizontal positioning error and the angular error scaled by the depth, valid for small incident angles (or offsets). The dependence on the angle is now kept by the depth. The relationship is plotted in Figure C.5 for different angular accuracies prescribed for a specific signal-to-noise ratio by the manufacturer.

From Eq. [C.24] and Figure C.5 we infer that the horizontal positioning error increases with decreased angular accuracy, and this positioning error increases with increasing depth h. Already for small incident angles $\theta_z \leq 5.7°$ or offsets $\leq 0.1h$, the positioning error can be of the order of meters. For the offshore contractor it means that strong background noise can negatively impact the positioning accuracy, even when the ROV is in the range of cone angles directly below the transceiver (e.g. FPROV). According to Ross and Kuperman (1989), the strongest noise is typically the propeller/bow thrusters when cavitating. Cavitation involves the formation of bubble clouds, that grow, vibrate and collapse. Consequently, an overall broadband noise spectrum is produced (few Hz to over 100 kHz). Cavitation noise increases with vessel size, load and speed (Ross and Kuperman, 1989). Also, the machinery and engine onboard of the vessel, vibrating into the water through the vessel's hull. Furthermore, turbulence-induced flow past the hull can generate additional narrow-band noise (Urick, 1983). These noise sources lead to a complicated and dynamic noise field (Erbe *et al.*, 2019), therewith decreasing the signal-to-noise ratio. It can negatively influence the angular accuracy when the transducer is determining the direction of the acoustic signal emitted by the ROV's transponder.

C.3 Derivation of Positioning Error Equations

C.3.1 Derivation of positioning error equation based on slant range and azimuth method

The positioning error equation of the USBL positioning system in the x-axis can be obtained by taking the total derivative of Eq. [C.13] (Wang *et al.*, 2018; Tong *et al.*, 2019). The total derivate is a linear approximation in quantifying the error. Using Eq. [C.13] yields:

$$\mathrm{D}x(r, \lambda, \varphi_x, d) = \frac{\partial x}{\partial r}\mathrm{d}r + \frac{\partial x}{\partial \lambda}\mathrm{d}\lambda + \frac{\partial x}{\partial \varphi_x}\mathrm{d}\varphi_x + \frac{\partial x}{\partial d}\mathrm{d}d$$

$$\Delta x = \frac{\lambda\varphi_x}{2\pi d}\Delta r + \frac{r\varphi_x}{2\pi d}\Delta\lambda + \frac{r\lambda}{2\pi d}\Delta\varphi_x - \frac{r\lambda\varphi_x}{2\pi d^2}\Delta d$$

$$\Delta x = \frac{r\lambda\varphi_x}{2\pi d}\left(\frac{\Delta r}{r} + \frac{\Delta\lambda}{\lambda} + \frac{\Delta\varphi_x}{\varphi_x} - \frac{\Delta d}{d}\right) \tag{C.25}$$

where Δr is ranging error, $\Delta\lambda$ the wavelength error, $\Delta\varphi$ the phase-difference error and Δd is the spacing error between the transducer elements.

Using Eq. [C.4] and Eq. [C.7], the positioning error can be rewritten:

$$\begin{aligned}\Delta x = \frac{r\lambda\varphi_x}{2\pi d}\left(\frac{\Delta r}{r} + \frac{\Delta\lambda}{\lambda} + \frac{\Delta\varphi_x}{\varphi_x} - \frac{\Delta d}{d}\right) &= \frac{r\lambda\varphi_x}{2\pi d}\left(\frac{\Delta(c_H t)}{c_H t} + \frac{\Delta c_s}{f\lambda} + \frac{\Delta\varphi_x}{\varphi_x} - \frac{\Delta d}{d}\right) \\ &= \frac{r\lambda\varphi_x}{2\pi d}\left(\frac{\Delta c_H}{c_H} + \frac{\Delta t}{t} + \frac{\Delta c_s}{c_s} + \frac{\Delta\varphi_x}{\varphi_x} - \frac{\Delta d}{d}\right) \\ &\approx \frac{r\lambda\varphi_x}{2\pi d}\left(2\frac{\Delta c_H}{c_H} + \frac{\Delta t}{t} + \frac{\Delta\varphi_x}{\varphi_x} - \frac{\Delta d}{d}\right)\end{aligned} \tag{C.26}$$

where Δc_H is the harmonic mean sound speed estimation error, and Δt is the time delay measurement error. Following Wang *et al.* (2018) and Tong *et al.* (2019), the errors are assumed to be independent of each other. Then the root-mean-square error in the x-axis direction is:

$$\overline{\Delta x} = \frac{r\lambda\varphi_x}{2\pi d}\sqrt{2\left(\frac{\Delta c_H}{c_H}\right)^2 + \left(\frac{\Delta t}{t}\right)^2 + \left(\frac{\Delta\varphi_x}{\varphi_x}\right)^2 + \left(\frac{\Delta d}{d}\right)^2} \tag{C.27}$$

C.3.2 Derivation of positioning error equation based on depth method

The positioning error equation of the USBL positioning system in the x-axis can be obtained by taking the total derivative of Eq. [C.20] (Wang *et al.*, 2018):

$$\mathrm{D}x(h, \theta_x, \theta_z) = \frac{\partial x}{\partial h}\mathrm{d}h + \frac{\partial x}{\partial \theta_x}\mathrm{d}\theta_x + \frac{\partial x}{\partial \theta_z}\mathrm{d}\theta_z$$

$$\Delta x = \frac{\cos\theta_x}{\cos\theta_z}\Delta h - h\frac{\sin\theta_x}{\cos\theta_z}\Delta\theta_x + h\frac{\cos\theta_x\sin\theta_z}{\cos^2\theta_z}\Delta\theta_z$$

$$\Delta x = h\frac{\cos\theta_x}{\cos\theta_z}\left(\frac{\Delta h_{ROV} - \Delta h_H}{h} - \frac{\Delta\theta_x}{\cot\theta_x} + \frac{\Delta\theta_z}{\cot\theta_z}\right) \tag{C.28}$$

where Δh is the depth measurement error and $\Delta \theta$ is the angle measurement error. Assuming that the errors are independent of each other, the mean-square error in the x-axis direction is:

$$\overline{\Delta x} = h \frac{\cos \theta_x}{\cos \theta_z} \sqrt{\left(\frac{\Delta h_{ROV}}{h}\right)^2 + \left(\frac{\Delta h_H}{h}\right)^2 + \left(\frac{\Delta \theta_x}{\cot \theta_x}\right)^2 + \left(\frac{\Delta \theta_z}{\cot \theta_z}\right)^2} \tag{C.29}$$